Cardiff Catalysis Institute

Sefydliad Catalysis Caerdydd

The Catalytic Decomposition of Ammonia

Thesis submitted in accordance with the requirement of Cardiff University for the degree of Doctor of Philosophy

Luke A. Parker

School of Chemistry

Cardiff University

2015-2019

DECLARATION

This work has not been submitted in substance for any other degree or award at this or any other university or place of learning, nor is being submitted concurrently in candidature for any degree or other award.

Signed ……………………… (candidate)   Date …………………..

STATEMENT 1

This thesis is being submitted in partial fulfilment of the requirements for the degree of PhD

Signed ……………………… (candidate)   Date …………………..

STATEMENT 2

This thesis is the result of my own independent work/investigation, except where otherwise stated, and the thesis has not been edited by a third party beyond what is permitted by Cardiff University's Policy on the Use of Third Party Editors by Research Degree Students. Other sources are acknowledged by explicit references. The views expressed are my own.

Signed ……………………… (candidate)   Date …………………..

STATEMENT 3

I hereby give consent for my thesis, if accepted, to be available online in the University's Open Access repository and for inter-library loan, and for the title and summary to be made available to outside organisations.

Signed ……………………… (candidate)   Date …………………..

Abbreviations and Units

%	Percent
°C	Degrees Celsius
Å	Angstrom (10^{-10} meters)
ΔH	Enthalpy change
a.u.	Arbitrary units
ADF	Annular dark field
BET	Brunauer, Emmet and Teller
BF	Bright field
BSD	Back Scattered Detector
cm	Centimetre (10^{-2} m)
CO_x	Carbon oxides (CO/CO_2)
CNTs	Carbon nanotubes
CVI	Catalysts prepared by Chemical Vapour Impregnation
DFT	Density functional theory
DRIFTS	Diffuse reflectance infrared fourier transform spectroscopy
EDX/EDS	Energy-dispersive X-ray spectroscopy
EELS	Electron energy loss spectroscopy
eV	Electron Volts
FT-IR	Fourier transform infrared spectroscopy
FWHM	Full-width half-maximum
g	Gram
h	Hours
HAADF	High Angle Annular Dark-Field
IR	Infrared Spectroscopy
M	Molar (mol dm^{-3})
MFC	Mass Flow Controllers
mg	Milligram (10^{-3} g)
min	Minutes
mL	Millilitre (10^{-3} L)
mm	Millimetre (10^{-3} m)
μm	Micrometre (10^{-6} m)
mol	Moles

MWCNTs	Multi-walled carbon nanotubes
nm	Nanometre (10^{-9} m)
RDS	Rate determining step
SEM	Scanning electron microscopy
STEM	Scanning transmission electron microscopy
SS	Stainless Steel
TCD	Thermal conductivity detector
TEM	Transmission electron microscopy
TOF	Turnover frequency
TPD	Temperature programmed desorption
TPR	Temperature programmed reduction
wt. %	Weight percent
XPS	X-ray photoelectron spectroscopy
XRD	X-ray diffraction

Abstract

Chemical vapour impregnation was investigated as a novel preparation method for Ru/Al_2O_3 catalysts for the production of hydrogen through ammonia decomposition. These catalysts were shown to be more active than those produced by impregnation. TEM imaging showed that this is because more particles were within the optimal 3-5 nm range. Investigation by XPS also revealed that less Cl^-, a known inhibitor, is present in the CVI prepared catalyst.

CoMoN catalysts have previously been shown to exhibit a synergistic effect with activity higher than that of Ru. The effect of pH on the preparation of these catalysts was investigated. Catalytic testing did not present this synergy and further investigation by XRD revealed this to be due to incomplete nitridation of the $CoMoO_4$ precursors.

Fe-Pt, Fe-Pd and Fe-Ni/Al_2O_3 catalysts were prepared by CVI to investigate the robustness of periodic table interpolation as a catalyst design method. Although all catalysts were predicted to show enhanced activity only Fe-Pt demonstrated a large enhancement, with Fe-Pd showing limited synergy and Fe-Ni showing none. STEM investigation showed that small, alloyed Fe-Pt particles were prepared by CVI that rearranged under reaction conditions but were catalytically stable. XRD suggested that the enhancement observed in Fe-Pd catalysts was due to particle size effects and the same was demonstrated for Fe-Ni using N_2O titration.

The activity of Fe catalysts was shown to be enhanced significantly upon the addition of a Cs promotor. The optimal Cs loading was shown to be between 0.5 and 1 mol eq. with further increase in Cs leading to a decrease in activity. XPS and TPR studies suggest that the enhancement is due to an electronic interaction between the two metals. XRD and BET surface area investigations show the decrease in promotion at higher Cs loadings is due to an amorphous layer of CsOH forming over the support; blocking active sites and causing a decrease in catalyst surface area.

Table of Contents

1 Introduction

1.1 Catalysis in Society

1.1.1 What is a Catalyst?

It is safe to say that without catalysis, life as we know it would cease to exist. All the plastic products in use need numerous catalytic steps such as cracking (the process by which the large molecules in crude oil are broken down into smaller, more useable molecules) and polymerisation (where these smaller molecules are built up into long, repeating chains to form materials such as polyethylene terephthalate, PET) to prepare from raw materials[1–3] and then more to assist in their recycling.[4] Many of our favourite drinks are brewed using one of nature's finest catalysts.[5] In fact, 50% of the population is only alive thanks to advances in catalysis[6] and the majority of industrial processes use catalysis. But what is catalysis? And what is a catalyst?

The IUPAC definition of a catalyst is given as follows and answers both questions:

> "*A substance that increases the rate of a reaction without modifying the overall standard Gibbs energy change in the reaction; the process is called catalysis*"[7]

The first key point in this definition is the use of the word "substance". A catalyst can be almost anything; solid, liquid or gas and depending on its form (and the nature of the reaction) we can divide catalysts into two groups, homogeneous and heterogeneous catalysts. Homogeneous catalysts are those in the same phase as the reactants (e.g. liquid catalysts in a liquid reaction) and heterogeneous catalysts are those in a different phase to the reactants (e.g. solid catalyst in a gas phase reaction). The second key point is that the Gibbs energy change is not modified. In other words, the outcome itself stays the same with the catalyst increasing the rate of reaction by offering an alternative reaction pathway with lower activation energies. One final point

to be made is noted at the end of the IUPAC definition: "*The term catalysis is also often used when the substance is consumed in the reaction… Strictly, such a substance should be called an activator.*"[7]

1.1.2 Why are Catalysts Needed?

Catalysts are used for a number of reasons, namely: necessity, legislative pressure and profit. For some processes, especially bulk chemical production, the reaction would not be feasible without a catalyst present. This is evidenced in the case of ammonia synthesis, where although alternative production methods exist they would not be able to keep up with global demand. In other cases, such as automotive emission catalysts, it is legislative pressure that caused catalytic converters to be introduced and the continuing tightening of regulations pushes the continued research into the improvement of these catalysts. Unlike those processes where catalysts are necessary for their implementation, cars can (and indeed did, until legislation came into effect) run without catalytic converters and it wasn't until the environmental impact of automotive emissions was realised and legislated against in the 1970s that catalytic abatement was added to cars.[8] Since then, legislation targets have been lowered and this has encouraged continued development of catalysts.[9]

The final reason is money. Companies can save money in the manufacturing process by introducing or modifying a catalyst and this drives implementation and innovation. There are numerous ways in which money can be saved through the addition of a catalyst. The first is lowering the energy requirements of the reaction as this can be a large expense, especially for reactions that run at high temperatures. This can be achieved by developing catalysts that allow reactions to run at lower temperatures. Money can also be saved by developing more selective catalysts. Some processes produce numerous by-products that require expensive clean-up stages after the reaction (such as distillation) and lower the overall yield of desired product. More selective catalysts can remove the expense of additional purification steps as well as increase the amount of sellable commodity produced.

1.2 Ammonia Synthesis

This all-too-brief review of ammonia synthesis serves two purposes: firstly, it is one of the most well-known examples of a heterogeneously catalysed reaction and demonstrates practically the points made in the previous section. Secondly, it is intrinsically linked with its reverse reaction (and the focus of this work), ammonia decomposition. In order to understand many of the catalyst design considerations mentioned later about decomposition there must be a basic understanding of the synthesis reaction.

1.2.1 The Haber - Bosch process

The Haber-Bosch process is the main process used for the production of ammonia worldwide. Named after its developers Fritz Haber and Carl Bosch, who won the Nobel Prize for their contributions to its development in 1918[10] and 1931[11] respectively, it was first used industrially in Germany during World War I in order to produce ammonia for explosives. Nowadays NH_3 is used mainly as a fertiliser in crop production and without it food production on a scale that can support world population would not be possible.[6] Figure 1 shows the dependence of the world population on the Haber-Bosch process.

Before the Haber-Bosch process, ammonia production on an industrial scale was challenging and nitrogen-based fertilizers were usually prepared through either the Birkeland-Eyde or Frank-Caro processes. Although air was well-known to be the most abundant source of N_2, the inertness of the N_2 molecule made ammonia production from air a challenge. In 1909, Fritz Haber and his assistant Robert de Rossingnol provided the first example of ammonia formation from air by using a high pressure reactor with a solid catalyst. The technology was purchased by BASF, for whom Carl Bosch was working at the time, and who scaled up the reaction from Haber's lab scale reactor to an industrial production scale.
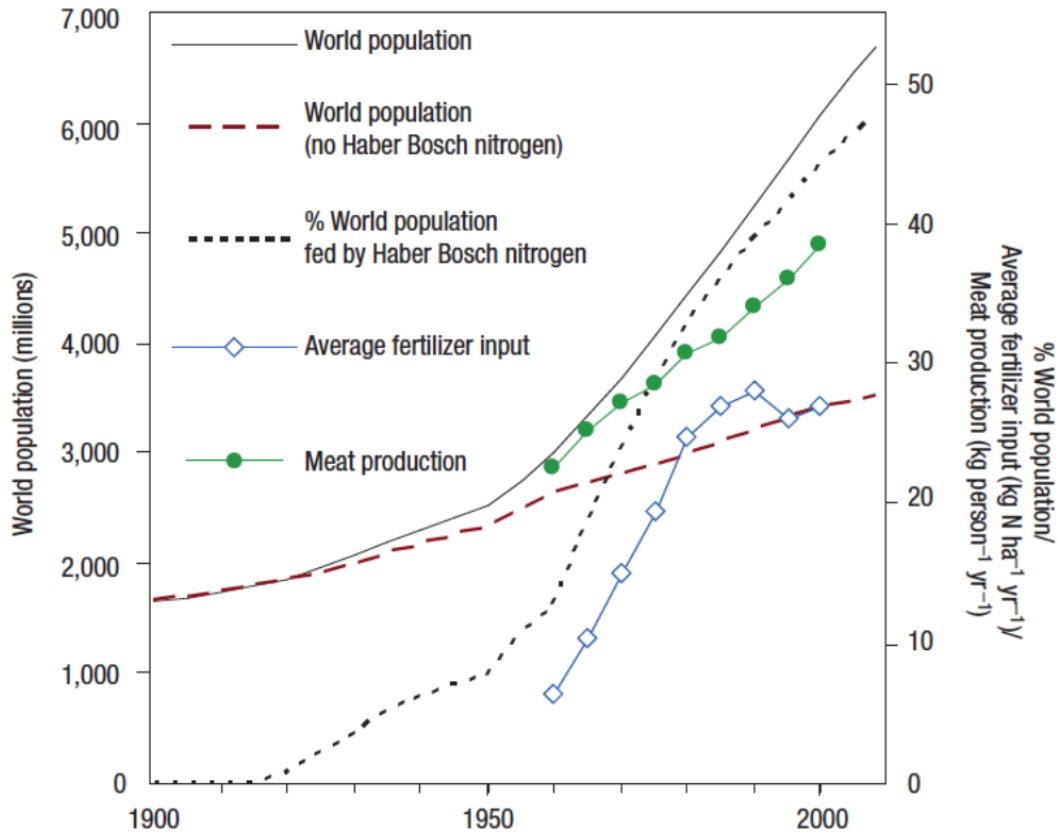
Figure 1: Dependence of world population on Haber-Bosch ammonia. Reproduced from ref. 6.

1.2.2 Thermodynamics, Kinetics and Mechanism

The reaction conditions for the Haber-Bosch process remain energy intensive, with pressures between 200-300 bar and temperatures between 400-500 °C. These conditions illustrate the complexities of balancing thermodynamics and kinetics in a catalytic reaction. Le Châtelier's principle states:

"If a system is in equilibrium, any change imposed on the system tends to shift the equilibrium to nullify the effect of the applied change."[12]

Ammonia synthesis is shown in Equation 1, along with the enthalpy of the reaction. It is shown that the pressure of the reaction decreases for the forward reaction and, because of this, it is thermodynamically favourable for the reaction to be performed at high pressure. However, as the forward reaction is exothermic it is surprising that the reaction is operated at such high temperatures. This is due to the unfeasibly low rate of reaction at lower

temperatures. This is a textbook example of balancing thermodynamics and kinetics in a complex catalytic reaction.

Equation 1: Ammonia synthesis reaction

$$N_2 + 3H_2 \rightleftharpoons 2NH_3 \qquad \Delta H = -92 \text{ kJ/mol}$$
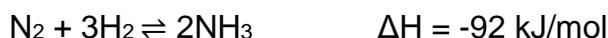
The mechanism of ammonia synthesis has been reported by Ertl in 1980 as shown in Equation 2.[13]

Equation 2: Ammonia synthesis mechanism

$$H_2 \rightleftharpoons 2H_{ads}$$

$$N_2 \rightleftharpoons N_{2,ads} \rightleftharpoons 2N_{ads}$$

$$N_{ads} + H_{ads} \rightleftharpoons NH_{ads}$$

$$NH_{ads} + H_{ads} \rightleftharpoons NH_{2,ads}$$

$$NH_{2,ads} + H_{ads} \rightleftharpoons NH_{3,ads} \rightleftharpoons NH_3$$
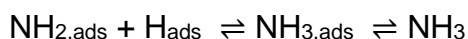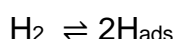
It was demonstrated that the rate limiting step of the reaction is the dissociative chemisorption of N_2. This is consistent with previous literature.[14–16] It is also noted that for the decomposition reaction the reverse of this step, associative desorption of N_2, is rate-limiting.

1.2.3 Fe Catalysts and Their Promotors

Since its inception, Fe-based catalysts have been the choice for ammonia synthesis. Initially, Fe_3O_4 reduced in *in-situ* to metallic Fe was used as a fine powder with the addition of Al_2O_3 as a structural promoter[17] but later studies focussed on supported Fe nanoparticles. The reaction over Fe/MgO has been shown to be structure sensitive, with large particles being an order of magnitude more active than small particles.[18] Further investigations of the catalyst surface have shown that the active site of the catalyst is a C_7 site – an Fe atom with seven nearest neighbours.[19,20]

Promotors have been used in Fe-based catalysts since their inception. These promoters fall broadly into two categories: structural promoters and electronic promoters. Structural promoters have included Al, which has been shown to

enhance activity by stabilising the α-Fe phase formed after reduction of the Fe_2O_3 precursor and prevent sintering. Alkali promoters such as K are known as electronic promoters and enhance activity by facilitating the rate determining step, N_2 dissociative adsorption.[21] Ertl et al. investigated the promotional mechanism of K on Fe(100) and Fe(111) surfaces and reported that the N_2 heat of adsorption increased in the presence of an adsorbed K atom.[22] This lowers the activation energy of N_2 dissociative desorption. This occurs due to charge transfer from K enhancing back-bonding in the metal-N bond.

1.2.4 Ru Catalysts and Their Promotors

Late in the 20th century, Ru emerged as a more active catalyst than Fe and has since been commercialised,[23,24] however, despite its higher activity the catalyst suffers from higher cost and lower stability.[25] The reaction over Ru was also shown to be surface sensitive and the active site in this case is a B_5 site (an Ru atoms with 5 neighbouring Ru atoms) as opposed to the C_7 active site of Fe-based catalysts. Jacobsen *et al.* investigated the nature of the reaction over Ru supported on $MgAl_2O_4$, two forms of C and Si_3N_4. They found that the $Ru/MgAl_2O_4$ was more active than the two Ru/C catalysts and Ru/Si_3N_4 was the least active catalyst.[26] It was noted that the activity trend is not adequately explained by the difference in metal dispersion and demonstrated that there is an optimal particle size where B_5 sites are maximised. The support also plays an important role in particle morphology, further maximising the number of B_5 sites.
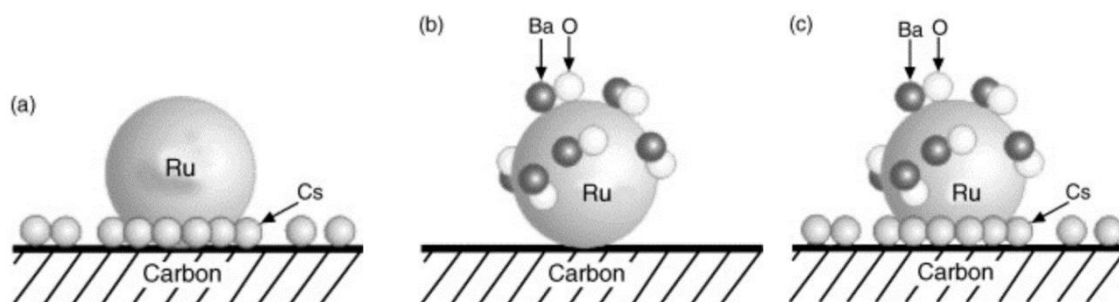
Figure 2: Interaction of different promotors with the active site on Ru/C ammonia synthesis catalysts. Reproduced from ref. 27.

Three promoters, Ba, Cs and K were investigated for Ru catalysts by Kowalczyk *et al.* and suggested that although all three metals promote the reaction over Ru, the mechanism of promotion is different over the alkali metals (K and Cs) and Ba.[27] It has been shown that Ba is distributed on top of the Ru nanoparticles, whereas Cs is present at the Ru/C interface as shown in Figure 2. The mechanism of Ba promotion is debated, with some researchers suggesting it is a structural promoter, enhancing activity by modifying the surface to create more B_5 sites and others suggesting an electronic effect. It is believed that Cs acts as an electronic promoter in this catalyst whereby the electropositivity of the Cs causes and electrostatic change in the Ru active site.

1.3 Catalysis for Renewable Energy

1.3.1 Global Warming

Global warming is seen as one of the greatest challenges facing mankind in the 21st century and is defined by NASA as "the increase in Earth's average surface temperature due to rising levels of greenhouse gases".[28] Although the global average temperature has been shown to rise and fall naturally throughout the history of the Earth, it is the rapid rise in temperature that has been attributed to the growing number of greenhouse gases that sets this instance apart from the rest. Whereas climate changes usually occurs over thousands of years, a marked increase in the Earth's surface temperature has been noted since the mid-20th century and this is shown in Figure 3.[29]
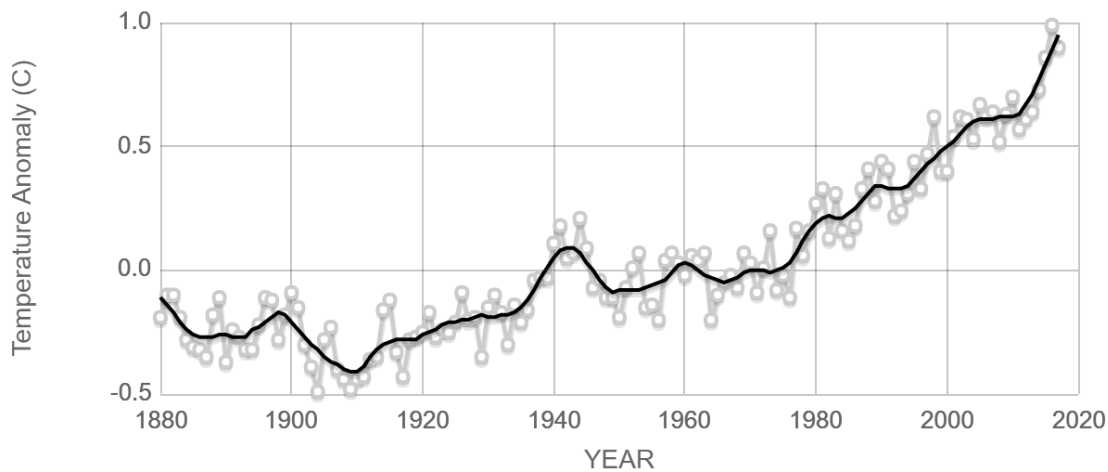
Source: climate.nasa.gov

Figure 3: Global temperature change 1880-2018. Reproduced from ref. 29.

During the industrial revolution of the mid-18th to 19th century, many processes became automated and locomotive transportation increased dramatically. Since then, industrial manufacturing and processes (such as the aforementioned Haber-Bosch process) as well as a rise in automobile ownership have all contributed further to the release of harmful greenhouse gases into the atmosphere and these are referred to as anthropogenic, or man-made, sources.

Greenhouse gases are gases which persist in the atmosphere and absorb energy in the thermal-infrared region. They contribute to what is known as the greenhouse effect, the major contributor to global warming. Global temperature should remain stable due to equilibrium between the thermal energy from the sun being absorbed by the earth and also emitted through the atmosphere. However, as the concentration of greenhouse gases in the atmosphere increase, less energy is emitted and more is trapped in the atmosphere, leading to a rise in global temperature. Some common examples of greenhouse gases include methane, nitrous oxide and H_2O, however, the greenhouse gas most emitted in the largest quantities is CO_2 and it is these emissions that are the focus of most efforts to curtail climate change. The majority of CO_2 is released through power generation processes which largely rely on the combustion of fossil fuels. Therefore, one approach to vastly reduce carbon emissions is to utilise alternative, non-carbon based fuels.

1.3.2 Alternative Fuels

In Jules Verne's "The Mysterious Island", the character Cyrus Harding claims;

> *"Yes, my friends, I believe that water will one day be employed as fuel, that hydrogen and oxygen which constitute it, used singly or together, will furnish an inexhaustible source of heat and light, of an intensity of which coal is not capable."*[30]

In 1874 this was merely science fiction, however, within 100 years it is startling how much of this quote was realised. Hydrogen had already been investigated as a fuel, with William Grove demonstrating its use in the first example of what is now known as the fuel cell,[31] and production of hydrogen through electrolysis of water has drawn a lot of research interest as the 'holy grail' of clean energy.[32–35] The proton-exchange membrane fuel cell (PEMFC) works by the electrochemical reaction of hydrogen and oxygen to form water. Hydrogen enters the fuel cell at one electrode (the anode) and is turned into protons and electrons. The protons move through an electrolyte to a second electrode (the cathode) where oxygen enters. The electrons then flow through a circuit to the cathode where they are combined with the protons and oxygen to form water. It is this flow of electrons from anode to cathode that causes a current and can be used for electrical power. Development of the fuel cell in the 150 years since has seen it emerge as an ideal mobile generation method. There have been a number of vehicles released commercially utilising PEMFC power such as the Honda Clarity[36] and Aston Martin Rapide S, which completed the Nürburgring 24-hour race.[37] Another form of fuel cell, the solid oxide fuel cell (SOFC), contains a solid oxide as the electrolyte through which oxygen ions travel and react with hydrogen at the anode. These typically operate at much higher temperatures than PEMFCs.

However, the main challenge limiting the potential of hydrogen being used as a fuel is its storage. In order for a useable amount of hydrogen to be stored it must be compressed to pressures ~200 bar. This is not a problem for stationary power generation, however, for mobile applications this presents a significant safety risk and leads to refuelling issues. Two main schools of

thought have developed in the research into H_2 storage materials: adsorptive storage and chemical storage.

Adsorptive storage materials are a group of materials which store hydrogen molecularly through physisorption by van der Waals interactions. Materials in this category typically possess high surface areas and are highly porous and include materials such as MOFs[38–43] and porous carbon structures.[44–46] In chemical storage media, hydrogen is chemically bonded with covalent or ionic bonds as opposed to weak interactions. Hydrogen is present as H in these materials, forming H_2 as it is released. Materials in this category include metal hydrides[47–49], liquid hydrocarbons,[50–52] and ammonia which is the focus of this work.

1.4   Ammonia Decomposition

Ammonia is a promising hydrogen storage material for the fuel industry. It is the second most produced chemical worldwide and is easily liquefied at moderate pressures and temperatures. Due to its liquid form and its abundance as a commodity chemical, transport infrastructure is already in place and modification of fuelling stations would take little effort. Another benefit of ammonia is its hydrogen content; at 17.6% it is one of the most hydrogen dense storage materials. This addresses the storage issues presented by gaseous hydrogen.

Ammonia is not without its disadvantages. Economically, it is already produced on a large scale for use as a fertilizer and wide-scale use as a fuel would lead to competition and increase its price. It is also toxic and causes environmental problems if leaked into bodies of water. Chemically, it is a potent fuel cell poison with a threshold of <1 ppm, therefore, further clean-up would be necessary. As the Nafion® membrane of a fuel cell is acidic, NH_3 titrates it and the poisoning effect is therefore irreversible degradation of the fuel cell.[53] However, suitable absorbers and membrane systems have been demonstrated that would deliver a pure H_2 feed to the fuel cell.[54] Objections have also been raised due to the toxicity of ammonia as a fuel. Ammonia

readily forms less toxic salts with many cheap and abundant metals and these have been shown to be useful as ammonia storage materials.

1.4.1 Thermodynamics and Kinetics

Ammonia decomposition is the reverse reaction of ammonia synthesis as employed in the Haber-Bosch process and is shown in Equation 3. It is an endothermic reaction and produces an increased number of molecules, therefore, high temperatures and low pressures are required for the reaction to proceed, as governed by Le Châtelier's principle.

Equation 3: Ammonia decomposition reaction

$$2NH_3 \rightleftharpoons N_2 + 3H_2 \qquad \Delta H = 92 \text{ kJ mol}^{-1}$$

As this reaction is in equilibrium with the synthesis reaction, the maximum conversion at a given temperature is governed by thermodynamics. Yin *et al.* describe these calculations from 2012 and the equilibrium conversion as a function of temperature is shown in Table 1.[55] This equilibrium conversion limit is the reason that further clean-up of H_2 produced through NH_3 decomposition is necessary, as mentioned previously, because conversion of NH_3 below 1 ppm cannot occur under feasible operating conditions.

Table 1: Equilibrium conversion of ammonia from 250-500 °C at atmospheric pressure

Temp. (°C)	250	300	350	370	400	420	450	470	500
Conv. (%)	89.2	95.7	98.1	98.6	99.1	99.3	99.5	99.6	99.7

Initially, ammonia decomposition was used to investigate the kinetics and mechanism of the forward reaction as understanding the Haber-Bosch process was the focus of the era, however, in 1980 Ertl *et al.* investigated the decomposition of ammonia on single crystal Fe surfaces with the aim of investigating the decomposition reaction itself.[56] They proposed the following mechanism:

$$NH_3 \rightleftharpoons NH_{3,ads}$$

$$NH_{3,ads} \rightarrow NH_{2,ads} + H_{ads}$$

$$NH_{2,ads} \rightarrow NH_{ads} + H_{ads}$$

$$NH_{ads} \rightarrow N_{ads} + H_{ads}$$

$$2H_{ads} \rightarrow H_2$$

$$2N_{ads} \rightarrow N_2$$
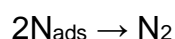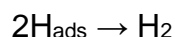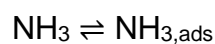
An NH_3 molecule adsorbs on the surface (1) and H is sequentially cleaved and forms surface H species (2-4), before combining on the surface to form H_2 and desorbing (5). Finally, two adsorbed N atoms recombine and desorb as N_2 (6). This final step was shown to be rate-determining and follow first order kinetics.

Tsai and co-workers investigated the kinetics of the reaction over a Ru(001) surface at low pressure (1 x 10^{-6} and 2 x 10^{-6} Torr) and observed that the rate determining step depended on reaction conditions.[57] At high temperatures (>750 K) the reaction was limiting by the N-H bond cleavage of adsorbed NH_3 molecules, whereas at lower temperatures the rate-determining step was recombinative desorption of N_2.

Shustorovich and Bell used BOC-MP (bond-order-conservation-Morse-potential) calculations to investigate the kinetics of both ammonia synthesis and decomposition over Pt(111), Ru(001), Fe(110), and Re(001) surfaces. They found that, in all cases, the activation barrier is largest for the recombinative desorption of nitrogen and predict this to be rate determining for all surfaces.[58] This is in agreement with the previous work of Tsai and co-workers.[57] For the reverse of this, $N_2 \rightarrow 2N_{ads}$, the activation barrier increased sharply with the trend Re < Fe < Pt, thereby demonstrating why Pt cannot catalyse ammonia synthesis.

These trends in activation barriers for various steps of the reaction have been shown by a number of other groups both theoretically and experimentally and are being used as descriptors for predicting novel active catalysts for both the synthesis and decomposition reaction. They play a profound role in explaining

the activity of various supported metal catalysts and will be used in the context of different classes of catalysts in the next sections.

1.4.2 Ru-based Catalysts

In 2004, Yin *et al.* investigated six transition metals (Ru, Rh, Pt, Pd, Ni and Fe) supported on CNTs for ammonia decomposition.[55] When tested for over 10 hours, all catalysts were found to be stable and Ru was found to be between 8-40 times more active than the other metals. This work also shows that larger Ru particles are more active with respect to the number of moles of NH_3 decomposed per mole of Ru in the catalyst. This is consistent with the results discussed in the previous section for the ammonia synthesis reaction.

In the same year, Ganley *et al.* investigated 13 metals from across the periodic table and also found Ru to be the most active, with the order of activity of the metals being Ru > Ni > Rh > Co > Ir > Fe >> Pt > Cr > Pd > Cu >> Te, Se, Pb.[59] With this experimental information on the activity of a large number of metals they investigated a number of properties in search of a correlation with activity. Their results suggest that nitrogen recombinative desorption is rate-limiting for Fe, Co and Ni and N-H bond scission is rate limiting for Rh, Ir, Pd, Pt and Cu. This is shown in Figure 4. They observe Ru occupying a 'goldilocks' region making it is hard to determine which step is rate-limiting, however, they noted that no property of the metal significantly slows the rate determining step.
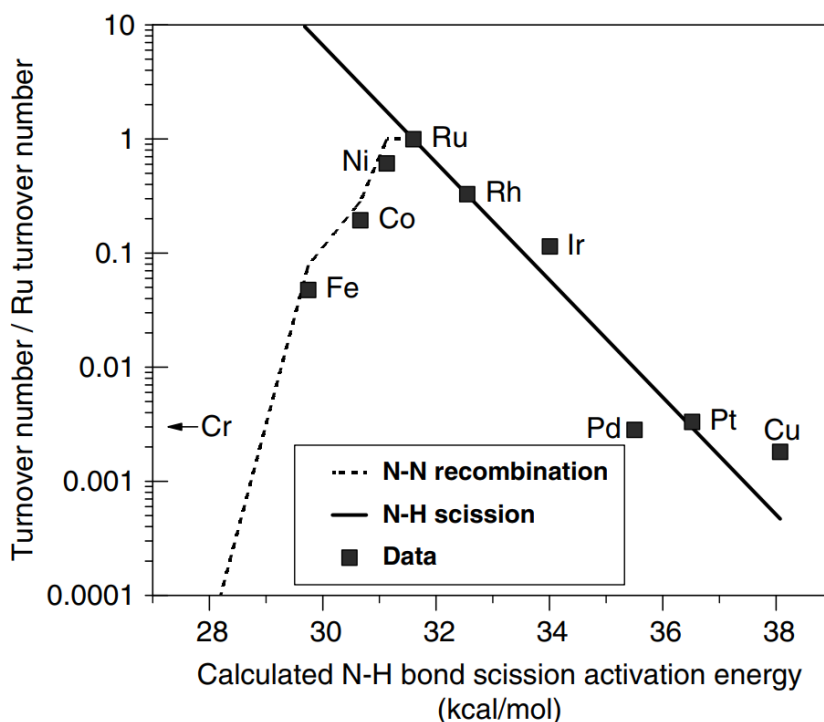
Figure 4: Dependence of ammonia decomposition activity on N-H bond scission activity for common transition metal active phases. The dotted line represents when the reaction is N-N recombination limited and the solid line represents N-H scission limitation. Reproduced from ref. 59

The work of Yin *et al.* also investigated the role of the support by impregnating a number of metal oxides, activated carbon (AC) and CNTs with Ru.[55] When comparing ammonia conversion, they found CNTs to be the most active support followed by MgO and TiO_2 (which exhibited similar activity to both Al_2O_3 and ZrO_2). However, when comparing activity with respect to the TOF, Ru supported on MgO was found to be more active than the Ru/CNT catalyst. When comparing TOF and the activation energy (E_a) data it was observed that catalyst activity increased with increasing support basicity. It was also shown that increasing the basicity of a neutral support (CNTs) or acidic support (ZrO_2-BD) by the addition of KOH also increased the activity. The authors also note that N_2 desorption appears to be the rate-determining step.

As support basicity was shown to be an important property, Ru supported on a number of modified ZrO_2 super-basic supports was investigated by Yin *et al.* in 2006.[60] These were prepared from two Ru precursors, Ru(acac)$_3$ and RuCl$_3$. It was observed that the catalyst prepared from Ru(acac)$_3$ was more active

and this is attributed to the electron-withdrawal from Ru by Cl. It was also observed that the dispersion was *ca.* 20% lower when prepared from the Cl precursor. One explanation for this could be the reaction of Cl^- and K^+ to form KCl on the surface which could block Ru sites. Comparison of the TOF of the catalysts again showed that activity increased as Ru was supported on more basic materials. Characterisation by N_2-TPD showed that the super-basicity facilitated the N_2 recombinative desorption, the RDS, and it is proposed that this is due to modification of the electronic state of the supported Ru.

Alkali and alkaline earth metals are well-known promoters for the ammonia synthesis reaction and have also been shown to be active for the decomposition reaction. It is widely believed that Ba and Cs promote the synthesis reaction by preventing sintering of Fe or Ru, therefore being termed structural promoters. Rarog-Pilecka *et al.* investigated the promotion of Ru/C catalysts with Ba and Cs for the decomposition and found that while the addition of either promoter greatly enhances the catalyst activity, Cs is a more effective promoter than Ba.[61] The same group in 2004 showed similar results for Ba- and Cs-promoted Ru supported on Mg-Al spinels, with the promoted catalyst being a factor of ten more active than the un-promoted catalyst, however, the spinel supported catalysts were less active than the previously investigated promoted Ru/C catalysts.[62]

More recently, Hill *et al.* have investigated the ideal ratio of Ru:Cs and also the effect of the support material on promoter activity.[63] They demonstrate that Cs acts only as a promoter as Cs/CNT shows no activity and that the presence of Cs dramatically enhances the activity of Ru/CNT at all tested concentrations. A volcano-type plot is observed for the effect of Cs/Ru on reaction rate and shown in Figure 5. The optimum Cs loading occurs at *ca.* 3 (Cs:Ru molar ratio), and is considered to be due to the blocking of active sites above this loading. The effect of support conductivity on promotion was also investigated by supporting Cs-promoted Ru on AC, graphitised carbon and CNTs.[64] It was observed that as the support conductivity increased the catalyst activity also increased. This was said to allow greater electronic modification of Ru by Cs that was not in direct contact with the Ru nanoparticle, thereby avoiding blocking the active site.

The development of a Cs-promoted Ru/MWCNT catalyst, which is widely regarded as the state-of-the-art, has been demonstrated by a number of groups.
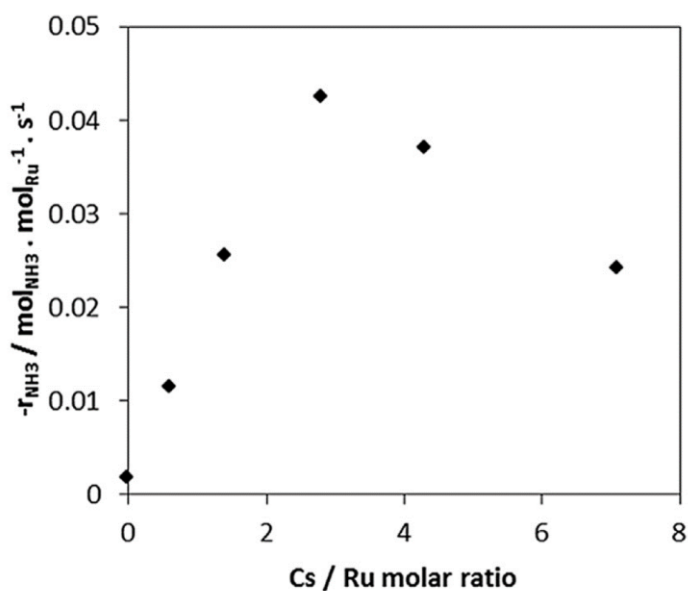
Figure 5: Effect of Cs/Ru ratio on catalyst activity. Reproduced from ref. 63.

1.4.3 Non-Ru Catalysts

While it has exceptional activity, Ru has a number of drawbacks that mean that current research is focussed on alternative active sites. The primary drawback is the scarcity of Ru. With recent technological advancements Ru, a key component in computer hard-drives, is being used in ever greater volumes. Although much is made of the price of Ru, it is a lot cheaper than other common catalytic materials such as Pt and Pd ($260 per troy ounce vs $809 and $1365, respectively as of June 2019) and as it is very stable for this reaction, the costs diminish over time.

An alternative metal of interest is Ni, due to its low cost, abundance, and high activity. Figure 4, shown previously highlighting the "goldilocks" region of high activity between the two rate determining steps, shows Ni to also be in this region with activity within an order of magnitude of Ru. Another metal that fits these criteria is Co and the research into these possible Ru replacements will be presented in this section. Several groups have shown both Ni and Co to be

active for ammonia decomposition and a number of them are presently discussed.

In 2006, Li *et al.* investigated Ru and Ni on three different SiO_2 supports: fumed SiO_2, MCM-41 and SBA-15. Although Ru was the more active metal, Ni was shown to be active at temperatures as low as 400 °C.[65] Of the three silica-supported Ni catalysts tested, Ni/MCM-41 was the most active. The addition of KOH does not increase the catalyst activity of this Ni catalyst. It was also shown that the reaction over Ni catalysts are structure-sensitive, with B5-like sites proposed as the active sites. This is consistent with the suggested active site for Ru catalysts[66] and has also been suggested by Zhang *et al.*[67]

In 2008, two groups investigated the use of lanthanide metals as promoters for metal oxide supported Ni catalysts. Liu *et al.* tested Ni/SBA-15 and found it to be active at 450 °C,[68] whilst Zheng *et al.* tested Ni/Al_2O_3, which was also active at 450 °C.[69] In both investigations, Ce was found to promote the decomposition of ammonia. Liu *et al.* also investigated La as a promoter and saw a weak promotional effect that was not as significant when compared to Ce. In both cases the optimum Ce:Ni ratio was 0.3 mol eq. and evidence was presented that inferred Ce is a structural promoter, increasing activity by increasing dispersion, facilitating the preparation of smaller nanoparticles and hindering particle agglomeration. Zheng *et al.* also demonstrated that Ni/Al_2O_3 is unstable, although, the Ce promoted catalyst was reported to be stable for 80 hours.

Co is another cheap, first-row transition metal that has garnered much attention as a potentially active NH_3 decomposition catalyst. Lendzion-Bieluń *et al.* demonstrated that although Co is not as active as Fe for the ammonia synthesis reaction, Co is a more active metal for the decomposition reaction.[70] This was also demonstrated by Zhang *et al.* who used commercial CNTs with residual Co or Fe as decomposition catalysts, although the metal loadings vary between Co and Fe (4.1 wt% vs. 2.8 wt%) due to the nature of the materials tested.[71] When comparing the Co/CNTs to other commercial decomposition catalysts they show that it is more active than the chosen catalysts (including

an Ru catalyst) even at much higher space velocities, however, other variables such as metal loading vary greatly.

The difference in suitability for the synthesis and decomposition reaction between Co and Fe can be explained by the effect of the reaction conditions on the metal binding energy. Figure 6 shows the difference in reaction rate for the synthesis and decomposition reaction (dashed lines) as a function of metal binding energy.[72] Below this are the experimental decomposition activities of a number of metals and their dissociative adsorsorption energies. It can be seen that the optimum of the synthesis curve is shifted more towards Fe whereas Co is much closer to the optimum of the decomposition curve.
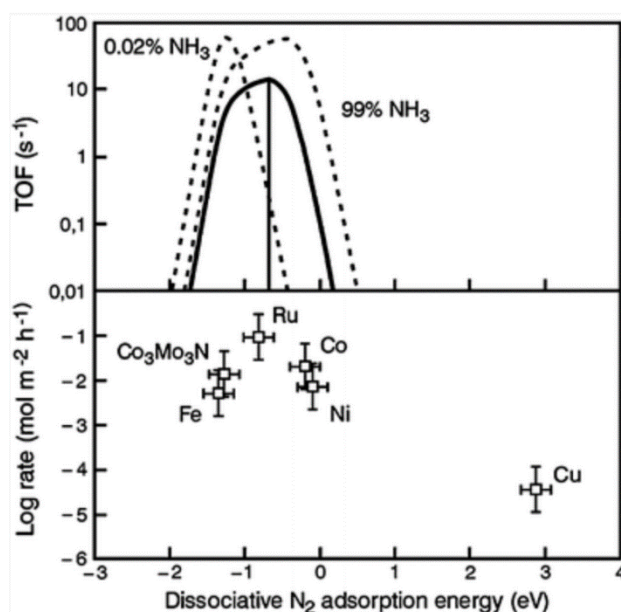
Figure 6: How the optimum N-binding energy changes between synthesis (0.02% NH₃) and decomposition (99%) gas compositions. Reproduced from ref. 72.

Torrente-Murciano *et al.* performed a systematic investigation of the effect of Co particle size, graphitisation of carbon support and the use of Cs as a promoter on decomposition activity, analogous to that of the group's investigations into Ru.[73] They found that Co responds to changes in these properties very differently to Ru. Whereas Ru has an optimal particle size of ~3-5 nm (highest density of active B5-sites), the optimum particle size of supported Co catalysts is shown to be ~2 nm. The degree of graphitisation of the carbon support also has an inverse effect on Co. Activity of Ru is seen to

increase with an increase in support graphitisation whereas Co catalysts become less active and are more active on supports with a low degree of graphitisation. This is due to the effect of conductive supports on the electronic structure of the metal atoms in the nanoparticle. These relationships are shown in Figure 7. Finally, unlike Ru catalysts, which are greatly enhanced by Cs promoters, Co catalysts are either unaffected or become less active upon addition of Cs depending on the support used.
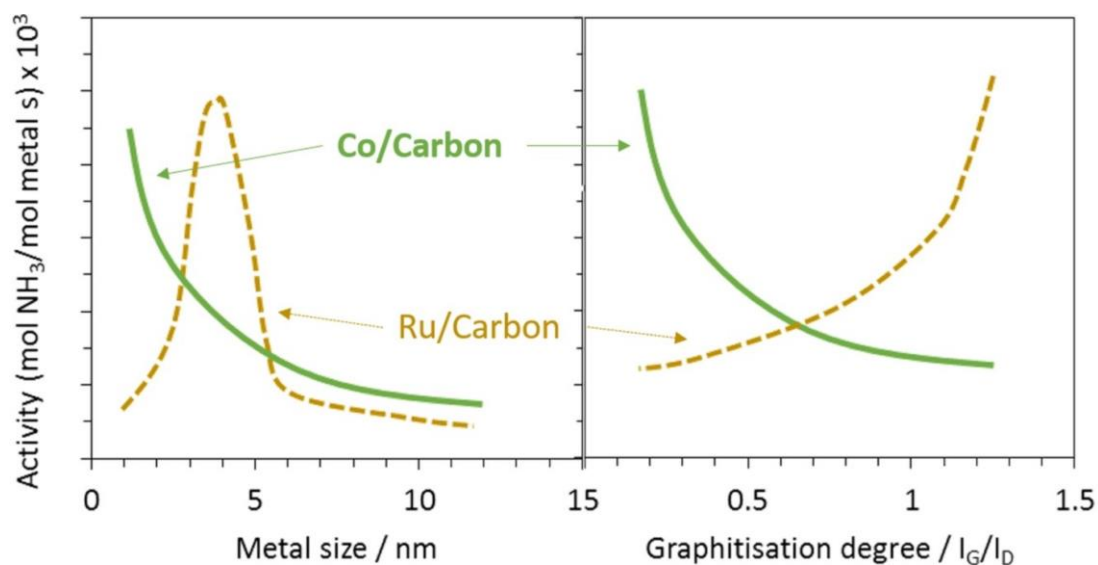
Figure 7: The differing effect of particle size and degree of support graphitisation on the activity of supported Co and Ru catalysts. Reproduced from ref. 73.

Although Cs has been shown to be inactive as a promoter for Co-based catalysts, a number of active promoters have been demonstrated. Czekajło *et al.* have demonstrated that oxides of Al, Ca and K all promote cobalt catalysts but found that Cr and Mn inhibit the reaction.[70] These promoted catalysts were unsupported and prepared by impregnating a Co_3O_4 catalyst precursor with one, two or three nitrate solutions of Al, Ca and K. After reduction and under reaction conditions the catalyst was shown to be the face-centered cubic (FCC) phase Co (as opposed to the HCP exhibited by bulk Co) with the desired combination of CaO, K_2O, and Al_2O_3. The most active catalyst was found to be the triply-promoted catalyst with all three oxides present that achieved nearly 100% conversion at 525 °C.[74]

1.4.4 Bimetallic Catalysts

Bimetallic catalysts are often investigated for their unique properties and in some cases synergy,[75] revealing more active catalysts than is possible with only monometallic catalysts. These bimetallic nanoparticles can take the form of structured particles (such as particles with a distinct core and shell)[75] or alloy particles, although in the latter case, care must be taken to fully investigate the active site as under reaction conditions it is well-reported that metals may segregate and lose the alloyed structure.[75]

As shown in Figure 4, Ru is the most active monometallic catalysts as it fits in a 'goldilocks' region between the two rate determining steps. Many investigations into bimetallic catalysts for ammonia decomposition have the aim of mimicking the attractive properties of Ru using two cheaper metals. Figure 8 shows the volcano-type relationship between metal binding energy and ammonia synthesis activity for a number of monometallic catalysts. In the case of the synthesis reaction, this arises due to the effect of metal binding energy on the rate determining step, N_2 dissociation, and the stability of surface N species. The binding energy of Ru is close to the optimum and therefore the most active metal. Jacobsen *et al.* have employed a rational design method termed "periodic table interpolation" to prepare catalysts that mimic the electronic behaviour of Ru by alloying a metal with a high binding
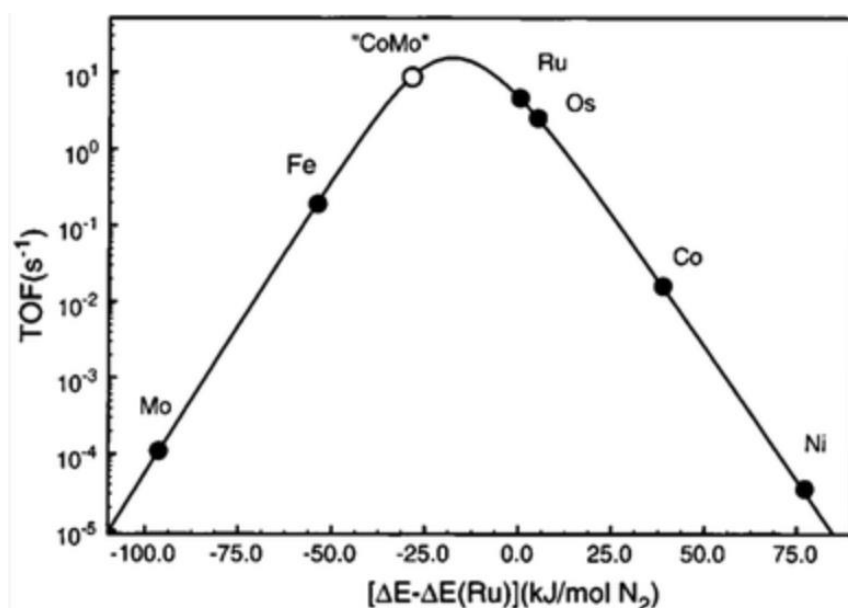
Figure 8: Relationship between N-binding energy and ammonia synthesis activity for various transition metals and an alloy designed by periodic table interpolation. Reproduced from ref. 76.

energy (Co) with a metal that has a low binding energy (Mo).[76] In this way, an alloy with an intermediate binding energy was prepared and was shown to be more active than Ru.

A similar volcano-type relationship has been demonstrated for the decomposition reaction and is shown in Figure 9. In this case the optimum activity is due to the balance between the two rate determining steps. A metal with a high N-binding energy easily cleaves N-H bonds but N recombinative desorption is not facilitated, whereas a metal with a low binding energy is hindered by the N-H scission step of the mechanism. Optimisation of this binding energy using bimetallic catalysts has also been used as a design method for the decomposition reaction.
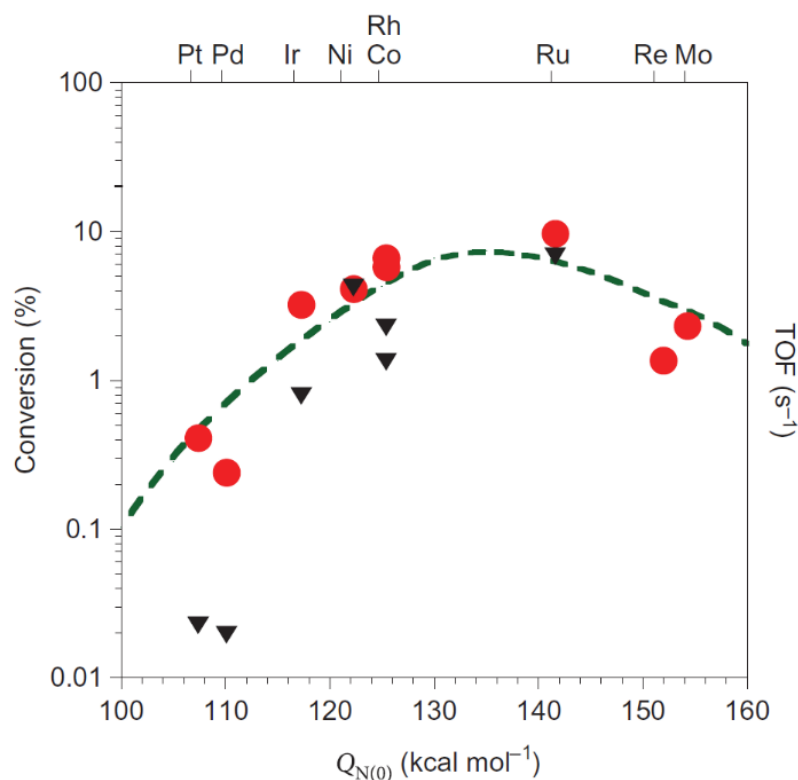
Figure 9: Relationship between N-binding energy and ammonia decomposition conversion. Reproduced from ref. 77.

In 2010, Hansgen *et al.* used DFT calculations to predict bimetallic layered surfaces that would make suitable catalysts. They argue that it is more beneficial to study bimetallic monolayers than alloys, as under reaction conditions many alloys are not thermodynamically stable and will segregate into monolayer structures. These were modelled as three stacked monolayers and notated as M-M-M, with the first layer being the top layer. M-Pt-Pt surfaces

and Pt-M-Pt sub-surfaces were investigated. Ni-Pt-Pt was identified as a suitable surface and using NH_3-TPD, shown that it has potential to be more active than Ru catalysts on the basis of a lower temperature of nitrogen desorption.[77]

In 2011, Hansgen *et al.* tested this model further by investigating Fe-Pt, Co-Pt and Cu-Pt both computationally and experimentally, again by NH_3-TPD.[78] They predicted that surface compositions of Fe-Pt and Co-Pt (i.e. Fe-Pt-Pt and Co-Pt-Pt) would be active for ammonia decomposition, whereas the subsurface compositions (i.e. Pt-Fe-Pt and Pt-Co-Pt) would be inactive. Both surface and subsurface compositions of Cu-Pt were predicted to be inactive. All of these predictions were found to be correct after testing using NH_3-TPD with Co-Pt-Pt decomposing NH_3 at a slightly lower temperature that Fe-Pt-Pt. Both Co-Pt and Fe-Pt were found to be more active than the parent metals, demonstrating a synergistic effect and illustrating the benefits of this approach to bimetallic catalyst design. Although practical catalysts have not been made and tested, these results indicate that core@shell catalysts of Pt@Fe and Pt@Co may be active for this reaction.

The alloying approach to catalyst design has also been used for ammonia decomposition. Duan *et al.* have shown that CoMo/MCM-41 is active for ammonia decomposition, however, unlike for the synthesis reaction, it is not more active than the Ru catalyst.[79] In 2012, Simonsen *et al.* prepared and tested FeNi catalysts based on the rationale of periodic table interpolation.[80] Tests of the monometallic catalysts confirm the expected order of activity as discussed previously: Ru > Ni > Fe. They also tested different gas mixtures by varying the NH_3:H_2 ratio and reported an inhibitory effect due to H_2. This has been widely reported by other groups.[81,82] They report that under both gas compositions the FeNi catalyst is more active than the Fe-only catalyst, however, it is only more active than the Ni-only catalyst in the high concentrations of H_2, in which case it is of comparable activity to Ru. This is due to the effect of NH_3 concentration on optimal binding energy as shown in Figure 6 and demonstrates that while the binding energy may be optimised by a rational design of alloys, the effect of reaction conditions must be considered.

The effect of support was also investigated and it was found that Al_2O_3 and an $MgAl_2O_4$ spinel were more suitable supports than other metal oxides, namely SiO_2, TiO_2 and ZrO_2. It was noted that the effect of metal oxide support on activity is far more significant for FeNi catalysts than Ru. This observation was attributed to the difficulty in preparing small FeNi particles on the less active supports due to sintering and support reduction. This work was expanded by the same group in 2015 when they investigated the effect of support structure on the activity of the $FeNi/Al_2O_3$ catalysts.[83] They report that by preparing an "egg-shell" catalyst (where the active phase is located on the outer surface of catalyst particles), the activity can be enhanced over "egg-white" (where the active phase is present midway into a spherical catalyst particle) and uniform distribution catalysts. This is attributed to better diffusion and heat transfer properties, the latter being especially due to the endothermic nature of the reaction. These catalysts were also shown to be stable over ten hours of reaction.

1.4.5 Summary

It has been shown that ammonia decomposition could offer an energy dense source of hydrogen that is CO_x-free at the point of use. The most active metal for the reaction has been shown to be Ru and this is due to the N-binding energy being balanced between facilitating N-H bond scission and allowing N_2 recombinative desorption, although the latter remains the rate determining step. The activity can be further enhanced by appropriate choice of promoter, such as Ba and Cs, and support, such as CNTs.

Due to the price and scarcity of Ru, research has focussed on preparing Ru-free catalysts with activities comparable to Ru. Two approaches have been taken: utilising promoters and supports to enhance the activity of less active but cheaper metals such as Ni and Co, and preparing bimetallic catalysts with cheaper metals in an effort to mimic the electronic properties of Ru that make it so favourable for this reaction.

The state of the art has been visually summed-up in graphic form in a review by Bell and Torrente-Murciano and is reproduced in Figure 10.[84] Although

great progress has been made in the investigation of alternative catalysts, it is shown that Ru catalysts remain the most active per mole of hydrogen produced per mol of metal per hour. The requirements for a highly active Ru catalyst are well understood: a highly conductive, graphitic support, a particle size between 3-5 nm to maximise B5 sites, and a Cs promoter to facilitate N_2 recombinative desorption. This has led to the development of the
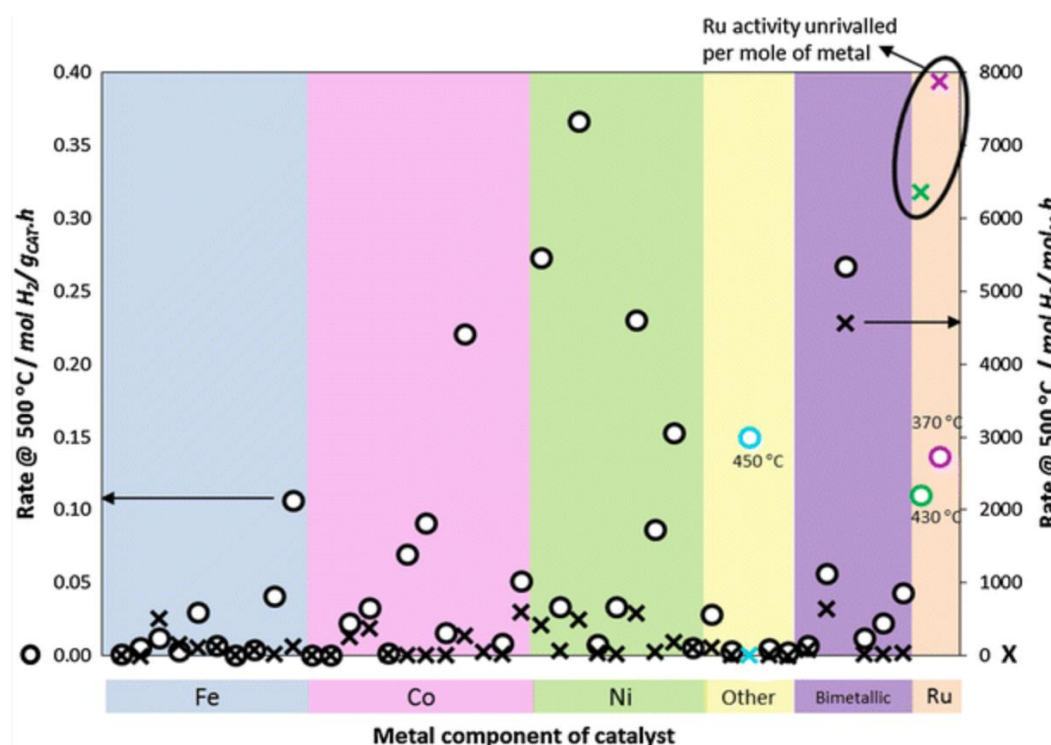
Figure 10: Comparison of ammonia decomposition catalyst from the literature order by active metal component. Reproduced from ref. 84.

7% wt% Ru/gCNT + 4 wt% Cs catalyst at the top right of the chart that is currently the most active ammonia decomposition catalyst reported.

1.5 Aims of the Project

The aims of this project are to prepare novel active catalysts for ammonia decomposition with a focus on cheaper and more abundant metals than Ru. Continuing from the work described above, non-Ru monometallic catalysts will be investigated as well as the use of promotors for these catalysts. Bimetallic catalysts will also be investigated, prepared with the principles of periodic table

interpolation to determine whether this is a robust catalyst design methodology.

1.6   References

1.   NKOSI, B. Hydrochlorination of acetylene using gold catalysts: A study of catalyst deactivation. *J. Catal.* **128**, 366–377 (1991).

2.   Kirkpatrick, W. H., Land, S. & Company, W. P. Patented Aug. 23, 1960. (1960).

3.   Thomas, C. L. Chemistry of Cracking Catalysts. *Ind. Eng. Chem.* **41**, 2564–2573 (1949).

4.   De Stefanis, A., Kaciulis, S. & Pandolfi, L. Preparation and characterization of Fe-MCM-41 catalysts employed in the degradation of plastic materials. *Microporous Mesoporous Mater.* **99**, 140–148 (2007).

5.   Ritter, S. K. A more natural approach to catalysts. *Chem. Eng. News* **95**, 26–32 (2017).

6.   Erisman, J. W., Sutton, M. A., Galloway, J., Klimont, Z. & Winiwarter, W. How a century of ammonia synthesis changed the world. *Nat. Geosci.* **1**, 636–639 (2008).

7.   Laidler, K. J. A glossary of terms used in chemical kinetics, including reaction dynamics (IUPAC Recommendations 1996). *Pure Appl. Chem.* **68**, 149–192 (1996).

8.   Ross, K., Chmiel, J. F. & Ferkol, T. The impact of the Clean Air Act. *J. Pediatr.* **161**, 781–6 (2012).

9.   Williams, M. & Minjares, R. *A technical summary of Euro 6/VI vehicle emission standards.* (2016).

10.   Fritz   Haber   -   Facts.   (2019).   Available   at: https://www.nobelprize.org/prizes/chemistry/1918/haber/facts/. (Accessed: 23rd January 2019)

11.   Carl Bosch - Facts.

12.   Le Chatelier's Principle. *A Dictionary of Chemistry* (2008).

13.   Ertl, G. Surface Science and Catalysis—Studies on the Mechanism of

Ammonia Synthesis: The P. H. Emmett Award Address. *Catal. Rev.* **21**, 201–223 (1980).

14. Emmett, P. H. & Harkness, R. W. The Adsorption of Hydrogen by Iron Synthetic Ammonia Catalysts. *J. Am. Chem. Soc.* **57**, 1631–1635 (1935).

15. Ozaki, A., Taylor, H. & Boudart, M. Kinetics and Mechanism of the Ammonia Synthesis Sciences. *Proc. R. Soc. Lond. A. Math. Phys. Sci.* **258**, 47–62 (1960).

16. TEMKIN & I., M. Kinetics of ammonia synthesis on promoted iron catalysts. *Acta Physiochim. URSS* **12**, 327–356 (1940).

17. Mittasch, A. & Frankenburg, W. Early Studies of Multicomponent Catalysts. *Adv. Catal.* **2**, 81–104 (1950).

18. Dumesic, J. A., Topsoe, H Khammouma, S. and B. M. Surface, Catalytic and Magnetic Properties of Small Iron Particles. *J. Catal.* **37**, 503–512 (1975).

19. Strongin, D. R. *THE IMPORTANCE OF C7 SITES AND SURFACE ROUGHNESS IN THE AMMONIA SYNTHESIS REACTION OVER IRON.* (1986).

20. Somorjai, G. A. & Materer, N. Surface structures in ammonia synthesis. *Top. Catal.* **1**, 215–231 (1994).

21. Rayment, T., Schlögl, R., Thomas, J. M. & Ertl, G. Structure of the ammonia synthesis catalyst. *Nature* **315**, 311–313 (1985).

22. Ertl, G., Lee, S. B. & Weiss, M. Adsorption of nitrogen on potassium promoted Fe(111) and (100) surfaces. *Surf. Sci.* **114**, 527–545 (1982).

23. Benner, G. S. *et al.* SUPPLEMENTAL AMMONIA SYNTHESIS. (1986).

24. Foster, A. I., James, P. G., McCarroll, J. J. & Tennison, S. R. Process for the synthesis of ammonia using catalysts supported on graphite containing carbon. (1979).

25. Forni, L., Molinari, D., Rossetti, I. & Pernicone, N. Carbon-supported

promoted Ru catalyst for ammonia synthesis. *Appl. Catal. A Gen.* **185**, 269–275 (1999).

26. Jacobsen, C. J. H. *et al.* Structure sensitivity of supported ruthenium catalysts for ammonia synthesis. *J. Mol. Catal. A Chem.* **163**, 19–26 (2000).

27. Kowalczyk, Z., Krukowski, M., Raróg-Pilecka, W., Szmigiel, D. & Zielinski, J. Carbon-based ruthenium catalyst for ammonia synthesis: Role of the barium and caesium promoters and carbon support. *Appl. Catal. A Gen.* **248**, 67–73 (2003).

28. Conway, E. NASA - What's in a Name? Global Warming vs. Climate Change. Available at: https://www.nasa.gov/topics/earth/features/climate_by_any_other_name.html. (Accessed: 24th January 2019)

29. Global Temperature | Vital Signs – Climate Change: Vital Signs of the Planet. Available at: https://climate.nasa.gov/vital-signs/global-temperature/. (Accessed: 31st January 2019)

30. Verne, J. *The Mysterious Island.* (1874).

31. Andújar, J. M. & Segura, F. Fuel cells: History and updating. A walk along two centuries. *Renew. Sustain. Energy Rev.* **13**, 2309–2322 (2009).

32. Zou, X. & Zhang, Y. Noble metal-free hydrogen evolution catalysts for water splitting. *Chem. Soc. Rev.* **44**, 5148–5180 (2015).

33. Ni, M., Leung, M. K. H., Leung, D. Y. C. & Sumathy, K. A review and recent developments in photocatalytic water-splitting using TiO2 for hydrogen production. *Renew. Sustain. Energy Rev.* **11**, 401–425 (2007).

34. Maeda, K. *et al.* Photocatalyst releasing hydrogen from water. *Nature* **440**, 295–295 (2006).

35. Bard, A. J. & Fox, M. A. *Artificial Photosynthesis: Solar Splitting of Water to Hydrogen and Oxygen. Acc. Chem. Res* **28**, (1995).

36. Hydrogen-powered vehicles on horizon. *Washington Times* (2009). Available at: https://www.washingtontimes.com/news/2009/aug/24/hydrogen-powered-vehicles-on-horizon/. (Accessed: 24th January 2019)

37. Hydrogen-powered Aston Martin completes Nürburgring 24 hours. *Autocar* Available at: https://www.autocar.co.uk/car-news/motorsport/hydrogen-powered-aston-martin-story-behind-racer. (Accessed: 24th January 2019)

38. Collins, D. J. & Zhou, H.-C. Hydrogen storage in metal–organic frameworks. *J. Mater. Chem.* **17**, 3154 (2007).

39. Suh, M. P., Park, H. J., Prasad, T. K. & Lim, D.-W. Hydrogen Storage in Metal–Organic Frameworks. *Chem. Rev.* **112**, 782–835 (2012).

40. Rosi, N. L. Hydrogen Storage in Microporous Metal-Organic Frameworks. *Science (80-.).* **300**, 1127–1129 (2003).

41. Kesanli, B. *et al.* Highly Interpenetrated Metal-Organic Frameworks for Hydrogen Storage. *Angew. Chemie* **117**, 74–77 (2005).

42. Liu, Y. *et al.* Assembly of Metal–Organic Frameworks (MOFs) Based on Indium-Trimer Building Blocks: A Porous MOF with soc Topology and High Hydrogen Storage. *Angew. Chemie* **119**, 3342–3347 (2007).

43. Panella, B., Hirscher, M., Pütter, H. & Müller, U. Hydrogen Adsorption in Metal–Organic Frameworks: Cu-MOFs and Zn-MOFs Compared. *Adv. Funct. Mater.* **16**, 520–524 (2006).

44. Panella, B., Hirscher, M. & Roth, S. Hydrogen adsorption in different carbon nanostructures. *Carbon N. Y.* **43**, 2209–2214 (2005).

45. Cheng, H.-M., Yang, Q.-H. & Liu, C. Hydrogen storage in carbon nanotubes. *Carbon N. Y.* **39**, 1447–1454 (2001).

46. Dillon, A. C. *et al.* Storage of hydrogen in single-walled carbon nanotubes. *Nature* **386**, 377–379 (1997).

47. Zaluska, A., Zaluski, L. & Ström-Olsen, J. O. Structure, catalysis and

atomic reactions on the nano-scale: a systematic approach to metal hydrides for hydrogen storage. *Appl. Phys. A Mater. Sci. Process.* **72**, 157–165 (2001).

48. Zaluska, A., Zaluski, L. & Ström–Olsen, J. . Nanocrystalline magnesium for hydrogen storage. *J. Alloys Compd.* **288**, 217–225 (1999).

49. Sakintuna, B., Lamari-Darkrim, F. & Hirscher, M. Metal hydride materials for solid hydrogen storage: A review. *Int. J. Hydrogen Energy* **32**, 1121–1140 (2007).

50. Joó, F. Breakthroughs in Hydrogen Storage-Formic Acid as a Sustainable Storage Material for Hydrogen. *ChemSusChem* **1**, 805–808 (2008).

51. Fellay, C., Dyson, P. & Laurenczy, G. A Viable Hydrogen-Storage System Based On Selective Formic Acid Decomposition with a Ruthenium Catalyst. *Angew. Chemie Int. Ed.* **47**, 3966–3968 (2008).

52. Olah, G. A. Beyond Oil and Gas: The Methanol Economy. *Angew. Chemie Int. Ed.* **44**, 2636–2639 (2005).

53. Engstr, A. Determination of acceptable contaminant levels for PEM fuel cell stacks and poisoning mitigation strategies. (2014).

54. García-García, F. R., Ma, Y. H., Rodríguez-Ramos, I. & Guerrero-Ruiz, A. High purity hydrogen production by low temperature catalytic ammonia decomposition in a multifunctional membrane reactor. *Catal. Commun.* **9**, 482–486 (2008).

55. Yin, S.-F. *et al.* Investigation on the catalysis of COx-free hydrogen generation from ammonia. *J. Catal.* **224**, 384–396 (2004).

56. Ertl, G. & Huber, M. Mechanism and kinetics of ammonia decomposition on iron. *J. Catal.* **61**, 537–539 (1980).

57. Tsai, W. & Weinberg, W. H. Steady-state decomposition of ammonia on the ruthenium(001) surface. *J. Phys. Chem.* **91**, 5302–5307 (1987).

58. Shustorovich, E. & Bell, A. T. Synthesis and decomposition of ammonia

on transition metal surfaces: bond-order-conservation-Morse-potential analysis. *Surf. Sci.* **259**, 0–5 (1991).

59. Ganley, J. C., Thomas, F. S., Seebauer, E. G. & Masel, R. I. A priori catalytic activity correlations: The difficult case of hydrogen production from ammonia. *Catal. Letters* **96**, 117–122 (2004).

60. Yin, S. F., Xu, B. Q., Wang, S. J. & Au, C. T. Nanosized Ru on high-surface-area superbasic ZrO2-KOH for efficient generation of hydrogen via ammonia decomposition. *Appl. Catal. A Gen.* **301**, 202–210 (2006).

61. Raróg-Pilecka, W. *et al.* Carbon-supported ruthenium catalysts for NH3synthesis doped with caesium nitrate: Activation process, working state of Cs-Ru/C. *J. Catal.* **239**, 313–325 (2006).

62. Szmigiel, D., Raróg-Pilecka, W., Miśkiewicz, E., Kaszkur, Z. & Kowalczyk, Z. Ammonia decomposition over the ruthenium catalysts deposited on magnesium-aluminum spinel. *Appl. Catal. A Gen.* **264**, 59–63 (2004).

63. Hill, A. K. & Torrente-Murciano, L. In-situ H2 production via low temperature decomposition of ammonia: Insights into the role of cesium as a promoter. *Int. J. Hydrogen Energy* **39**, 7646–7654 (2014).

64. Hill, A. K. & Torrente-Murciano, L. Low temperature H2 production from ammonia using ruthenium-based catalysts: Synergetic effect of promoter and support. *Appl. Catal. B Environ.* **172**–**173**, 129–135 (2015).

65. Li, X. K., Ji, W. J., Zhao, J., Wang, S. J. & Au, C. T. Ammonia decomposition over Ru and Ni catalysts supported on fumed SiO 2, MCM-41, and SBA-15. *J. Catal.* **236**, 181–189 (2005).

66. Zheng, W., Zhang, J., Xu, H. & Li, W. NH3decomposition kinetics on supported Ru clusters: Morphology and particle size effect. *Catal. Letters* **119**, 311–318 (2007).

67. Zhang, J., Xu, H. & Li, W. Kinetic study of NH3 decomposition over Ni nanoparticles: The role of la promoter, structure sensitivity and

compensation effect. *Appl. Catal. A Gen.* **296**, 257–267 (2005).

68. Liu, H., Wang, H., Shen, J., Sun, Y. & Liu, Z. Promotion effect of cerium and lanthanum oxides on Ni/SBA-15 catalyst for ammonia decomposition. *Catal. Today* **131**, 444–449 (2008).

69. Zheng, W., Zhang, J., Ge, Q., Xu, H. & Li, W. Effects of CeO2 addition on Ni/Al2O3 catalysts for the reaction of ammonia decomposition to hydrogen. *Appl. Catal. B Environ.* **80**, 98–105 (2008).

70. Lendzion-Bielun, Z., Narkiewicz, U. & Arabczyk, W. Cobalt-based catalysts for ammonia decomposition. *Materials (Basel).* **6**, 2400–2409 (2013).

71. Zhang, J., Comotti, M., Schüth, F., Schlögl, R. & Su, D. S. Commercial Fe- or Co-containing carbon nanotubes as catalysts for NH3 decomposition. *Chem. Commun. (Camb).* 1916–1918 (2007). doi:10.1039/b700969k

72. Boisen, A., Dahl, S., Nørskov, J. K. & Christensen, C. H. Why the optimal ammonia synthesis catalyst is not the optimal ammonia decomposition catalyst. *J. Catal.* **230**, 309–312 (2005).

73. Torrente-Murciano, L., Hill, A. K. & Bell, T. E. Ammonia decomposition over cobalt/carbon catalysts—Effect of carbon support and electron donating promoter on activity. *Catal. Today* **286**, 131–140 (2017).

74. Czekajło, Ł. & Lendzion-Bieluń, Z. Effect of preparation conditions and promoters on the structure and activity of the ammonia decomposition reaction catalyst based on nanocrystalline cobalt. *Chem. Eng. J.* **289**, 254–260 (2016).

75. Singh, A. K. & Xu, Q. Synergistic Catalysis over Bimetallic Alloy Nanoparticles. *ChemCatChem* **5**, 652–676 (2013).

76. Jacobsen, C. J. H. *et al.* Catalyst design by interpolation in the periodic table: Bimetallic ammonia synthesis catalysts [2]. *J. Am. Chem. Soc.* **123**, 8404–8405 (2001).

77. Hansgen, D. a, Vlachos, D. G. & Chen, J. G. Using first principles to

predict bimetallic catalysts for the ammonia decomposition reaction. *Nature chemistry* **2**, 484–489 (2010).

78.   Hansgen, D. A., Thomanek, L. M., Chen, J. G. & Vlachos, D. G. Experimental and theoretical studies of ammonia decomposition activity on Fe-Pt, Co-Pt, and Cu-Pt bimetallic surfaces. *J. Chem. Phys.* **134**, (2011).

79.   Duan, X., Qian, G., Zhou, X., Chen, D. & Yuan, W. MCM-41 supported CoMo bimetallic catalysts for enhanced hydrogen production by ammonia decomposition. *Chem. Eng. J.* **207**–**208**, 103–108 (2012).

80.   Simonsen, S. B., Chakraborty, D., Chorkendorff, I. & Dahl, S. Alloyed Ni-Fe nanoparticles as catalysts for NH3 decomposition. *Appl. Catal. A Gen.* **447**–**448**, 22–31 (2012).

81.   Prasad, V., Karim, A. M., Arya, A. & Vlachos, D. G. Assessment of Overall Rate Expressions and Multiscale, Microkinetic Model Uniqueness via Experimental Data Injection: Ammonia Decomposition on Ru/γ-Al $_2$ O $_3$ for Hydrogen Production. *Ind. Eng. Chem. Res.* **48**, 5255–5265 (2009).

82.   García-Bordejé, E., Armenise, S. & Roldán, L. Toward Practical Application Of H $_2$ Generation From Ammonia Decomposition Guided by Rational Catalyst Design. *Catal. Rev.* **56**, 220–237 (2014).

83.   Silva, H. *et al.* Synthesis and characterization of Fe-Ni/χ-Al2O3egg-shell catalyst for H2generation by ammonia decomposition. *Appl. Catal. A Gen.* **505**, 548–556 (2015).

84.   Bell, T. E. & Torrente-Murciano, L. H2 Production via Ammonia Decomposition Using Non-Noble Metal Catalysts: A Review. *Top. Catal.* (2016). doi:10.1007/s11244-016-0653-4

2 Experimental

2.1 Materials Used

The following materials were used during this project. All were used as received.

- 5000 ppm NH_3/Ar (BOC)
- Ar (BOC)
- 5%H_2/Ar (BOC)
- γ-Al_2O_3 (Sigma-Aldrich, nanopowder <50 nm particle size)
- Fe(acac)$_3$ (Sigma-Aldrich, 99.9%)
- Pt(acac)$_2$ (Alfa-Aesar, Pt 48.0% min.)
- Pd(acac)$_2$ (Sigma-Aldrich, 99%)
- Co(acac)$_2$ (Sigma-Aldrich, 97%)
- Ni(acac)$_2$ (Sigma-Aldrich, 95%)
- Ru(acac)$_3$ (Sigma-Aldrich, 97%)
- $RuCl_3$.xH_2O (Sigma-Aldrich, *ReagentPlus®*)
- 5 wt.% Ru/C (Sigma-Aldrich)
- $Fe(NO_3)_3$.xH_2O (Sigma-Aldrich, ≥98%)
- $CsNO_3$ (Sigma-Aldrich, 99.9%)

2.2 Catalyst Preparation

This section details the catalyst preparation techniques carried out during this work. Catalyst preparation is of utmost importance in heterogeneous catalysis as the preparation method will have a large effect on the activity of the catalyst when tested. The preparation method affects properties such as metal particle size, distribution and morphology, as well as the introduction of impurities; all of these things can be the difference between a highly active catalyst and completely inactive catalyst. Two impregnation techniques were used to

prepare catalysts during this work and are described in more detail below, however, there are a plethora of methods not mentioned in this work. These range from widely used methods such as colloidal preparations,[1] to more specific techniques developed to study model surfaces and particles.[2]

2.2.1 Wet Impregnation

Wet impregnation is a simple and commonly used catalyst preparation technique that can be easily scaled up for industrial use. In wet impregnation, metal precursors (typically salts such as metal nitrates or chlorides) are dissolved in an excess of suitable solvent (typically water or common organic solvents such as ethanol). The support is then added to this solution and the metal binds to the surface. Surfaces are interfaces with lower co-ordination than the bulk and are therefore higher in energy. Metal ions will interact with the surface to increase the co-ordination of surface atoms, thereby lowering the overall energy of the system. The excess solvent is removed either by filtration or evaporation. Catalysts prepared by wet impregnation typically exhibit small, well-dispersed nanoparticles, however care must be taken when selecting appropriate metal salts, as counter-ion species such as Cl^-, may also persist on the surface and act as poisons.

Experimental

Fe-Cs/Al$_2$O$_3$ Catalysts

$Fe(NO_3)_3 \cdot xH_2O$ (5 wt%) and $CsNO_3$ (0.5, 1 and 2 mol eq.) were dissolved in deionised water and stirred in a silicone oil bath. Al_2O_3 was added and the resultant suspension was heated at 80 °C until the excess solvent was removed and the catalyst resembled a thick paste. This was dried at 110 °C for 16 h. The as-prepared catalyst was then reduced in a tube furnace at 550 °C for 3 h with a heat ramp of 10 °C/min under a flow of 5% H_2/Ar.

2.2.2 Chemical Vapour Impregnation (CVI)

Chemical vapour impregnation (CVI) is a solvent-free preparation method pioneered in Cardiff by M. M. Forde in 2011.[3] CVI uses metal acetylacetonate $(M(acac)_x)$ precursors that have a high vapour pressure that are sublimed onto

the support, disregarding the need for a solvent. CVI has been shown to produce catalysts with small, evenly-distributed nanoparticles with a narrow particle size distribution.[4] In 2017, Bowker and co-workers also demonstrated how precious metal – base metal alloy particles can be readily prepared.[5] Figure 1 illustrates a typical CVI preparation set up.
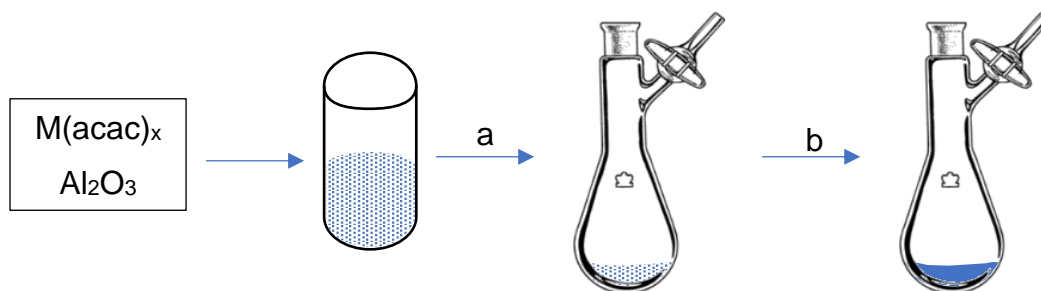
Figure 1: Schematic of a CVI preparation. (a) Metal acac precursor(s) and support and thoroughly mixed and added to a Schlenk flask; (b) heating under vacuum at 140 °C for 1 h.

Experimental

The appropriate masses of $M(acac)_x$ precursor and support were accurately weighed and well mixed in a vial before being transferred to a Schlenk tube. The mixture was then heated to 140 °C under vacuum for 1 h. The resultant catalyst was then reduced in a tube furnace at 550 °C for 3 h with a heat ramp of 10 °C/min under a flow of 5% H_2/Ar.

2.2.3 Precipitation Methods

Precipitation methods are widely used to produce both supported nanoparticle catalysts and metal oxide or mixed metal oxide catalysts. They are easily scaled up and a number of industrial catalysts, such as Cu/ZnO for methanol synthesis, are prepared by precipitation methods.[6] Deposition-precipitation is a method for preparing supported metal nanoparticles with the support being added as a solid to the metal solution and the nanoparticles precipitating onto it. This is in contrast to co-precipitation where two or more metal solutions are mixed and precipitate simultaneously. In this project, co-precipitation was used to prepare CoMo oxide that can be used as a catalyst precursor for ammonia decomposition.

Experimental

Calculated quantities of ammonium molybdate tetrahydrate $((NH_4)_6Mo_7O_{24}\cdot 4H_2O)$ and cobalt acetate $(Co(CH_3CO_2)_2\cdot 4H_2O)$ were dissolved in deionised water to give an equimolar solution of cobalt and molybdenum ions with an overall metal concentration of 0.2 M.

For analysis of the effects of pH, this solution was slowly fed into the reaction vessel, where the solution was heated to 60 °C and stirred vigorously. The pH was set to the desired level by the addition of an ammonium hydroxide solution. To ensure stability in the pH throughout the reaction, a Metrohm Autotitrator was used. For the catalyst prepared without pH control, the solutions were heated separately to 60 °C and then mixed under stirring for 1 h.

2.3   Catalyst Characterisation

2.3.1   Introduction to X-ray Characterisation

A number of the characterisation methods used in this work use x-ray radiation for analysis so a short introduction as to why X-rays are used and how they are produced is presented in this section. X-rays have a wavelength in the order of Ångstroms and can therefore be used to for bulk characterisation techniques such as diffraction as this is in the same range as lattice spacing of solids. X-ray photons also possess sufficient energy to emit electrons from atomic shells and can therefore be used for spectroscopic techniques.

X-rays are generated in an X-ray tube. This is a vacuum tube in which electrons from a cathode are accelerated using a high voltage into a 'target' at the anode position. Typical target materials include Cu and Al. On colliding with the anode, the electron accelerates other species in the target (e.g. ions, nuclei) and electromagnetic radiation is given off in the form of X-rays. Two forms of X-ray radiation are given off: the first is called *Bremsstrahlung* – also called continuous X-rays – and these are due to deceleration of the electron

(*bremsstrahlung* is a contraction of two German words *Bremen* and *strahlung*, meaning "to brake" and "radiation", respectively) and appears on the X-ray spectrum as a smooth, continuous, background radiation. The second form of radiation arises when an electron from the beam removes a core electron from the target and creates a hole or vacancy. An electron from a higher quantum shell may fill this hole and the difference in energy is released as an X-ray of specific wavelength and energy, for example Cu Kα radiation, a common source for XRD, has an energy of 8.04 eV and a wavelength of 0.154 nm. These characteristic wavelengths and energies are the basis for X-ray characterisation techniques and are used extensively in the equations governing them. Figure 2 shows an X-ray spectrum consisting of both types of radiation.
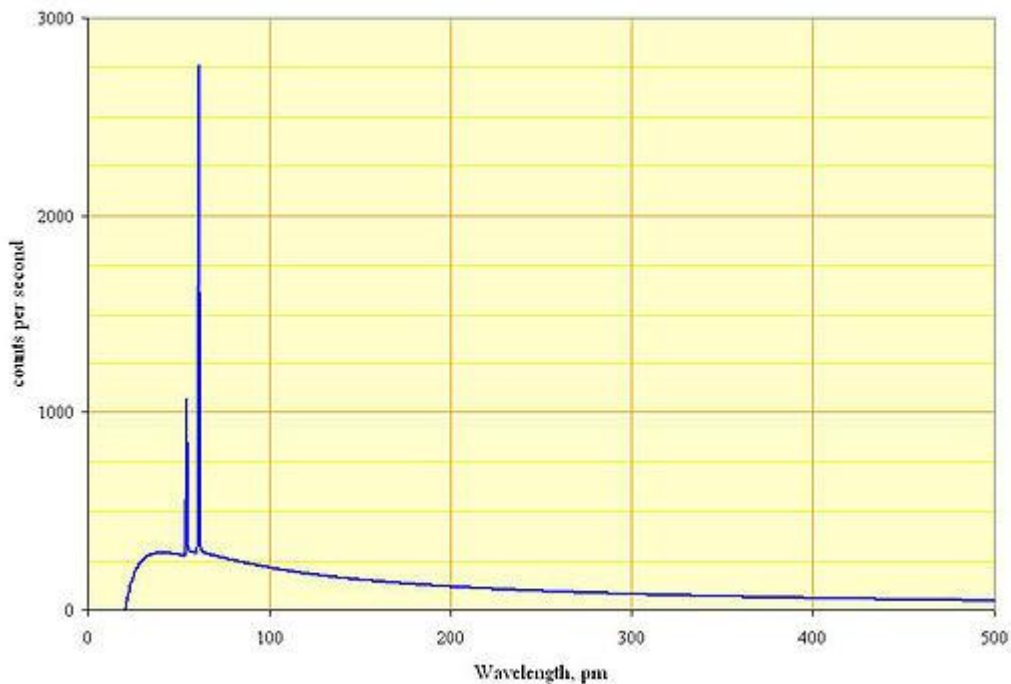
Figure 2: X-ray spectrum from an x-ray tube using a Rhodium target. The smooth, curved baseline is the continuous Bremsstrahlung radiation and the sharp lines are the K-line radiations. Reproduced from Wikimedia Commons

Radiation notation is based on which shell a hole is created in and which shell the electron filling it is from. In this notation, the shells following the quantum numbers 1, 2, 3... are called K, L, M... In the above example of Kα radiation, the K is describing where the hole is formed (the K shell, or innermost electron shell) and the α indicates that the electron filling the hole has come from the

next quantum shell (i.e. L -> K). If the hole were filled by an electron two shells away (i.e. M -> K) it would be Kβ radiation. Different characterisation techniques use different x-ray sources and radiation and these are discussed in the specific sections ahead.

2.3.2 Electron Microscopy (SEM/TEM/STEM)

The ability to see the surface of a catalyst and identify defects, measure the size of particles directly as opposed to calculate it indirectly, and to calculate the particle size distribution can only be achieved by imaging the catalyst itself. In electron microscopy (EM) a high-energy electron beam is focussed onto a mounted sample and the resultant changes are detected using a range of detectors. Figure 3 illustrates a number of the interactions that occur to the sample due to the electron beam. Some electrons will pass through the sample without suffering energy loss and these are called transmitted electrons. The number of these depends on sample thickness. Some electrons will lose energy due to a series of inelastic collision and these are called secondary electrons. Backscattered electrons arise when an electron hits an atom and is elastically scattered directly back, the number of these depends on the size of the atom. X-Rays may also be generated due to the electron beam through the means described in 2.3.1.
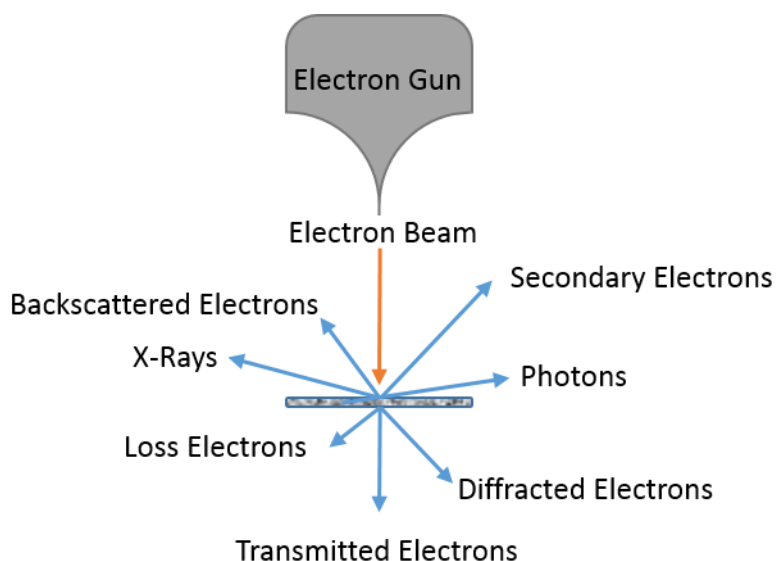
Figure 3: Interaction of the electron beam with a sample. A number of interactions occur (not all are illustrated) and give rise to the different modes available with electron microscopy

EM can be operated in many modes, each detecting a different effect of the electron beam. Examples of these modes include scanning electron microscopy (SEM), transmission electron microscopy (TEM) or a combination of these techniques (STEM). Schematics illustrating the differences in microscope are shown in Figure 4. SEM uses a focussed energy beam that rasters across the sample surface, collecting either the secondary or backscattered electrons. Use of the two types of detectors can be complementary and extremely helpful. When detecting secondary electrons, intensity is related to surface orientation, meaning surfaces facing the electron beam appear brighter than those oriented away, giving structural information. Using a backscattered detector, the contrast arises from atomic mass. The heavier an atom is, the more likely it is to backscatter electrons meaning that heavier elements appear as brighter in the image. By utilising both it is possible to get an idea of the orientation and composition of a sample using SEM.
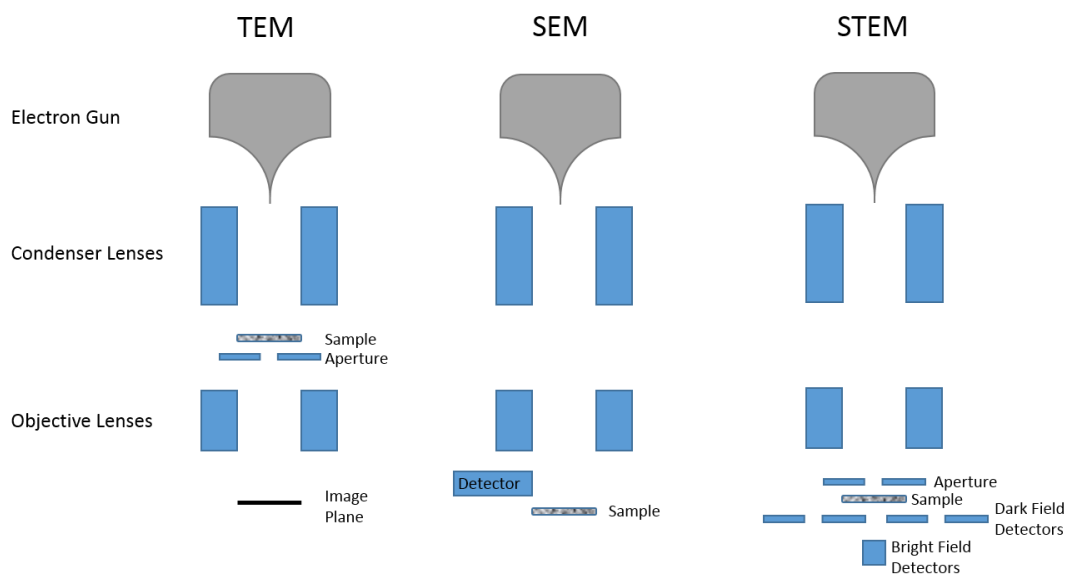
Figure 4: Schematics of three types of EM

TEM utilises the transmitted and diffracted electrons to build up two types of images; dark-field and bright-field. The bright-field image is created from the transmitted electrons whose intensity depends on the thickness and density of the sample. Dark-field images are obtained from the diffracted electrons collected by the ring shaped annular dark field (ADF) detectors, or high-angle annular dark field (HAADF) detectors if the angle is greater than that at which Bragg diffraction occurs. STEM is a combination of both techniques and offers

the greatest insight into the catalyst by using a focussed electron beam (<1 nm) and rastering it across the sample surface.

Two of the main limitations of electron microscopy are the sample size and the damage from the electron beam. As EM images only a small area of a catalyst it is important to ensure that this area is representative of the whole sample. For this reason, numerous regions should be imaged from throughout a sample. This also applies when measuring particle size; in order to get a reliable mean particle size many (>100) particles should be measured from different regions of the sample and a particle size distribution should also be produced. The electron beam is very powerful (>100 keV) and because of this damage can be caused to a sample under observation. For example, low and medium atomic number elements are liable to electron beam sputtering whereby they are ejected from the surface and into the vacuum of the microscope.[7]

2.3.2.1   Energy Dispersive X-Ray Spectroscopy (EDX)

Bombarding a sample with an electron beam produces X-ray radiation as described in 2.3.1 and shown in Figure 3. As mentioned previously, X-ray radiation is characteristic of the specific element it is emitted from and this forms the basis of the electron microscope based elemental analysis technique, EDX (which is also referred to as EDS). Using the X-rays emitted from a sample under the electron beam of an EM it is possible to determine the elemental composition of a sample. When used in conjunction with the other imaging methods mentioned, this is an incredibly powerful tool for the researcher as a vast array of information about the active site such as morphology, structure and composition can be collected for the same site, however, care must be taken as the structure may not be the same as under reaction conditions. This allows for a detailed understanding of the active site and elucidation of structure-activity correlations.

Experimental

SEM and EDX in chapter 4.2.1 was carried out by Dr Tom Davies in Cardiff. Samples for examination by SEM were prepared by mounting 1 cm^3 steel sections on SEM stages using carbon tape. SEM images were collected using

SE and BSE detectors on a MAIA3 TECSAM microscope operating at 15 kV. This instrument was also equipped with a detector for energy dispersive X-ray spectroscopy (EDX).

STEM and TEM were carried out by Li Lu in Lehigh University. Samples for examination by STEM were prepared by dry dispersing the catalyst powder onto a holey carbon film supported by a 300 mesh copper TEM grid. Bright field (BF) and high angle annular dark field (HAADF) STEM images were taken using an aberration-corrected JEM ARM-200CFmicroscope operating at 200 kV. This instrument was also equipped with a JEOL Centurio silicon drift detector for X-ray energy dispersive spectroscopy (XEDS). Particle size distribution analysis was performed from analysis of the HAADF electron micrographs using ImageJ.

2.3.3 Powder X-Ray Diffraction (P-XRD)

X-ray diffraction is a bulk technique that is used for the analysis of crystal structures in solid samples. Using XRD, solid phases can be identified, changes in phase can be followed and particle sizes can be estimated. XRD is used in many fields such as for mineral identification in geology[8] and protein structure determination in biology.[9] In catalysis, XRD is used to identify (or confirm) support material and/or phase as well as to investigate the presence nanoparticles and estimate their size.

For a material to be suitable for XRD it must be crystalline and therefore possess long-range order. X-ray radiation, typically from a Cu Kα source, is elastically scattered by the ordered lattice and if it is in-phase, will constructively interfere. These constructively interfered X-rays are collected by a detector throughout a range of angles (typically 5 – 80 °). A standard XRD machine consists of a fixed position x-ray source and a scanning detector. Using the Bragg equation (Equation 4) it is possible to relate x-ray diffraction to lattice spacing. These lattice spacings and angles are characteristic to the solid being analysed. Amorphous solids are not suitable for analysis by XRD because the lack of long-range order means there is no in-phase diffraction

leading to no constructive interference and therefore no intensity change is observed.

Equation 4: Bragg's Law

$$n\lambda = 2d \sin\theta$$

Where:

n is the order of the reflection (an integer)

λ is the wavelength of the x-rays

d is the lattice spacing

θ is the angle of diffraction

Similarly, for nanoparticles to be observed on the support they must be larger than ~ 5 nm (although recent advances in technology, discussed later, allow nanoparticles to be measured down to 1 – 2 nm). This is because even if the nanoparticle is crystalline, due its small size means there will be very little constructive interference due to a relatively low-number of lattice planes. Even in particles that are detectable by XRD, line-broadening occurs in particles < 100 nm, however, this has its advantages. The Scherrer formula, shown in Equation 5, can be used to calculate crystallite size from the diffraction angle and the full-width-half-maximum (FWHM) of a peak. It is important to note, however, that although use of the Scherrer equation can give a good indication of particle size it is an average over the whole sample and should not be used as a replacement for full particle size analysis using microscopy, merely as a quick method to aid in initial analysis.

Equation 5: Scherrer Equation

$$\tau = \frac{K\lambda}{\beta \cos\theta}$$

Where:

τ is the mean crystallite size

K is a constant known as the 'shape factor' typically taken as 1

β is the peak width measured as the FWHM

θ is the Bragg angle.

One method of measuring smaller particles is through the use of different X-ray sources. According to the Scherrer equation, both X-ray wavelength and peak angle relate to peak broadening, therefore, by using an X-ray source with a lower wavelength (such as Mo K*α λ* = 0.07 nm) diffraction patterns from smaller particles can be obtained. Another method is the use of alternative detectors. Particles < 5 nm are seldom detected due to a low signal-to-noise ratio, however, recent advances have led to silicon strip detectors which increase the detection area and greatly increase the signal-to-noise. This allows detection of nanoparticles down to 1 nm.[10]

Experimental

Samples were placed in metal sample holders and patterns were analysed using a Panalytical X'Pert diffractometer with a Cu X-ray source operating at 40 kV and 40 mA. Patterns were attained by 40 minute scans over a range of 5-80 ° 2θ angles. Phase identification was performed by matching experimental patterns against entries from the International Centre for Diffraction Data (ICDD) database.

2.3.4 X-Ray Photoelectron Spectroscopy (XPS)

X-Ray Photoelectron Spectroscopy (XPS) is a powerful surface technique that can provide data on properties such as oxidation state and surface composition as well as more in-depth studies such as depth-profiling of samples and dispersion of nanoparticles.
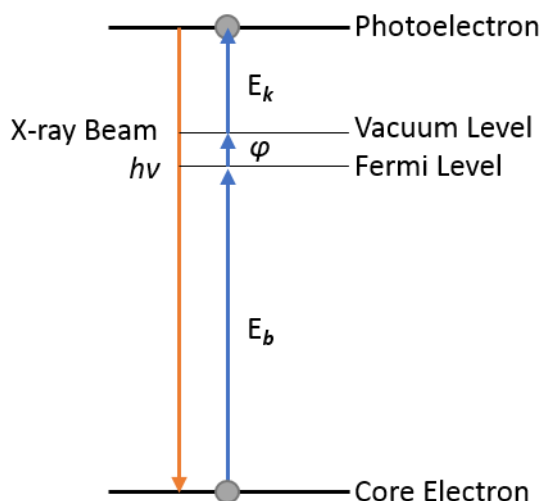
Figure 5: Photoemission of a core electron by an x-ray beam. The terms of the photoelectric equation are illustrated

The theory of XPS is based on Einstein's photoelectric effect (Equation 6). When an atom absorbs a photon of sufficient energy a photoelectron will be emitted from either the core or valence band (Figure 5). As shown in the equation, by measuring the kinetic energy of these photoelectrons it is possible to calculate the binding energy of the photoelectron. Core photoelectrons, from the inner quantum shells which are not involved in chemical bonding, have binding energies that are specific to the atom from which they are ejected. A typical XP spectrum is a plot of the intensity of these photoelectrons as a function of their binding energy.

Equation 6: The Photoelectric Effect

$$E_k = hv - E_b - \varphi$$

Where:

E_k is the kinetic energy of a photoelectron

h is Planck's constant

v is the frequency of the radiation

E_b is the binding energy of the photoelectron (relative to the Fermi level of the atom)

φ is the work function of the spectrometer

A standard XPS machine consists of an x-ray beam, typically from a Mg Kα or Al Kα source, focussed onto a solid sample on a stage. Ejected photoelectrons are then detected by a detector which simultaneously analyses the kinetic energy of the photoelectron in order to calculate the binding energy, and measures the intensity of ejected photoelectrons. Current systems operate under high or ultra-high vacuum, however, state-of-the-art machines are beginning to be manufactured that can perform near-ambient pressure measurements.

Although binding energies are characteristic of each element, this does not mean they are static. The chemical state of the atom can vary the binding energy up to ~3 eV meaning that changes in oxidation state and other chemical changes such as ligands can be investigated using XPS.[11] This is due to the changes in attraction the core electrons feel; in an oxidised form, fewer electrons are feeling a stronger positive charge. This typically leads to an increase in binding energy with increasing oxidation. A similar trend is observed with increasing electronegativity of ligands (E_b: $FeBr_3$ = 710.0 eV; $FeCl_3$ = 711.1 eV; FeF_3 = 714.0 eV).[12] Other factors that can affect the binding energy are the size of nanoparticle and the support material used. The energy of the ejected electron is the difference in energy between the *N* electron initial state and the *N-1* ionized final state, therefore influences such as the screening of core electrons are referred to as initial state effects and the screening of a created hole by the environment are called final state effects.[13]

Dispersion of nanoparticles on the support material can also be investigated using XPS. This is done by looking at the ratio of particle intensity (I_p) and support intensity (I_s). As XPS is a surface-sensitive technique, small well-dispersed nanoparticle will appear as more intense compared to the support they are covering, whereas the intensity of large, ill-dispersed nanoparticles will be lower as less of the support surface will be covered. Also, in very large particles metal deep in the core of the particle will not be detected by XPS (again, because it is a surface-sensitive technique) and will further lower the I_p. Numerous attempts have been made to quantify dispersion using XPS with focus on the shape of the modelled particle. One model by Kuipers shows that

I$_p$/I$_s$ can be used as a direct measure of dispersion, independent of particle shape.[14]

Experimental

X-ray photoelectron spectroscopy was carried out using a Thermo Fisher Scientific K-alpha+ spectrometer. A monochromatic Al Kα X-ray source was used to analyse the samples over an area of 600x400 microns. Data was recorded at energies of 150 eV for survey scans and 40eV for high resolution scans with a step size of 0.1 eV. The neutralisation of charge was achieved through low energy electrons and argon ions.

2.3.5 Fourier Transform Infrared Spectroscopy (FT-IR)

Infrared spectroscopy is one of the most versatile analysis techniques in chemistry. It can be used to analyse solids, liquids and gases, can be used quantitatively or qualitatively, and offers a vast amount of information whilst being a cheap and fast technique.

Electromagnetic radiation in the infrared region (2.5-25 μm) is absorbed by covalent bonds in molecules and causes them to vibrate or bend. Different bonds (and different vibrational modes of these bonds) absorb energy at characteristic wavenumbers, therefore, by measuring at which wavenumbers the radiation is absorbed it is possible to identify the bonds present in a molecule. For a linear molecule with N atoms, there exists $3N - 6$ vibrational modes and for non-linear molecules there exists $3N - 5$ vibrational modes, an example of these for a non-linear molecule with 3 atoms is shown in Table 1. In order for a molecule to be IR active there must be a change in dipole moment (however, this doesn't mean there has to be a permanent dipole). For this reason, some diatomic molecules are inactive as they only have one bond and one vibrational mode. Symmetrical diatomic molecules (e.g. N_2 or O_2) are not IR active as they will not present a change in dipole moment, however, asymmetric diatomic molecules (e.g. CO) are IR active.

Symmetric Stretch	Asymmetric Stretch	Scissoring
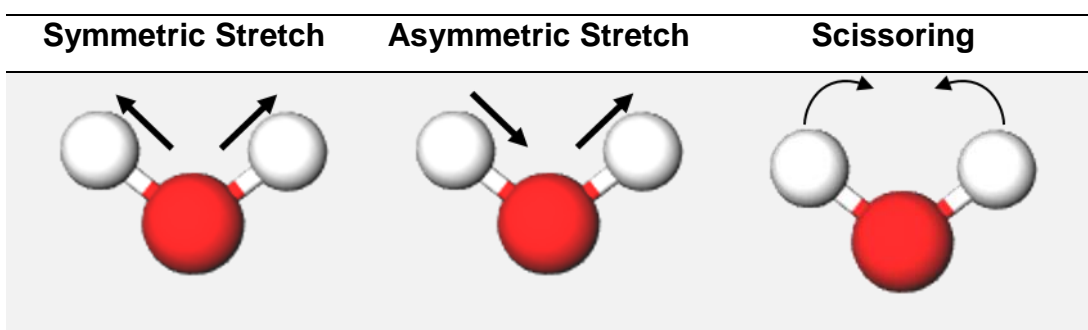
Earlier spectrometers (along with cheaper current spectrometers) use a monochromatic light source that scans through the desired spectral region (typically 4000 – 400 cm^{-1}), however, this is a slow method of analysis. Fourier-transform IR spectroscopy is a more advanced form or IR spectroscopy that uses a polychromatic light source and an interferometer to measure multiple wavenumbers at the same time. The main benefit of this method is Felgett's Advantage, simply that by taking multiplex readings (in this case multiple wavelengths of light at once as opposed to scanning through single wavelengths) an increase in signal-to-noise ratio as well as a reduction in sampling time is achieved.

Experimental

In this work a Gasmet FT-IR equipped with a 0.4 L sample cell was used to analyse the effluent gas from the ammonia decomposition reaction. As discussed in the previous paragraphs, N_2 and H_2 are not IR active as they are symmetrical diatomic molecules. NH_3 is the IR active component of the reaction that was followed, with its concentration being calculated by the Calcmet software with reference files from 50-5100 ppm NH_3. This equipment and software is shown in Figure 10.

2.3.5.1 Diffuse Reflectance FT-IR (DRIFTS)

Diffuse reflectance FT-IR, commonly known as DRIFTS, is a technique for analysing the surface of a solid sample. IR light is reflected off the surface of a powder, however, because the powder is an example of a rough surface the light is reflected at many angles, this is called diffuse reflectance. The

powdered sample is placed in a sample cup and mounted in a DRIFTS cell. The cell consists of a number of mirrors directing the beam to a mirror that focuses the beam onto the sample. A large, ellipsoid focussing mirror is then used to collect the reflected beam and another series of mirrors then direct this beam to the IR detector. Focussing of the beam and collection of diffuse reflectance radiation is shown in a simplified schematic in Figure 6, the interferometer is not shown. Due to the use of multiple mirrors, as well as the large scattering due to diffuse reflectance, very little of the incident beam makes it to the detector and the IR efficiency is low.
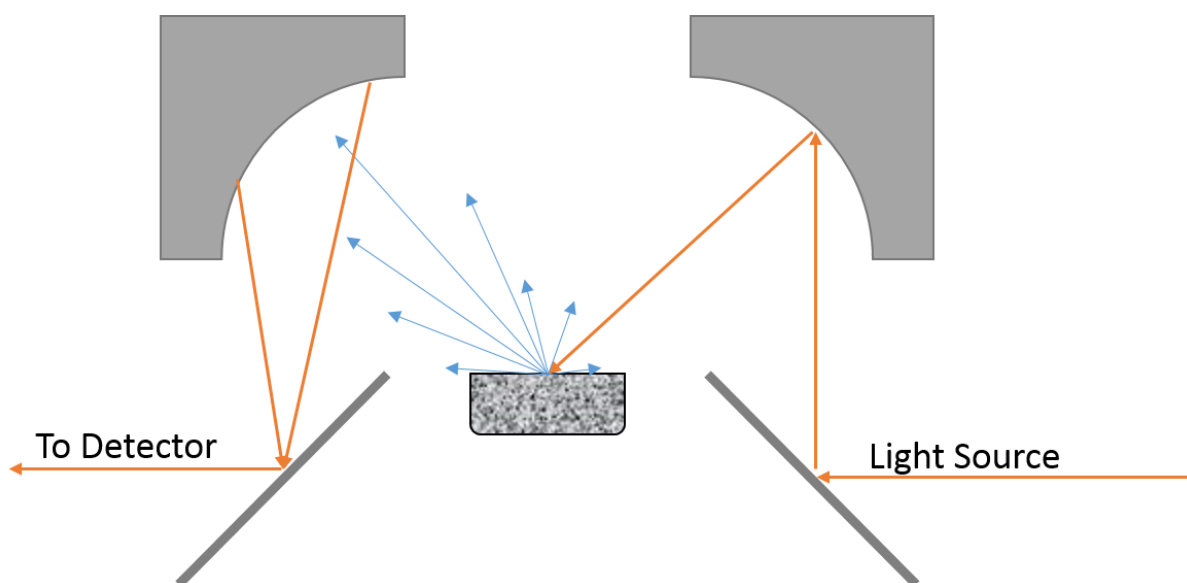
Figure 6: Schematic of a DRIFTS cell. The beam is focussed on the sample from the light source (orange), reflects diffusely from the sample (blue) and is then refocussed and guided to the detector (orange)

It is important to discuss two aspects of DRIFTS. Firstly, DRIFTS is sensitive to sample preparation and great care must be taken when preparing samples to get results that can be compared to each other. Samples should be well ground before use, typically in an agate pestle and mortar, to ensure uniform particle shape and size throughout the sample. A uniform particle shape and size is desirable as it reduces light scattering and leads to an increased intensity of measured light, which as discussed above is a desirable thing. Care must also be taken when filling the sample cup as multiple factors such as packing density and the size of particles on the surface (a problem somewhat alleviated by grinding) will lead to differing intensities of reflected light and different band heights.

Secondly, is the issue of y-axis units. Usually IR spectra are plotted in absorbance or transmittance, however, since DRIFTS is a reflectance technique these are both incorrect. The units commonly used for the y-axis are Kubelka-Munk units, named after the two scientists whose equation relates intensity of diffusely reflected light and concentration. It is also possible to use these units for quantitative DRIFTS if suitable calibration spectra are taken.

Experimental

DRIFTS studies were carried out on a Bruker Tensor 27 spectrometer using a Harrick in-situ cell equipped with 2mm CaF_2 windows. The cell was connected to a water chiller, Harrick cell heater and thermocouple to regulate heat, and Swagelok lines to allow gas flow through the cell. 20 ml/min 10%CO/N_2 was passed over the catalyst for 30 mins to saturate it with CO. The flow was then switched to pure N_2 for a further 30 mins to remove physisorbed CO and leave only the chemisorbed species.

2.3.6 Temperature Programmed Reduction (TPR)

Temperature programmed reduction (TPR) is characterisation technique that can be used to gather information on oxidation states present in a catalyst, reduction temperatures for metal species on the catalyst, reduction phenomena occurring during the heat treatment and interactions occurring within the catalyst such as strong metal-support interactions (SMSI).

A small sample of catalyst is packed in a reaction tube and a dilute H_2/Ar gas mix is passed through the catalyst bed while the temperature is increased at a uniform rate. The effluent gas is passed through a thermal conductivity detector to measure the uptake (or in a few instances, evolution) of hydrogen. This produces a signal vs. temperature plot showing peaks at the temperatures of different reduction processes. An example TPR plot for CuO is shown in Figure 7. Reduction temperatures can be characteristic of different metal oxidation states and species and can be assigned from literature. However, as support materials, promotors and impurities can all shift the position of reduction peaks, it should not be used primarily for identification of oxidation states, this would be much better suited to techniques such as XPS.
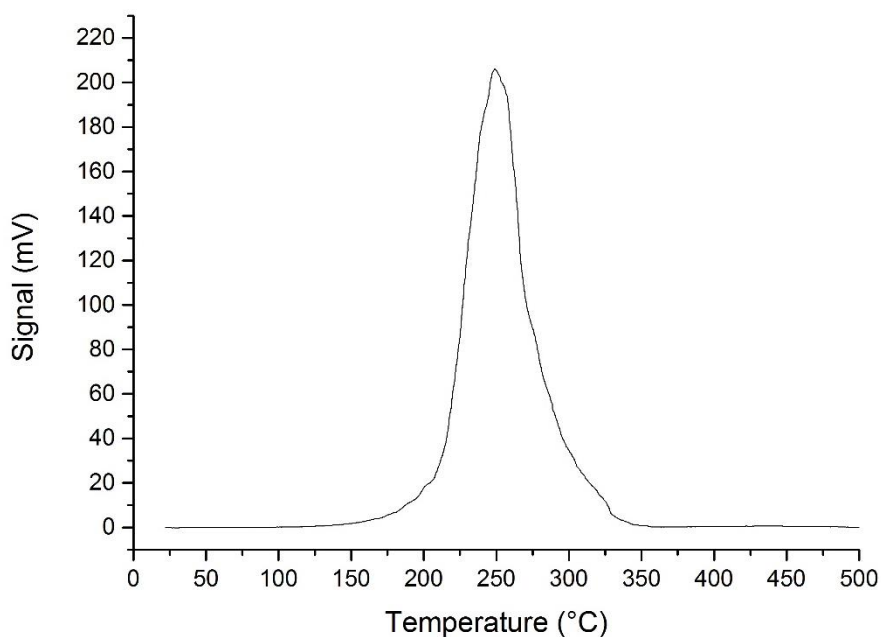
Figure 7: H$_2$ - TPR of CuO

CuO has one distinct reduction event at ~270 °C in which the entire sample is reduced and therefore can be used as a calibration standard to make TPR a quantitative technique. By reducing different masses of CuO and calculating the mols of H$_2$ needed to fully reduce each sample, a calibration plot can be produced relating integrated peak area and H$_2$ uptake. This is shown in Figure 8, the calibration used in this work. Applying this to TPR characterisation of catalysts is then straightforward: reduction peaks are integrated and then converted into the number mols H$_2$ consumed by the reduction. Knowing the metal species being reduced, and therefore the stoichiometry of reduction, the total mols metal reduced can be calculated. This is useful in that it gives information on the degree of reduction of a sample and the relative ratios of metal species present in a sample.
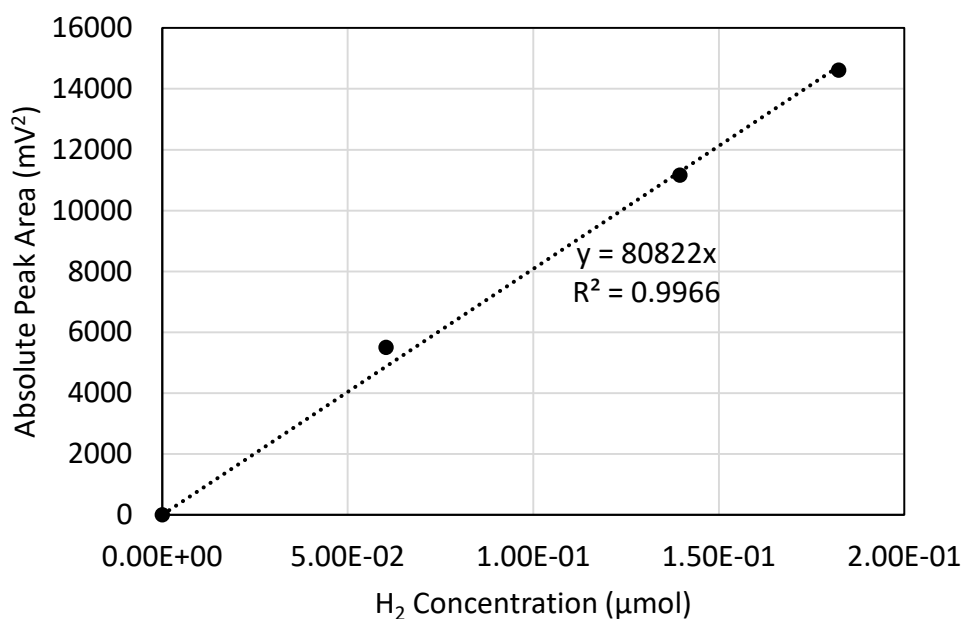
Figure 8: TPR calibration of ChemBET Pulsar instrument using CuO

Experimental

Temperature programmed reduction (TPR) was performed using a Quantachrome ChemBET Pulsar and the associated TPRWin software. Heating rates and ranges and the pre-treatment step varied depending on catalyst sample, but a typical procedure is as follows. ~50 mg catalyst was fixed between two quartz wool plugs in the analysis tube and was pretreated at 160 °C (20 °C/min heating rate) for 60 minutes under an Ar flow. Reduction was then carried out using 10% H_2/Ar from room temperature to 800 °C with a heating rate of 5 °C/min.

2.3.7 Gas Adsorption Techniques

Gas adsorption is a versatile technique used to characterise numerous properties of both support and active site including surface area, porosity and acid/base sites. Adsorption techniques probe the interaction between a gas (the adsorptive) and a surface (the adsorbent) when the gas is in an adsorbed state on the surface (the adsorbate). Adsorption occurs in two manners, chemical adsorption (chemisorption) or physical adsorption (physisorption), which differ by their heats of adsorption and reversibility and can be used to

probe different properties of catalysts. Physisorption is used to measure pore size and distribution of support materials, whereas chemisorption is used to selectively measure the surface area of active sites or probe specific sites support features such as acid/base sites.

2.3.7.1 Physisorption, Specific Surface Area and BET Theory

Physisorption is the reversible adsorption of a gas onto a surface and occurs at any gas/surface interface. The interactions between adsorptive and adsorbent are weak and namely van der Waals interactions, leading to low heats of adsorption and no changes to structure. Multiple layers can be adsorbed forming a multilayer. Physisorption is used experimentally to determine catalyst properties such as specific surface area, porosity and pore size distribution. This is done by dosing the sample with a gas (typically N_2) at a suitably low temperature (typically the boiling point of the probe gas, 77K for N_2) at a series of pressures. The volume of gas is then plotted as a function of changing pressure to create an isotherm with different pore structures leading to different isotherms. The most relevant isotherm for this project, type II, is shown in Figure 9.
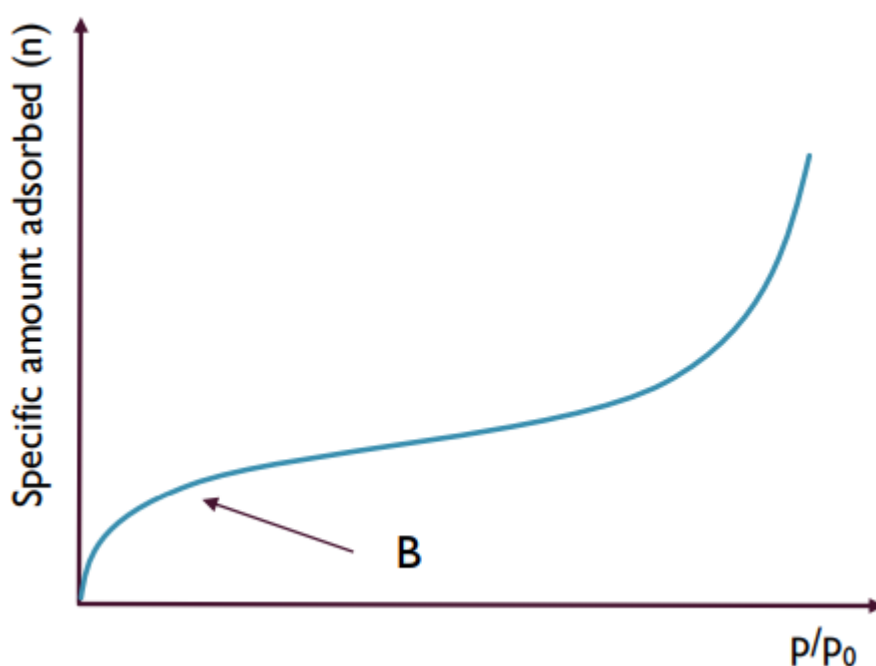
Figure 9: Type II adsorption isotherm

Up until point B shows the formation of a monolayer of adsorbate, increasing pressure after this point shows the formation of multilayers. From this isotherm the surface area can be calculated using Brunnaer, Emmett and Teller (BET) theory. Unlike previous models, BET theory recognises the formation of multilayers and can be used to calculate the number of atoms required to form a monolayer. The BET equation is shown in Equation 7

Equation 7: BET equation

$$\frac{P}{V(P_0 - P)} = \frac{1}{V_m.C} + \frac{(C-1)}{V_m.C} \cdot \frac{P}{P_0}$$

Where:

P is the equilibrium pressure

P_0 is the saturation pressure

V is the volume adsorbed

V_m is the monolayer volume

C is a constant

A linear region of the isotherm is required for analysis using the BET equation, for this reason adsorption is usually measured at 5 points from P/P_0 = 0.05-0.35. A plot of $\frac{P}{V(P_0-P)}$ against $\frac{P}{P_0}$ will give a straight line with an intercept of $\frac{1}{V_m.C}$ and gradient of $\frac{(C-1)}{V_m.C}$. Then, using the calculated value of V_m, surface area can be calculated using Equation 8.

Equation 8: Surface area calculation

$$S = \frac{V_m}{22414} \cdot N_A \sigma$$

Where:

S is the surface area

N_A is Avogadro's constant

σ is the cross-sectional area of N_2 (0.162 nm^2)

It is standard practise to turn this surface area (m^2) into a specific surface area (m^2/g) by dividing by the sample mass for comparison between samples.

Experimental

Specific surface area measurements were carried out using a Quantachrome Quadrabsorb. A mass of sample equivalent to ~10 m^2 was degassed for 16 hours at 250 °C before N_2 physisorption was performed at 77 K. Specific surface area was calculated using BET theory with 5 points in the linear region 0.05-0.35 p/p_0.

2.4 Catalyst Testing

2.4.1 Ammonia Decomposition

Ammonia decomposition testing was carried out in a fixed-bed flow reactor, a schematic is given in Figure 10. The catalyst (0.1 g) was fixed in a quartz tube (7 mm i.d.) between two pieces of quartz wool. The catalyst bed was heated to 500 °C under a flow of Ar for 1 h. The reaction gas, 5000 ppm NH_3/Ar was then allowed to stabilise bypassing the catalyst bed for 30 mins. The reaction gas was then passed over the catalyst bed. On-line analysis of the effluent gas stream was carried out by FT-IR and the conversion was calculated after steady-state was achieved, typically 2 h.

For catalyst stability tests the above method was used, however, the reaction gas was passed over the catalyst bed for 20 h.

Initially, the catalyst bed was fixed in a stainless steel tube (10 mm i.d.). Contamination of the reaction tube is discussed in 4.2.1 and lead to the change to quartz tubes.
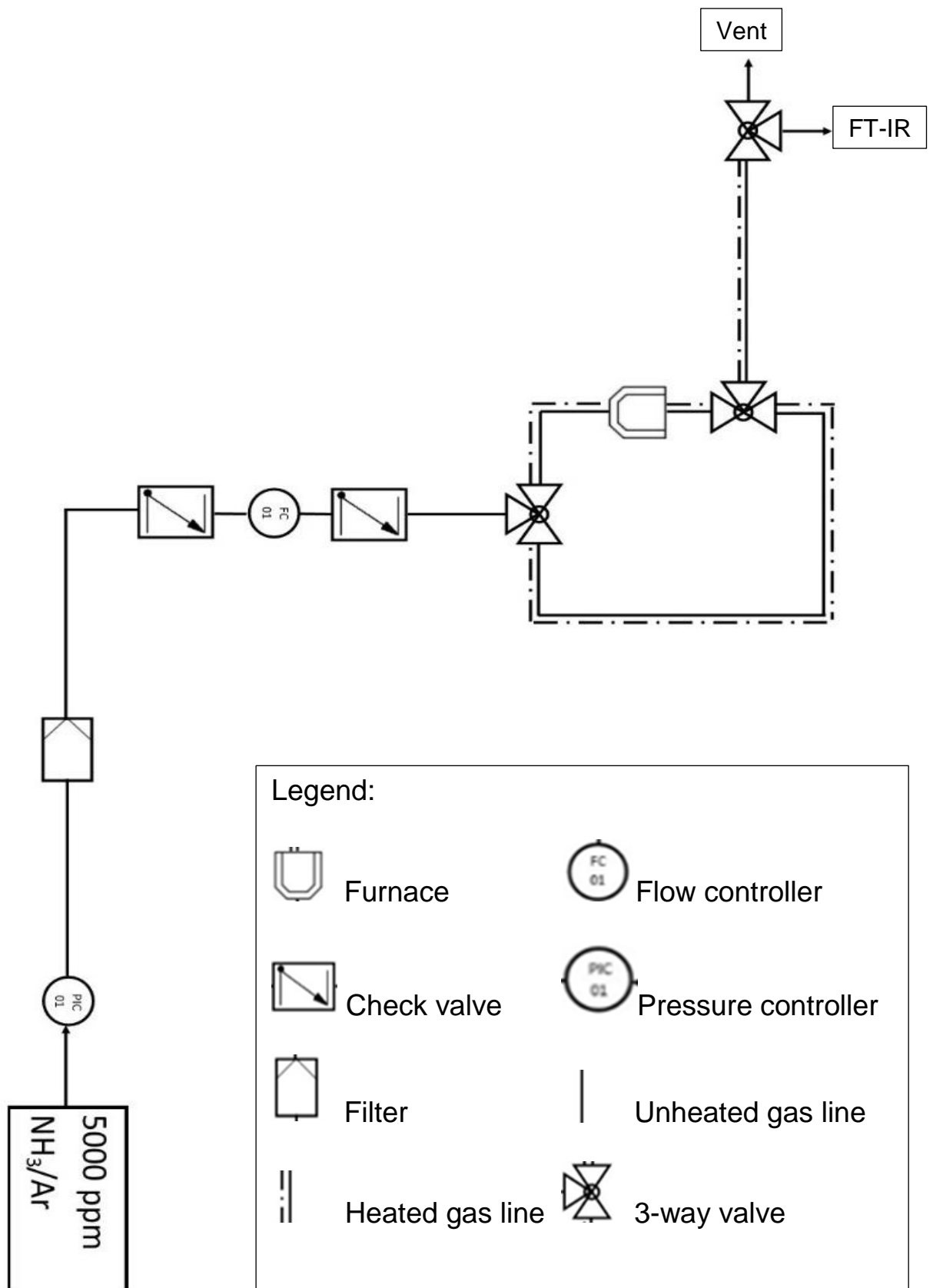
Figure 10: Schematic of ammonia decomposition testing reactor

Legend:

Furnace		Flow controller	FC 01
Check valve		Pressure controller	PIC 01
Filter		Unheated gas line	
Heated gas line		3-way valve	

Vent

FT-IR

FC 01

PIC 01

5000 ppm NH₃/Ar

2.5 References

1   J. Grunwaldt, C. Kiener and W. Clemens, *J. Catal.*, 1999, **181**, 223–232.

2   Y. Joseph, G. Ketteler, C. Kuhrs, W. Ranke, W. Weiss and R. Schlögl, *Phys. Chem. Chem. Phys.*, 2001, **3**, 4141–4153.

3   M. M. Forde, Cardiff University, 2011.

4   M. M. Forde, R. D. Armstrong, C. Hammond, Q. He, R. L. Jenkins, S. A. Kondrat, N. Dimitratos, J. A. Lopez-Sanchez, S. H. Taylor, D. Willock, C. J. Kiely and G. J. Hutchings, *J. Am. Chem. Soc.*, 2013, **135**, 11087–11099.

5   H. Bahruji, M. Bowker, W. Jones, J. Hayward, J. Ruiz Esquius, D. J. Morgan and G. J. Hutchings, *Faraday Discuss.*, 2017, **197**, 309–324.

6   M. Behrens, F. Studt, I. Kasatkin, S. Kuhl, M. Havecker, F. Abild-Pedersen, S. Zander, F. Girgsdies, P. Kurr, B.-L. Kniep, M. Tovar, R. W. Fischer, J. K. Norskov and R. Schlogl, *Science (80-.).*, 2012, **336**, 893–897.

7   R. F. Egerton, P. Li and M. Malac, *Micron*, 2004, **35**, 399–409.

8   D. E. D. E. Berl, *Clay Clay Miner.*, 2001, **49**, 514–528.

9   H. Frauenfelder, G. A. Petsko and D. Tsernoglou, *Nature*, 1979, **280**, 558–563.

10   K. O'Connell and J. R. Regalbuto, *Catal. Letters*, 2015, **145**, 777–783.

11   R. D. Feltham and P. Brant, *J. Am. Chem. Soc.*, 1982, **104**, 641–645.

12   J. W. Niemantsverdriet, *Photoemission and Auger Spectroscopy*, 2007.

13   D. Yang and E. Sacher, *Appl. Surf. Sci.*, 2002, **195**, 187–195.

14   C. E. Kuipers, H. C. E. Van Leuven and W. M. Visser, *Surf. Interface Anal.*, 1986, **8**, 235–242.

3 Preparation Techniques for State-of-the-Art Active Phases

3.1 Introduction and Aims

3.1.1 Ru as an Active Nanoparticle

As discussed in 1.4, Ru is the most investigated transition metal catalyst for ammonia decomposition. It has been shown to be the most active monometallic catalyst[1–3] and has been studied on many supports.[4–6] Its activity can be improved by support modification, where desirable support properties such as conductivity and basicity are enhanced,[7–9] and the use of alkali metals as promotors.[10,11] As of 2017, the most active catalysts consist of Ru supported on a conductive carbon support (such as MWCNTs) with a Cs promotor.[9]

This high activity that is unparalleled throughout the transition metals has been attributed to the optimal N-binding energy calculated for Ru, a useful descriptor for the reaction.[12] As detailed in Chapter 1, the rate-determining step (RDS) is dependent on the interaction between the metal surface and the N of the NH_3 and the effect this has on N-H bond scission energy. In the case of Ru, this interaction is strong enough to facilitate N-H bond cleavage, but not so strong that N_2 associative desorption is hindered.[3] It is widely accepted that N_2 associative desorption is the RDS.

It has been widely reported that the active site on Ru catalysts is the B_5-site, as illustrated in Figure 20. This is a Ru atom with five neighbouring Ru atoms, specifically three in one layer with two in the layer above forming a step.[13–15] This active site is maximised when Ru nanoparticles are between 3-5 nm,[15,16] therefore catalysts with nanoparticles of this size are desirable. It has also been reported that electron-withdrawing groups including Cl^- inhibit the

ammonia decomposition reaction. Therefore, to maximise activity the use of Cl⁻ in the catalyst preparation should be avoided.[7,17]
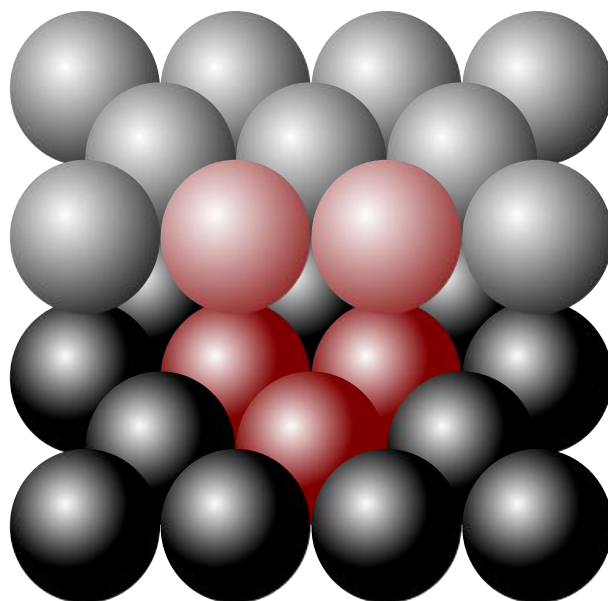
Figure 20: Illustration of a B₅-type site with the relevant atoms highlighted in red

In this chapter, supported Ru catalysts were investigated to validate the testing reactor built for this project and to investigate a novel preparation method for supported Ru catalysts – Chemical Vapour Impregnation (CVI). CVI is known to produce catalysts with small, metal nanoparticles which are well-dispersed on the support, with more control than conventional impregnation techniques.[18] It has been shown that there is an optimum particle size of 3 nm for Ru catalysts[11] and it is expected that CVI will be appropriate for preparing this. CVI also uses organometallic precursors and therefore no inhibitory Cl⁻ will be introduced. A series of simple, commercially desirable supports was screened and the most active was taken forward to investigate with CVI.

3.1.2 CoMo as an Active Mixed Metal Phase

CoMo was first predicted to be active for ammonia synthesis by Norskov and co-workers in 2001.[19] Using N-binding energy as a descriptor for the reaction, a volcano-style relationship was observed with activity. This showed metals with too-strong or too-weak binding energy exhibiting lower activity with an

intermediate binding energy offering an optimum activity. Of the transition metals tested, Ru was the closest to the optimum and exhibited the highest activity. However, it was hypothesised and demonstrated that by combining a metal from each side of the volcano plot, a material of intermediate binding energy and increased activity could be produced. CoMo catalysts were then demonstrated to be active for the decomposition reaction by other groups.[20,21]

Many of these CoMo-based catalysts are active as CoMoN which is formed through the nitridation of $CoMoO_4$ catalyst precursors. These catalyst precursors are often prepared by co-precipitation,[22,23] however, the pH of this step is left uncontrolled. The precipitation pH will be investigated to elucidate its effect on the morphology of CoMo oxide catalyst precursors and their subsequent activity for ammonia decomposition. These precursors will be activated *in-situ* using NH_3 to form an active species to then decompose NH_3. *Ex-situ* activation, in which the higher temperatures common in previous research can be used and will be compared to previously reported catalysts.

3.1.3 Aims

This initial research is to form a foundation on which the novel research of the proceeding two chapters can build. The supported Ru catalysts will serve to validate a suitable testing reactor and inform future choice of support material and preparation technique. Although the most active reported catalysts frequently use carbon nanotubes, these are expensive and impractical on a commercial scale. Therefore, only cheap and readily available supports such as metal oxides and activated carbon will be investigated. The CoMo catalysts will be used as an insight into the design of novel bimetallic catalysts using computational techniques and how synergistic relationships between two transition metals can occur. This initial research will also investigate the effect of catalyst preparation parameters on the activity of state-of-the-art catalyst.

3.2 Novel Preparation of Supported Ru Cataylsts Using CVI

3.2.1 Preparation of Metal Oxide Supported Ru using Standard Impregnation

3.2.1.1 Calcination vs. Reduction

Initial investigations were carried out using a commercial 5%Ru/C catalyst (Sigma-Aldrich) and investigated the effect of a reduction pre-treatment on catalyst activity. As shown in Figure 2, both untreated and reduced forms of the commercial catalyst are active for ammonia decomposition and reach equilibrium conversion at 475 and 450 °C, respectively. Reduction of the Ru/C catalyst increases activity, lowering the T_{50} by 25 °C. Yin *et al.* ascribe this increase in activity to the removal of poisonous Cl$^-$ ions on the catalyst,[7,17] however, due to the unknown preparation of the commercial catalyst it is unknown if Cl$^-$ ions are present in the untreated sample. The effect of Cl$^-$ ions on activity is investigated later in this chapter.
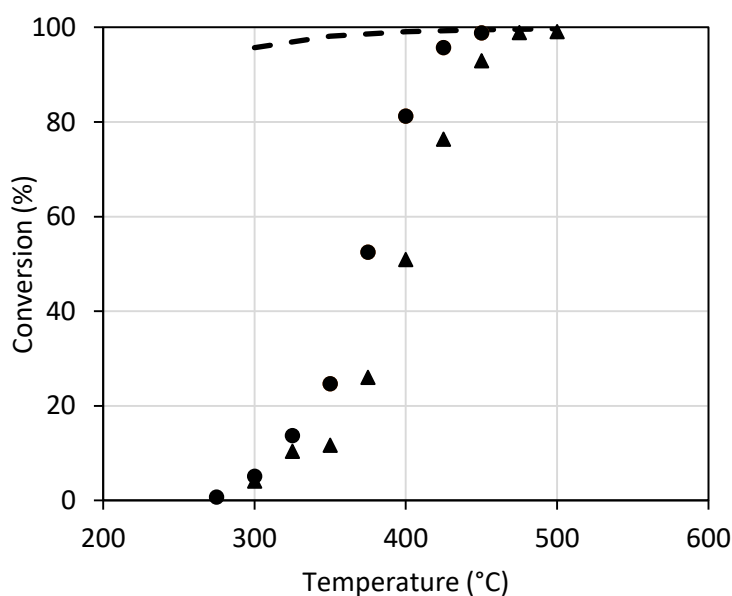
Figure 2: Ammonia decomposition activity of untreated (▲) and reduced (●) commercial 5% Ru/C. The dotted line represents equilibrium conversion as discussed in the introduction

By plotting 1/T against ln(activity) an Arrhenius plot was obtained for both reactions and is shown in Figure 3. The slope of this graph is $-E_a/R$ and was used to calculate the apparent activation energy. For this, only conversions of <50% were used to be sure that the reaction was not mass-transfer limited. The apparent activation energy decreases from 103 to 86 kJ/mol due to the reduction heat-treatment. These values are in good agreement with other reported apparent activation energies and confirm that the testing reactor is suitable for this project.[24] It has also been reported by Perego and Peratello that in a gas-solid fixed-bed reactor (such as this), mass transfer limitations are suspected if the apparent activation energy is <20 kJ/mol.[25] With this 'rule of thumb' it is evident that the reaction conditions used in this work lead to a kinetically-limited regime which is essential for catalytic performance comparison.
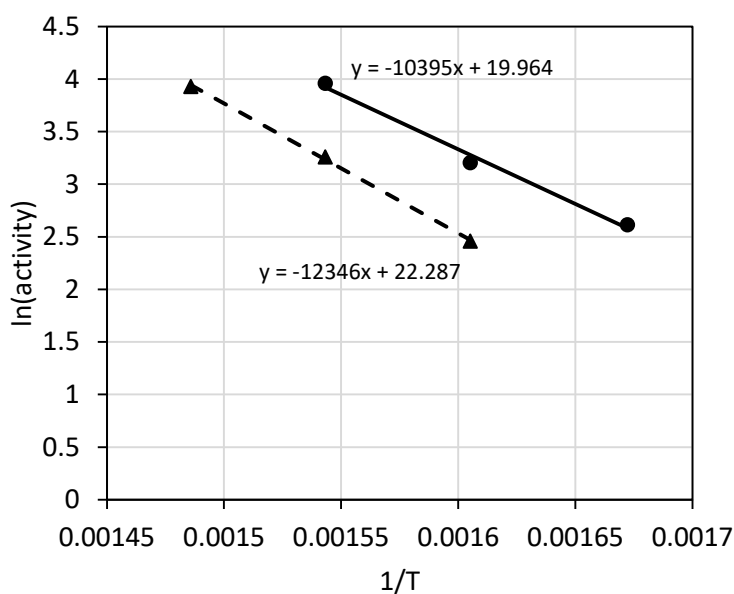
Figure 3: Calculation of E_a for untreated and reduced 5% Ru/C

3.2.1.2   Investigation of Support Materials

Further investigation of supported Ru catalysts was carried out by investigating the effect of the support material. State-of-the-art supports such as CNTs are expensive and require complex synthesis methods. For this project, the focus was on simple materials and preparation techniques, therefore, three common metal oxide support materials were chosen and compared to the commercial C supported catalyst: TiO_2, SiO_2 and Al_2O_3 5%Ru/MO catalysts were prepared by impregnation and tested, comparing activity at 400 °C with the results shown in Figure 4.
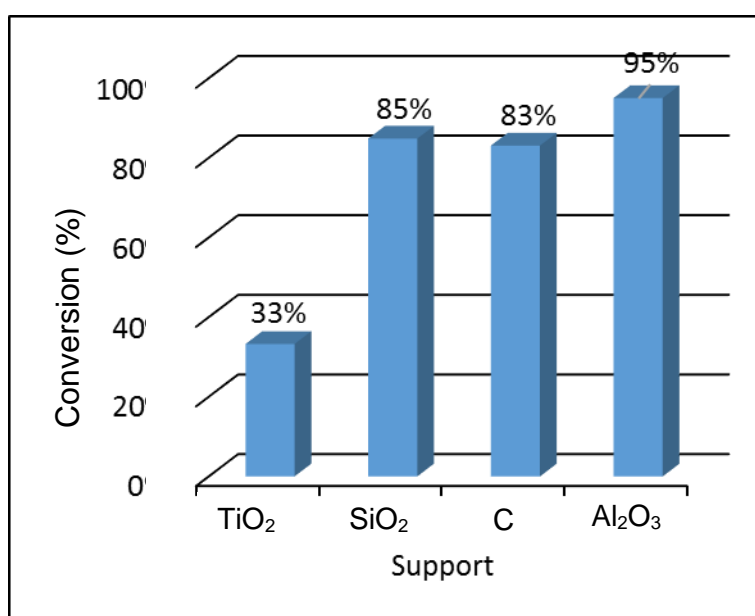
Figure 4: Activity of 5 wt% Ru supported on various support materials prepared by impregnation

These results show that the choice of support has a large effect on the activity of the catalyst, as demonstrated by Yin *et al.*[1] The SiO_2 supported catalyst shows a comparable conversion (ca. 84%) to the C supported catalyst, whereas the activity of the TiO_2 supported catalyst is much lower converting only 33% NH_3. This is in contrast to the work of Yin *et al.* who report TiO_2-supported Ru to have similar activity to the Al_2O_3-supported catalyst.[1] The inactivity of the TiO_2 supported catalyst could be due to the reducibility of the support. Reducible supports exhibit strong metal support interactions whereby the support can grow over the metal nanoparticle during heat-treatment thereby lowering active surface area. The most active catalyst tested was using the Al_2O_3 support, which converted 95% NH_3 at 400 °C. It interesting to

note that there is no correlation between support acidity and activity as discussed in Chapter 1. This investigation has not taken into account alternative structures of these support materials. For example, two common SiO_2 materials have ordered mesoporous structures and these are MCM-41 and SBA-15. A report by Li *et al.* has shown that MCM-41 is more active than non-structured fumed SiO_2.[5] Likewise, the form of carbon used has a large effect on the activity of Ru catalysts as Li *et al.* have shown. They report that graphitic carbon and CNTs are more active than activated carbon,[26] however, as CNTs are expensive and are not commercially viable they were not tested for this project.

With Al_2O_3 identified as the most active support material, the effect of heat-treatment on the catalyst was revisited and investigated further.

3.2.1.3   TPR

Figure 5 shows the TPR of 5%Ru/Al_2O_3 after calcination, after reduction and after testing of the calcined catalyst.
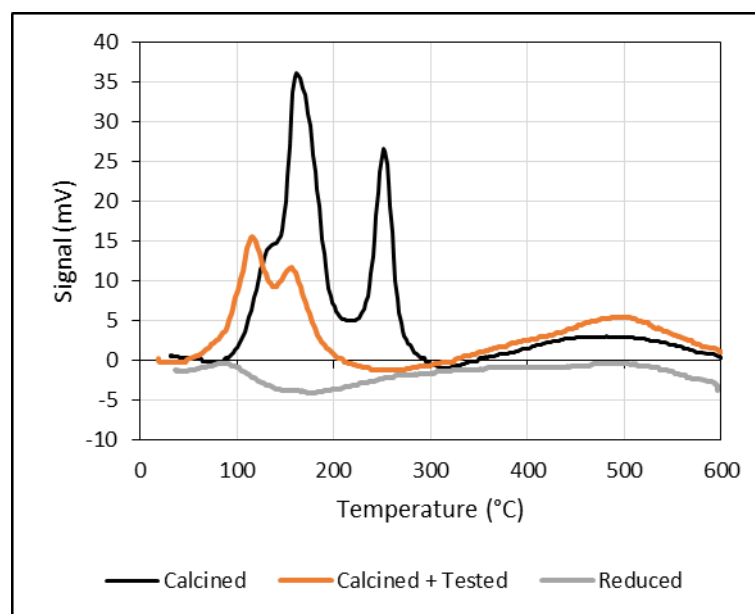

Figure 5: TPR of 5%Ru/Al_2O_3 after: (a) Calcination, (b) Calcination and testing, (c) Reduction

The catalyst shows two main reduction peaks at 160 °C and 250 °C and a shoulder at ~ 110 °C. The reduction at 160 °C is attributed to the reduction of $RuCl_3$[27] and the event at 250 °C is attributed to the reduction of RuO_2 as

reported by Mazzieri *et al.*[28] During ammonia decomposition, H_2 is produced and the catalyst bed is in a reductive environment. In order to see the effect of this reductive environment on the catalyst during testing and therefore gain a more accurate understanding of the active species during the reaction, TPR was performed on a calcined and tested catalyst. There was no reduction of RuO_2 observed at 250 °C and the reduction peak due to $RuCl_3$ at 160 °C was much smaller, showing that during reaction this is not the major Ru species. The main reduction peak in the tested sample is at 110 °C (which was present in the fresh sample as a shoulder of the $RuCl_3$ reduction peak) and is attributed to $RuO_2.xH_2O$.[27] This demonstrates that the reducing atmosphere of the reaction has had an effect on the speciation of Ru and partially reduced the catalyst. The TPR of the reduced catalyst shows no reduction phenomena, indicating that there are no reducible species and the Ru is likely present as Ru^0.

3.2.1.4 XPS

Further investigation into the active Ru species was carried out using XPS and is shown in Figure 6. The Ru 3p region was recorded, as the Ru 3d region strongly overlaps with that of C 1s which, due to adventitious carbon, will always show a signal.[29] The Ru 3p spectrum was investigated in a 2015 paper by D.J. Morgan and the assignments in it are used for analyses of these catalysts.[30] It is seen that the binding energy shifts to a higher energy as the
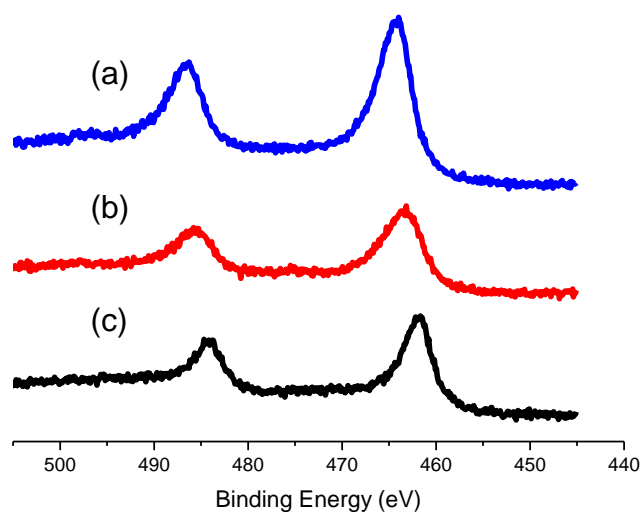

Figure 6: XPS of the Ru3p region in 5%Ru/Al₂O₃ after: (a) Calcination, (b) Calcination and testing, (c) Reduction

sample becomes more oxidised. The Ru 3p binding energy in the calcined catalyst is 464.1 eV which is characteristic of $RuCl_3$. This is in agreement with the TPR in Figure 5 and shows that the calcination pre-treatment does not remove the Cl^- present in the metal salt used in the catalyst preparation. The Ru 3p signal of the calcined and tested catalyst was at 463.4 eV which is characteristic of $RuO_2.xH_2O$ and is again in agreement with the TPR. However, the TPR showed a peak due to $RuCl_3$ reduction that was not observed in the XPS. This could be because it is less abundant than the $RuO_2.xH_2O$ but could also explain why the tested catalyst peak in the spectrum is slightly broader than the other samples. This shows that the catalyst was modified under reaction conditions and the active form of Ru is not that which was put into the reactor. The reduced catalyst showed a peak at 461.7 eV that was characteristic of Ru^0. This corroborates the conclusions made from the TPR due to the absence of reducible Ru species and shows that the most active form of Ru for NH_3 decomposition is Ru^0. This is consistent with the active Ru catalysts previously reported.[1]

3.2.2 Improved Preparation of 5%Ru/Al$_2$O$_3$ using CVI

3.2.2.1 CVI vs. Impregnation

It was shown by Hill *et al.* that there is an optimum Ru particle size of ~3 nm and that the Ru particle size has a large effect on catalyst activity.[11] Therefore, a preparation method which leads to small, uniform nanoparticles with a narrow particle size distribution should produce a more active catalyst than a method with little control over particle size. Chemical vapour impregnation (CVI) has been shown to produce active catalysts using a number of transition metals and is known for producing small nanoparticles of uniform size.[31,32] CVI also has the benefit of using organometallic precursors ($M(acac)_x$), therefore limiting the possible introduction of poisons such as Cl^-.

Figure 7 compares the activity of 5%Ru/Al$_2$O$_3$ prepared by CVI and standard impregnation. It is shown that the catalyst prepared by CVI exhibits higher activity than that of the catalyst prepared by impregnation, with the T$_{50}$ being reduced by ~30 °C. This demonstrates that the novel CVI preparation prepares more active catalysts for NH$_3$ decomposition than conventional impregnation. In order to determine the reason for this enhancement in activity, in-depth characterisation was performed.
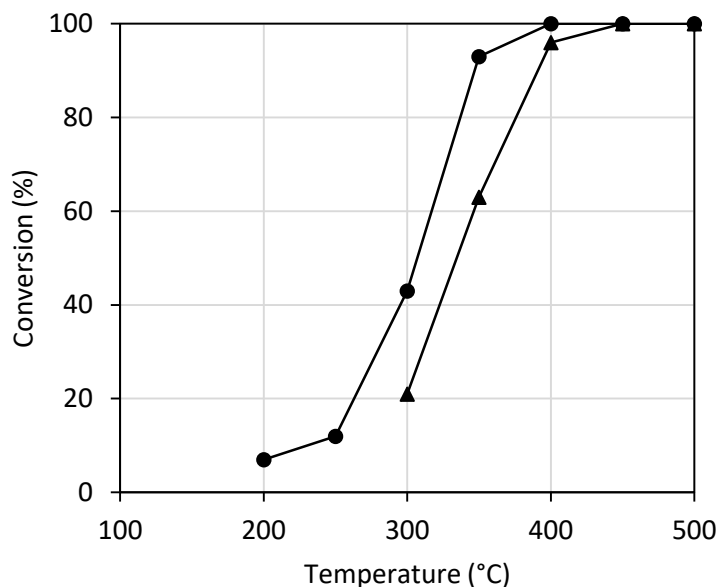
Figure 7: Comparison of ammonia decomposition by 5% Ru/Al$_2$O$_3$
prepared by CVI (●) and impregnation (▲)

3.2.3 Characterisation

3.2.3.1 TEM

In order to investigate the effect of particle size on catalyst activity, TEM was carried out on 5%Ru/Al_2O_3 prepared by both impregnation and CVI and the micrographs are shown in Figure 8.
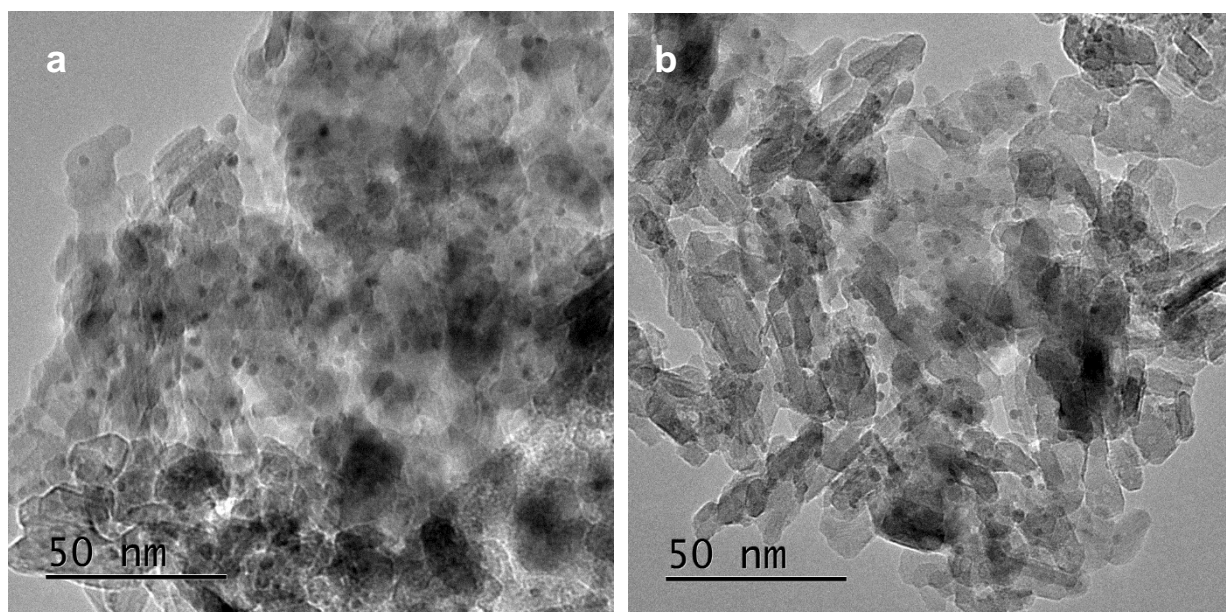
Figure 8: TEM images of 5%Ru/Al_2O_3 prepared by a) CVI, b) Impregnation

In both images, Ru nanoparticles are visible as dark spots of uniform size and well-distributed throughout the sample. An analysis of the mean particle size shows that there is little difference in mean particle size between the samples, with impregnation producing catalysts with particles of 2.47 nm and CVI producing particles of 2.62 nm. Both methods prepare catalysts with a narrow particle size distribution as displayed in Figure 9. All particles observed were between 1.5 and 4.5 nm, with impregnation preparing slightly more nanoparticles below 3 nm and CVI preparing more nanoparticles in the range 3-4.5 nm. The increased number of nanoparticles >3 nm in the catalyst prepared by CVI may be a cause of its higher activity. This also shows that, contrary to what was expected from previous work, CVI does not produce smaller or more well-dispersed nanoparticles than impregnation.
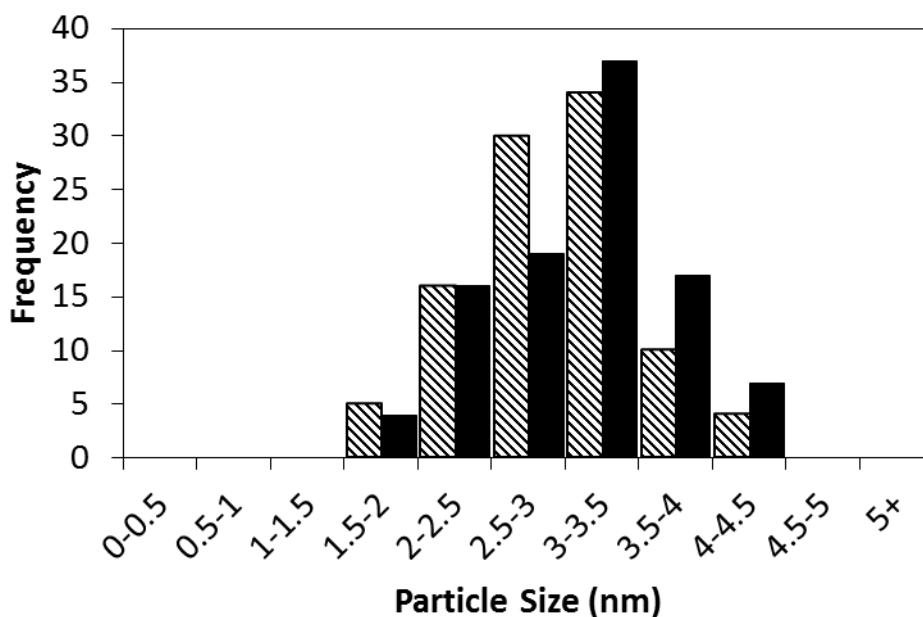
Figure 9: Particle size distribution of 5%Ru/Al₂O₃ as prepared by impregnation (stripes) and CVI (block)

3.2.3.2 BET Surface Area

Catalyst surface area as determined by N_2-physisorption is another common cause for differences in catalyst activity. A higher surface area means more area for reactions to take place and lowers the possibility of sintering as nanoparticles are further apart. Catalyst preparation method can affect the surface area as it can introduce species that will block the pores, interaction with a solvent may alter the structure or if the support is not very thermally stable, heating may cause it to change. The surface area of the Al_2O_3 support and the two Ru/Al_2O_3 catalysts was calculated and is shown in Table 1.

$γ$-Al_2O_3 is a frequently used support and as such has been well-characterised previously. The specific surface area was calculated by the BET method to be 124 m^2/g which is in agreement with previous data.[33] However, it is shown that neither preparation method altered the surface area of the catalyst when loading Ru. As these methods do not produce structural differences, i.e. surface area or particle size, the difference in activity must be due to chemical differences.

Table 1: BET surface area as calculated from N₂-physisorption for Ru/Al₂O₃ catalysts

Sample	Surface Area (m²/g)
Al_2O_3	124

5%Ru/Al₂O₃ Impregnation	124
5%Ru/Al₂O₃ CVI	124

3.2.3.3   XPS

Figure 10 shows the Cl⁻ region of the XPS for both the impregnation and CVI catalysts. It is evident that Cl⁻ is present in both samples, however, there is a much higher concentration in the catalyst prepared by impregnation than that prepared by CVI. Quantification of these regions shows that there is 0.15 at% and 0.55 at% Cl⁻ in the CVI and impregnation samples, respectively. The Cl⁻ present in the impregnation sample is most likely residual Cl⁻ from the $RuCl_3$ precursor, demonstrating that a high temperature reduction (550 °C) is not sufficient to fully remove Cl⁻. The presence of Cl⁻ in the CVI catalyst is unexpected as the precursor is Cl-free and the preparation equipment does not come in contact with Cl-containing compounds. In this case, the Cl⁻ contaminant most likely occurred either in the heat-treatment step, due to the
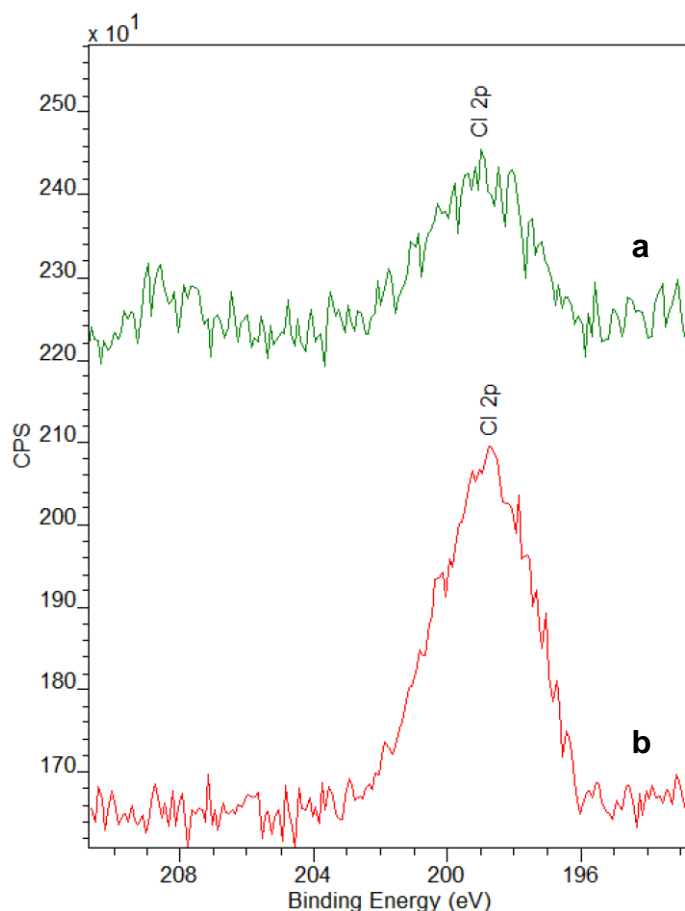
Figure 10: Cl 2p region of the XPS spectrum for 5%Ru/Al2O3 catalysts prepared by (a) CVI and (b) impregnation

use of tube furnaces that have previously been used for Cl⁻ containing catalysts, or present in the Al_2O_3 from its production. Despite this, the increased concentration of Cl⁻ in the impregnation catalyst correlates with the lower activity observed in testing. It has been reported that Cl⁻ is a poison and despite the assumption that a high-temperature reduction removes it this work demonstrates that this is not the case. This highlights the benefits of selecting a Cl-free Ru precursor.[7,17]

The Ru 3p region is shown in Figure 11. The Ru 3p binding energy in both samples is shown to be 462.0 eV which is attributed to metallic Ru. This demonstrates that the state of Ru in both catalysts is the same and therefore the only chemical difference observed using XPS is the presence of the Cl⁻ poison.
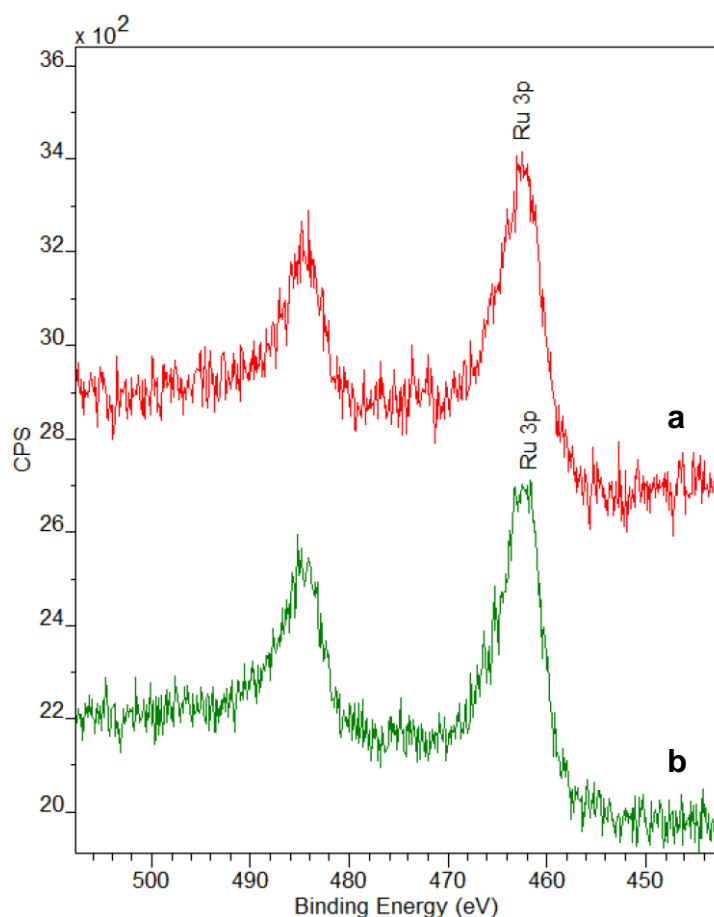
Figure 11: Ru 3p region of the XPS spectrum for 5%Ru/Al₂O₃ catalysts prepared by (a) CVI and (b) impregnation

Mean Ru particle size and BET surface area are some of the most common attributions for differences in activity but despite very different preparation methods these are the same for both catalysts. However, closer analysis of

the particle size distribution reveals that CVI produces more nanoparticles in the 3-5 nm size range which are reported to contain the most active B_5 sites. It was also shown that Cl^-, a known inhibitor of the reaction, is present in much higher quantities in the impregnation prepared catalyst and demonstrates the importance of metal precursor in catalyst preparation. Despite it being reported that high-temperature reduction heat-treatments remove residual Cl^-, low concentrations are shown to remain on the surface and these appear to have a dramatic effect on NH_3 decomposition activity. This novel, solventless preparation is Cl-free and has been demonstrated to produce more active catalysts than conventional impregnation techniques with a more optimal particle size distribution.

3.3 Co-precipitation of CoMo Bimetallic Catalysts

In this section, $CoMoO_4$ was prepared as a catalyst precursor using precipitation techniques with different pH control. Co_3Mo_3N has been reported to be more active for both ammonia synthesis[19] and ammonia decomposition.[34] These catalysts are often prepared by co-precipitation of Co and Mo nitrate precursors, however, the pH during precipitation is uncontrolled.[34,35] The pH of precipitation is reported to have an effect on catalyst morphology,[36] therefore in this study the preparation of the $CoMoO_4$ precursor at controlled pHs was investigated. These precursors were then nitrided *in-situ* using the reaction gas to form the active species. Characterisation of the $CoMoO_4$ precursors was performed to understand the effect of precipitation at different pHs and of the catalysts post-reaction to elucidate the effect of $CoMoO_4$ phase on the active catalyst.

3.3.1 Characterisation of CoMoO₄ Precursors

3.3.1.1   X-Ray Diffraction

XRD analysis was performed on the three $CoMoO_4$ catalyst precursors and is shown in Figure 12. It is immediately evident from the diffraction patterns that the pH of precipitation has a profound effect on the $CoMoO_4$ phase formed. When precipitated at pH 5.5, the $CoMoO_4$ forms a crystalline phase which is not pure. Five of the most intense reflections, labelled ●, occur at 27, 32, 34, 37 and 47 ° and correspond to the (002), (022), (222), (400) and (421) reflections of $CoMoO_4$ respectively. This is in agreement with work by Veerasubramani *et al.*[37] However, not all reflections correspond to $CoMoO_4$. The most intense among these being the reflection at 40 ° which does not correspond to any reported for phases of $CoMoO_4$, CoO or MoO_3. When precipitated at pH 8 the phase is amorphous, with only two, broad diffraction peaks at 34 ° and 60 ° and therefore the material cannot be identified by XRD. When the pH of precipitation is not controlled the same diffraction pattern is observed as for the catalyst precipitated at pH 5.5, suggesting that when the pH is uncontrolled, the precipitation occurs in slightly acidic conditions.

Measurement of the pH of the uncontrolled sample confirms that the precipitation occurs at pH 5.4.
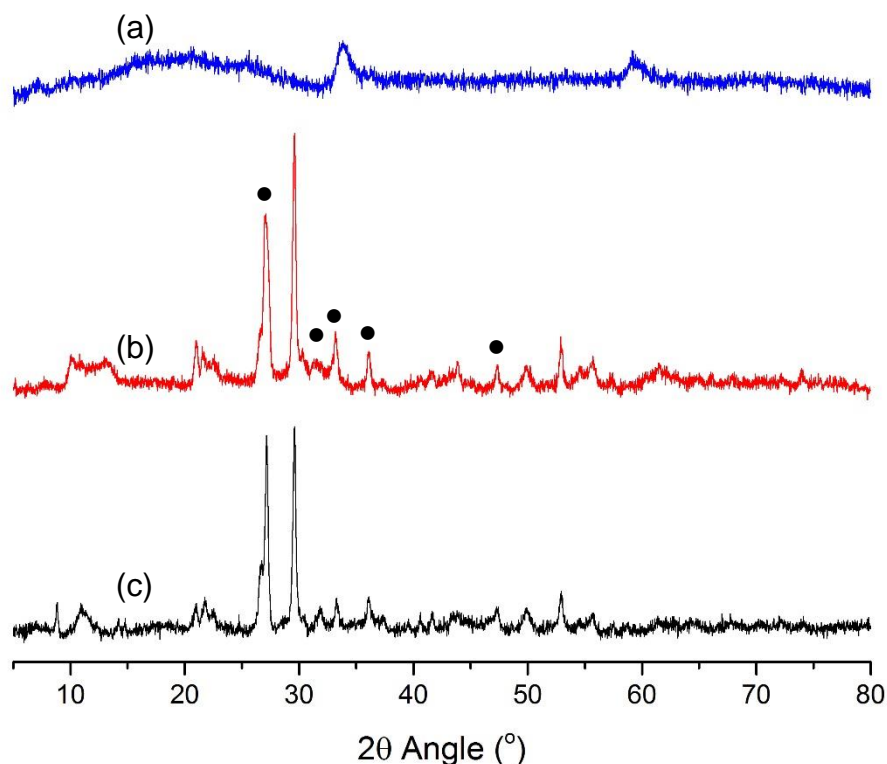
Figure 12: Diffraction patterns of CoMoO₄ prepared with different pH control: (a) uncontrolled pH, (b) pH5.5, (c) pH8

3.3.2 Testing of CoMo Bimetallic Catalysts

The three catalysts were treated *in-situ* in 0.5% NH_3/Ar at 600 °C for 3 hours then tested at 600 °C and in 50 °C intervals down to 300 °C. A fourth catalyst, $CoMoO_x$ prepared with no pH control and treated under the same gas in a tube furnace at 750 °C, was also tested and will be referred to as "No control-TF". This was done to achieve the higher temperatures used by Hargreaves *et al.* and Srifa *et al.*[34,35] The results are shown in Figure 13. The catalysts achieved equilibrium conversion (99.7%) at temperatures above 500 °C and exhibit activity down to 350 °C. All CoMo catalysts were less active than the Ru catalysts tested previously, with the T_{50} of the most active catalyst (CoMoO₄ pH 8) ~120 °C higher than that of the 5%Ru/Al₂O₃ prepared by CVI. The catalysts prepared with no pH control and at pH 8 were not significantly

different, with conversions within ±1% at all temperatures. However, the catalyst prepared at pH 5.5 is significantly lower in activity at 400-500 °C. The reason for this activity difference was investigated by characterisation of the post-reaction catalyst. The $CoMoO_4$ catalyst that was treated at 750 °C is less active again, with a T_{50} ~50 °C higher than the most active CoMo catalysts.
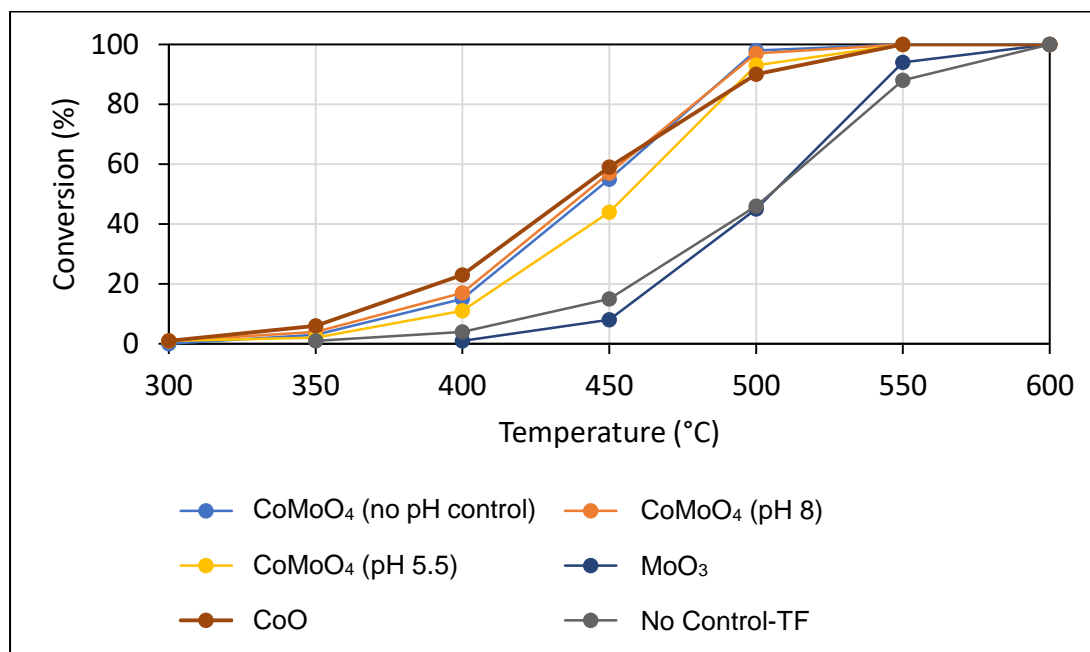
Figure 13: Ammonia decomposition testing of four $CoMoO_4$ catalysts and CoO and MoO_3

Testing of monometallic oxides of CoO and MoO_3 after a similar heat-treatment in NH_3 reveals no synergistic effect, in contrast to previous work that showed that CoMoN was more active than both parent metals.[19] MoO_3 was far less active, not reaching equilibrium conversion until 600 °C and with a T_{50} ~70 °C higher than that of the most active $CoMoO_4$ catalysts. CoO is slightly more active at lower temperatures and slightly less active at higher temperatures than the most active $CoMoO_4$ catalysts but exhibits a similar T_{50}. This is initial evidence that the *in-situ* heat-treatment of these precipitated catalyst precursors did not form an active CoMo nitride catalyst as demonstrated in literature.

3.3.3 Characterisation of Active CoMo Catalysts

3.3.3.1   X-Ray Diffraction

Diffraction patterns of the four CoMo catalysts are shown in Figure 14. It is immediately evident that preparation method and heat treatment alter the structure and composition of the catalyst. The parent metals are not shown. MoO_3 is very crystalline and all peaks match the reference pattern for MoO_2 (ICDD No. 32-0671) and are consistent with the sample reported by Jiang et al.[27] CoO, which after reaction displays three diffraction peaks at 44.2, 51.5 and 75.8 ° which are indicative of the Co(111), Co(200) and Co(220) surfaces of α-Co (ICDD No. 89-4307).[38,39]
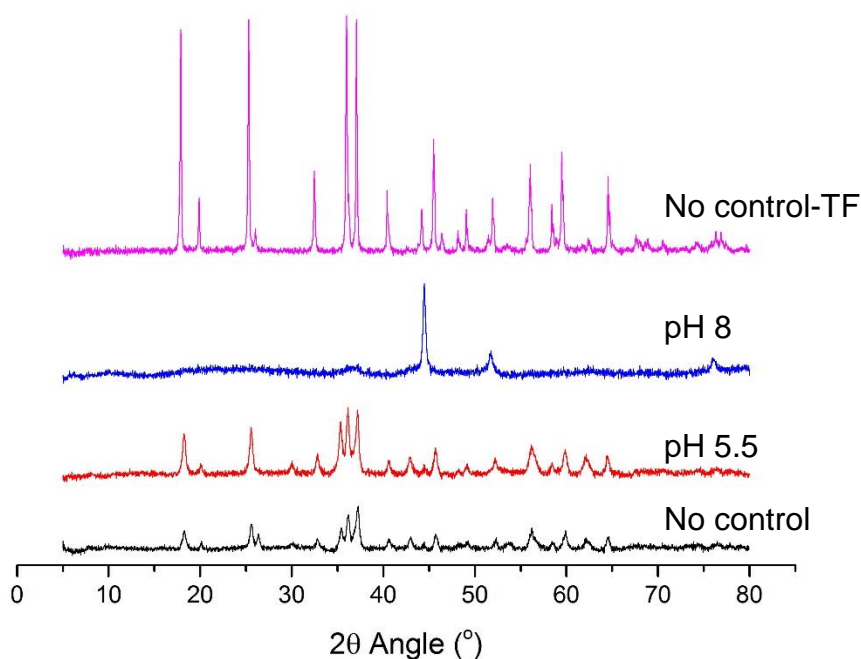
Figure 14: Diffraction patterns of the 4 tested CoMoO$_x$ catalysts

The catalyst preparation at pH 8 shows three reflections at 44.2, 51.5 and 75.8 ° which are all characteristic of Co metal, as previously discussed. This suggests that the Mo is present in an amorphous form and the crystalline, metallic Co has segregated from it, leading to the possibility of supported metallic Co. This catalyst is similar in activity to the monometallic Co catalyst which suggests that the active species in the catalyst may be supported metallic Co, however, there is much less Co present in the CoMo catalyst.

Therefore, if the segregated Co is the active species of the catalyst, its activity has been enhanced either due to smaller nanoparticles or a promotional effect from the CoMo support.

The $CoMoO_4$ sample treated at 750 °C is the most crystalline sample and matches with the reference pattern for $Co_2Mo_3O_8$ (ICDD No. 04-001-9062). It is also consistent with material reported by Adamski et al.[27] This indicates that during the heat-treatment, a partial reduction to the CoMo sub-oxide occurred as opposed to the nitridation shown by Kojima et al. when pure NH_3 was used.[27] There is a small peak that does not match with the reference for $Co_2Mo_3O_8$ at 44.2 °. This is shown to be Co metal, and suggests that there is a minor segregation of Co from the $Co_2Mo_3O_8$ lattice occurring during the heat-treatment. This peak is also present in the work of Adamski et al.[27] Despite this Co peak, the activity for this catalyst is very low. This suggests that either the Co is not the active site of these catalysts or that the amount of Co segregation in this catalyst is a lot less than in the catalysts heat-treated in-situ.

The other two $CoMoO_4$ samples (prepared with no pH control and at pH5.5) show the same phase after heat-treatment/reaction. These peaks match no single phase, however, they do show evidence that these catalysts are in a transitional phase between $CoMoO_4$ and the sub-oxide previously discussed. A majority of the peaks are indicative of $Co_2Mo_3O_8$, with the rest being assigned to various oxides of Mo and Co. Further investigation into the heat-treatment process would be required to elucidate whether higher temperature or longer heating is required to fully form the $Co_2Mo_3O_8$ phase.

In all six catalysts, it was observed that reduction, or partial reduction, occurred whereas there was no evidence of nitridation. As the heat-treatment took place at the same temperature and for a comparable time as previous work, this suggests that ammonia concentration may be important for successful nitridation. Despite this, all catalysts are active for ammonia decomposition. The prominence of metallic cobalt shown in these diffraction patterns and its demonstrated activity as a nanoparticle in the literature[40,41] suggest that cobalt supported on cobalt-molybdenum oxides could be an active catalyst for

ammonia decomposition. However, it is possible that amorphous phases, or highly dispersed species that are below the detection limit of XRD have formed that are also active for the reaction.

3.3.3.2 SEM

SEM was used to investigate the effect of pH during preparation on catalyst morphology. Figure 15 shows images of the three $CoMoO_4$ precursors precipitated at different pH at 200 µm, 20 µm and 1 µm scales. It is evident that the pH of precipitation has a large effect on the morphology of the $CoMoO_4$ precursor prepared. When precipitated with no pH control, the oxide forms a structure of thick sheets with large flat facets randomly oriented. When precipitated in acidic conditions, the morphology formed contains many, far smaller flake-like structures and when precipitated under basic conditions, the structure is very different again, with thin rose petal-like surfaces that appear pristine.
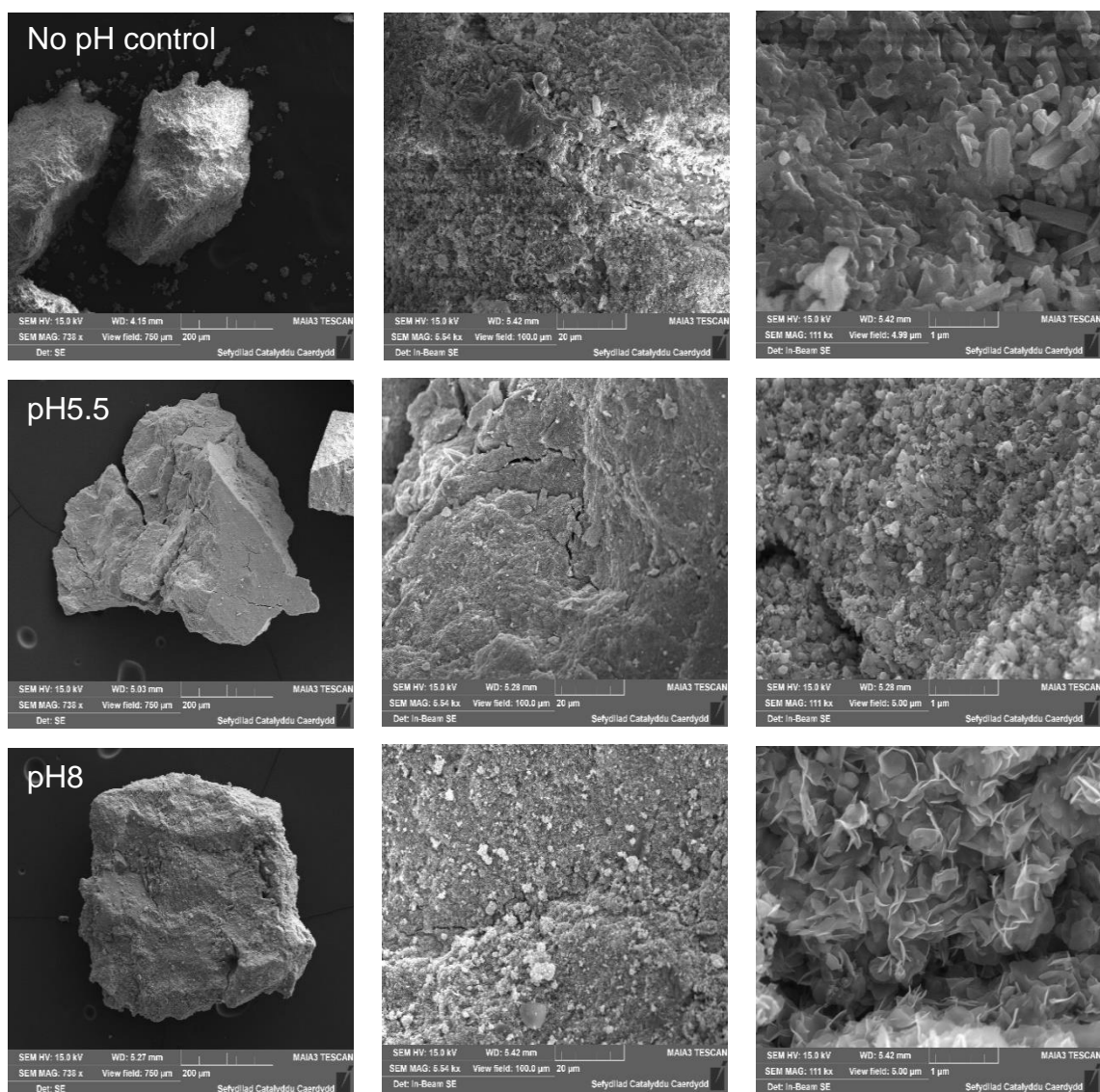
Figure 15: SEM images of CoMoO$_4$ at different magnifications

When related to the XRD and testing results, it can been seen that this morphologies have little effect on activity, with pH 8 and no pH control having very different morphologies and diffraction patterns, yet exhibiting the same activity. This suggests that the activity of the catalyst is not dependent on the morphology.

3.4 Conclusions

Supported Ru nanoparticles were prepared and tested in order to validate the testing reactor to be used throughout this project. Initial tests using a commercial Ru/C catalyst demonstrated the expected high activity and confirmed that the reactor was suitable for the project. It was shown that the apparent activation energy is 17 kJ/mol lower on metallic Ru than on the untreated catalyst, which was similar to other Ru/C catalysts reported previously and suggests that the reaction is not mass-transfer limited. Further investigation into the optimal catalyst preparation showed that $5\%Ru/Al_2O_3$ was more active than the commercial $5\%Ru/C$ catalyst. Characterisation by TPR and XPS showed that a reduction heat-treatment results in a more active catalyst than those that had a calcination heat treatment indicating that the metallic Ru^0 state present in the reduced catalyst is more active than $RuO_2.xH_2O$ and $RuCl_3$ species that are present in the calcined catalyst.

Chemical vapour impregnation was then investigated as a novel, solventless preparation for these state of the art catalysts. Using the knowledge gained from the previous optimisation investigations, Al_2O_3 was used as a support and the catalyst was reduced. It has been shown by TEM and N_2-physisorption that the preparation method has no effect on mean particle size, particle size distribution and BET surface area and the cause of the enhanced activity is a lack of Cl^- on the surface which acts as an inhibitor. This work establishes CVI as a novel method for preparing state-of-the-art catalysts, with a lower Cl^- concentration than traditional impregnation with $RuCl_3$ precursor.

The investigation into effect of precipitation pH on the preparation of CoMo oxides showed that different morphologies can be prepared by varying the pH at which co-precipitation occurs. It was shown that in acidic conditions the prepared $CoMoO_x$ is amorphous whilst under basic conditions the $CoMoO_x$ is crystalline. SEM imaging also showed a great variation in morphology depending on the pH of precipitation, however, despite the differences in morphology and crystallinity two of the catalysts showed the same activity. This suggests that while preparation conditions do have an effect on catalyst morphology, the morphology does not have an effect on catalyst activity. Post-

reaction characterisation showed that the desired Co_3Mo_3N, which has been demonstrated to be more active than Ru, was not formed and instead partially reduced CoMo oxides were formed. XRD indicates that segregated and reduced Co species were observed in all catalysts.

3.5 References

1.   Yin, S.-F. *et al.* Investigation on the catalysis of COx-free hydrogen generation from ammonia. *J. Catal.* **224**, 384–396 (2004).

2.   Yin, S. F., Xu, B. Q., Zhou, X. P. & Au, C. T. A mini-review on ammonia decomposition catalysts for on-site generation of hydrogen for fuel cell applications. *Appl. Catal. A Gen.* **277**, 1–9 (2004).

3.   Ganley, J. C., Thomas, F. S., Seebauer, E. G. & Masel, R. I. A priori catalytic activity correlations: The difficult case of hydrogen production from ammonia. *Catal. Letters* **96**, 117–122 (2004).

4.   Di Carlo, A., Vecchione, L. & Del Prete, Z. Ammonia decomposition over commercial Ru/Al2O3 catalyst: An experimental evaluation at different operative pressures and temperatures. *Int. J. Hydrogen Energy* **39**, 808–814 (2014).

5.   Li, X. K., Ji, W. J., Zhao, J., Wang, S. J. & Au, C. T. Ammonia decomposition over Ru and Ni catalysts supported on fumed SiO 2, MCM-41, and SBA-15. *J. Catal.* **236**, 181–189 (2005).

6.   Lorenzut, B. *et al.* Embedded Ru@ZrO2 Catalysts for H2 Production by Ammonia Decomposition. *ChemCatChem* **2**, 1096–1106 (2010).

7.   Yin, S. F., Xu, B. Q., Wang, S. J. & Au, C. T. Nanosized Ru on high-surface-area superbasic ZrO2-KOH for efficient generation of hydrogen via ammonia decomposition. *Appl. Catal. A Gen.* **301**, 202–210 (2006).

8.   Yin, S. F., Xu, B. Q., Ng, C. F. & Au, C. T. Nano Ru/CNTs: A highly active and stable catalyst for the generation of COx-free hydrogen in ammonia decomposition. *Appl. Catal. B Environ.* **48**, 237–241 (2004).

9.   Hill, A. K. & Torrente-Murciano, L. Low temperature H2 production from ammonia using ruthenium-based catalysts: Synergetic effect of promoter and support. *Appl. Catal. B Environ.* **172**–**173**, 129–135 (2015).

10. Huang, D.-C. *et al.* Preparation of Ru–Cs catalyst and its application on hydrogen production by ammonia decomposition. *Int. J. Hydrogen*

Energy **38**, 3233–3240 (2013).

11. Hill, A. K. & Torrente-Murciano, L. In-situ H2 production via low temperature decomposition of ammonia: Insights into the role of cesium as a promoter. *Int. J. Hydrogen Energy* **39**, 7646–7654 (2014).

12. Hansgen, D. a, Vlachos, D. G. & Chen, J. G. Using first principles to predict bimetallic catalysts for the ammonia decomposition reaction. *Nature chemistry* **2**, 484–489 (2010).

13. Zheng, W., Zhang, J., Xu, H. & Li, W. NH3decomposition kinetics on supported Ru clusters: Morphology and particle size effect. *Catal. Letters* **119**, 311–318 (2007).

14. Karim, A. M. *et al.* Correlating Particle Size and Shape of Supported Ru/γ-Al2O3 Catalysts with NH3 Decomposition Activity. *J. Am. Chem. Soc.* **131**, 12230–12239 (2009).

15. García-García, F. R., Guerrero-Ruiz, A. & Rodríguez-Ramos, I. Role of B5-Type Sites in Ru Catalysts used for the NH 3 Decomposition Reaction. *Top. Catal.* **52**, 758–764 (2009).

16. Torrente-Murciano, L., Hill, A. K. & Bell, T. E. Ammonia decomposition over cobalt/carbon catalysts—Effect of carbon support and electron donating promoter on activity. *Catal. Today* **286**, 131–140 (2017).

17. Wang, S. J. *et al.* Investigation on modification of Ru/CNTs catalyst for the generation of COx-free hydrogen from ammonia. *Appl. Catal. B Environ.* **52**, 287–299 (2004).

18. Bahruji, H. *et al.* PdZn catalysts for CO $_2$ hydrogenation to methanol using chemical vapour impregnation (CVI). *Faraday Discuss.* **197**, 309–324 (2017).

19. Jacobsen, C. J. H. *et al.* Catalyst design by interpolation in the periodic table: Bimetallic ammonia synthesis catalysts [2]. *J. Am. Chem. Soc.* **123**, 8404–8405 (2001).

20. Duan, X., Qian, G., Zhou, X., Chen, D. & Yuan, W. MCM-41 supported CoMo bimetallic catalysts for enhanced hydrogen production by

ammonia decomposition. *Chem. Eng. J.* **207**–**208**, 103–108 (2012).

21. Srifa, A. *et al.* Hydrogen production by ammonia decomposition over Cs-modified Co3Mo3N catalysts. *Appl. Catal. B Environ.* **218**, 1–8 (2017).

22. Podila, S. *et al.* High performance of bulk Mo2N and Co3Mo3N catalysts for hydrogen production from ammonia: Role of citric acid to Mo molar ratio in preparation of high surface area nitride catalysts. *Int. J. Hydrogen Energy* **42**, 8006–8020 (2017).

23. Srifa, A. *et al.* COx-free hydrogen production via ammonia decomposition over molybdenum nitride-based catalysts. *Catal. Sci. Technol.* **6**, 7495–7504 (2016).

24. Choudhary, T. V, Sivadinarayana, C. & Goodman, D. W. Catalytic ammonia decomposition : CO x -free hydrogen production for fuel cell applications. *Catal. Letters* **72**, 197–201 (2001).

25. Perego, C. & Peratello, S. Experimental methods in catalytic kinetics. *Catal. Today* **52**, 133–145 (1999).

26. Li, L., Zhu, Z. H., Yan, Z. F., Lu, G. Q. & Rintoul, L. Catalytic ammonia decomposition over Ru/carbon catalysts: The importance of the structure of carbon support. *Appl. Catal. A Gen.* **320**, 166–172 (2007).

27. Adamski, P. *et al.* Thermal stability of catalyst for ammonia synthesis based on cobalt molybdenum nitrides. **1**, 3

28. Mazzieri, V., Coloma-Pascual, F., González, M., L"argentičre, P. & Fígoli, N. PREPARATION OF Ru/Al2O3 CATALYSTS FROM RuCl3. *React. Kinet. Catal. Lett.* **76**, 53–59 (2002).

29. Barr, T. L., Seal, S., Barr, T. L. & Seal, S. Nature of the use of adventitious carbon as a binding energy standard. *J. Vac. Sci. Technol. A* 1239 (1995). doi:10.1116/1.579868

30. Morgan, D. J. Resolving ruthenium: XPS studies of common ruthenium materials. *Surf. Interface Anal.* **47**, 1072–1079 (2015).

31. Forde, M. M. *et al.* Light alkane oxidation using catalysts prepared by

chemical vapour impregnation: tuning alcohol selectivity through catalyst pre-treatment. *Chem. Sci.* **5**, 3603–3616 (2014).

32. Forde, M. M. *et al.* High Activity Redox Catalysts Synthesized by Chemical Vapor Impregnation. *ACS Nano* **8**, 957–969 (2014).

33. Huang, C. P. & Stumm, W. The specific surface area of γ-Al2O3. *Surf. Sci.* **32**, 287–296 (1972).

34. Hargreaves, J. S. J. & Mckay, D. A comparison of the reactivity of lattice nitrogen in Co3Mo3N and Ni2Mo3N catalysts. *J. Mol. Catal. A Chem.* **305**, 125–129 (2009).

35. Srifa, A. *et al.* COx-free hydrogen production via ammonia decomposition over molybdenum nitride-based catalysts. *Catal. Sci. Technol.* **6**, 7495–7504 (2016).

36. Hessien, M. M., Rashad, M. M. & El-Barawy, K. Controlling the composition and magnetic properties of strontium hexaferrite synthesized by co-precipitation method. *J. Magn. Magn. Mater.* **320**, 336–343 (2008).

37. Rodriguez, J. A., Chaturvedi, S., Hanson, J. C., Albornoz, A. & Brito, J. L. Electronic Properties and Phase Transformations in CoMoO 4 and NiMoO 4 : XANES and Time-Resolved Synchrotron XRD Studies. *J. Phys. Chem. B* **102**, 1347–1355 (1998).

38. Hong, W. *et al.* A novel Co(phen) 2 /C catalyst for the oxygen electrode in rechargeable lithium air batteries. *Chin Sci Bull* **57**, (2012).

39. Yuan, X. *et al.* Effects of cobalt precursor on pyrolyzed carbon-supported cobalt-polypyrrole as electrocatalyst toward oxygen reduction reaction. *Nanoscale Res. Lett.* **8**, 478 (2013).

40. Zhang, J., Comotti, M., Schüth, F., Schlögl, R. & Su, D. S. Commercial Fe- or Co-containing carbon nanotubes as catalysts for NH3 decomposition. *Chem. Commun. (Camb).* 1916–1918 (2007). doi:10.1039/b700969k

41. Podila, S., Alhamed, Y. A., Alzahrani, A. A. & Petrov, L. A. Hydrogen

production by ammonia decomposition using Co catalyst supported on Mg mixed oxide systems. *Int. J. Hydrogen Energy* **40**, (2015).

4 Design and Preparation of Novel Alloy Catalysts for the Ammonia Decomposition Reaction

4.1 Introduction and Aims of the Chapter

4.1.1 Catalyst Design through Periodic Table Interpolation

Numerous alloy catalysts have been investigated as ammonia decomposition catalysts.[1–4] This section will explore the state-of-the-art with respect to the design and use of alloy catalysts and then investigate how this can be applied to novel supported nano-alloy catalysts.

It is widely accepted that N-binding energy is a good descriptor for the reaction, with the activity of transition metals following a volcano-type relationship with binding energy.[5] Of these, Ru is the most active with a binding energy closest to the optimum.[6] This volcano-type relationship arises due to the nature of the decomposition mechanism, with N-H bond scission and N_2 recombinative desorption as possible rate determining steps. An increase in N-binding energy facilitates N-H bond scission (therefore increasing activity), however, when the N-binding energy becomes too strong N_2 desorption is hindered, thereby lowering activity.

Research into ways of tuning the binding energy of metals to make more active catalysts has become a prominent area over the last 10 years with numerous approaches and model catalysts being developed. As discussed in the previous chapter, Norskov and co-workers used periodic table interpolation – that the binding energy of an alloy is a linear combination of that of the parent metals – to predict and demonstrate CoMo is an active catalyst for ammonia synthesis (another reaction for which N-binding energy is used as a descriptor).[7] This was subsequently shown to be active for ammonia

decomposition by a number of groups.[8] Hansgen *et al.* argue that periodic table interpolation and alloying is not a suitable method to predict active catalysts as under reaction conditions particles undergo phenomena such as surface segregation to minimise surface energy and be in the most thermodynamically stable phase.[5] Therefore, investigation from this group has focussed on the binding energy of bimetallic surfaces and sub-surfaces and the subsequent preparation of these surfaces to corroborate the theoretical calculations. They have predicted and demonstrated numerous active surfaces such as Fe-Pt-Pt, Ni-Pt-Pt and Co-Pt-Pt (where Fe, Ni or Co were modelled as a monolayer on top of a bulk of Pt) as well as demonstrating the corresponding sub-surfaces, Pt-M-Pt (where the Fe, Ni or Co are under a surface monolayer of Pt), to be inactive.[2]

This chapter focusses on preparation of supported metal nanoparticle catalysts that are inspired by these model systems. As Fe-Pt is predicted to be active as an alloy by periodic table interpolation and as a segregated surface, the investigation starts with the preparation of $Fe-Pt/Al_2O_3$. This chapter also documents reactor engineering challenges that were encountered during the initial stages of this research and the investigation into the cause.

4.1.2 Aims

In chapter 3, we saw that CVI can be used as a suitable preparation method for preparing supported nanoparticle catalysts while minimising Cl^- poisons. We also saw that by computationally assisted design, bimetallic catalysts can show synergistic effects in bulk materials. The aim of this chapter is to investigate the applicability of periodic table interpolation to supported alloy nanoparticles. Two CVI preparation methods will be investigated for the preparation of alloys and the electronic structure of these alloys will be probed using spectroscopic techniques and microscopy. While much previous work has been focussed on the highly active CoMo alloy catalysts designed using periodic table interpolation, these are bulk materials with well-defined

structures. Active nanoparticles, with more complex and varying structures, may present a larger challenge to predict.

4.2 Importance of Reactor Design in Catalyst Testing

4.2.1 Affinity of Pt with Stainless Steel Reaction Tubes

This section details the investigation into the use of stainless steel reactor tubes as mentioned in Chapter 2. Initial catalyst testing was carried out using 10 mm i.d. reactor tubes made from 316 stainless steel, however, it was noted that routine blank reactions (a reaction carried out with no catalyst present) would present ammonia decomposition activity. The present work focusses on the SEM investigation into the cause of this 'blank activity' and the steps taken to eliminate it.

A ~1 cm^2 sample was taken from the centre of a contaminated stainless steel tube along with two samples from new 316 stainless steel tubing in order to analyse the inner and outer surfaces as a control. These three samples are referred to as used, fresh inner and fresh outer respectively and are shown, mounted in the SEM, in Figure 1. It can be seen, even under low magnification that the fresh outer surface is pristine, the fresh inner surface shows minor contamination (possibly as a factor of the tube manufacturing process) and scratching, and the used surface is heavily damaged.
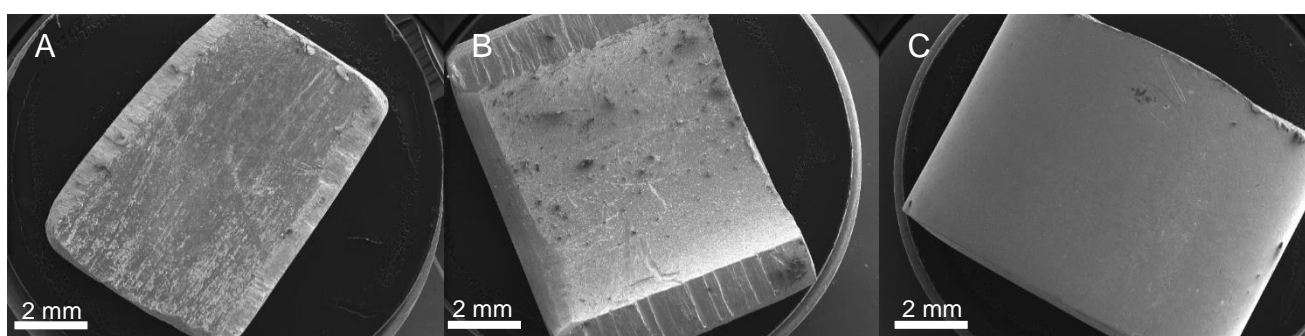

Figure 1: Low-zoom images of: a) Used, b) Fresh Inner and c) Fresh Outer surfaces mounted in the SEM

SEM-EDX analysis of the fresh outer surface was performed in order to have a control surface. Elemental mapping was performed and is shown in Figure 2. From this, elemental composition was calculated and is shown in Table 1. It was observed that all metal components are homogeneously distributed and that the elemental composition of the steel conforms to the expected composition of 316 stainless steel, as shown in the reference data from Swagelok,[9] also shown in Table 1.
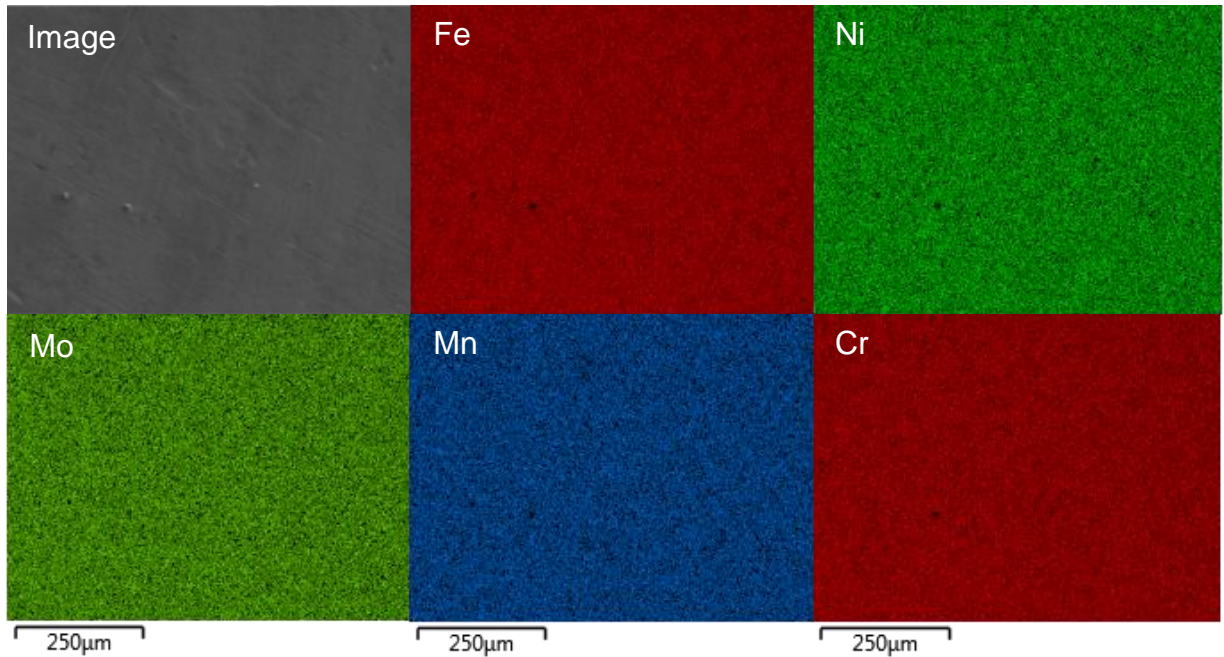
Figure 2: Elemental mapping of five major constituents of stainless steel in fresh outer surface

Table 1: Composition of 316 stainless steel as supplied by Swagelok[9] and as analysed by SEM-EDX

Element	SEM Composition (wt%)	Swagelok Composition (wt%)
O	1.68	-
Si	0.44	1.00 max.
Ca	0.13	-
Cr	17.86	17.00 – 19.00
Mn	1.64	2.00 max.
Fe	62.97	Balance
Ni	12.58	12.50 – 15.00
Mo	2.70	2.50 – 3.00

Analysis of the fresh inner surface reveals that it is less pristine than the fresh outer surface and is shown in Figure 3. Defects such as scratches are observed, possibly caused in the cutting of the cross-section, and surface contaminants are readily visible in the electron image. Elemental mapping reveals this contamination to contain C and O, possibly indicating an organic species left on the surface from the tube forming process. The three steel constituents shown – Fe, Ni and Cr – still appear homogeneously distributed through the sample.
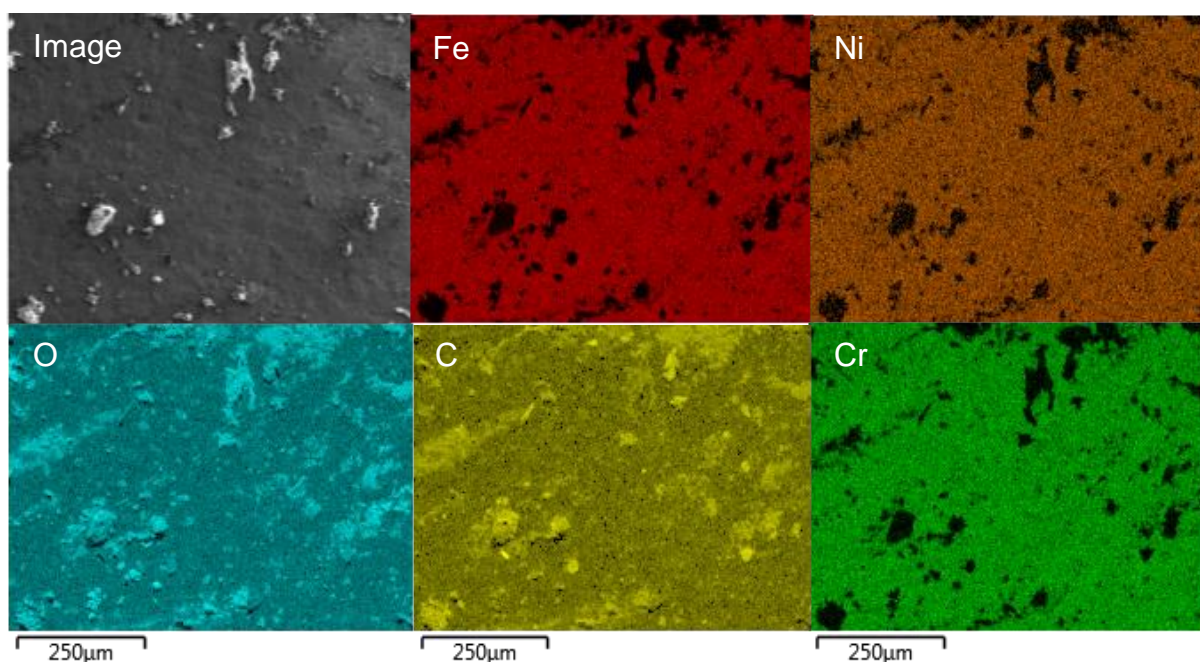

Figure 3: Elemental mapping of stainless steel components and contaminants on fresh inner surface

Elemental mapping of the used tube sample is shown in Figure 4 and it is clear from these images that the surface of the stainless steel has been changed in two ways. Firstly, the stainless steel itself has restructured and metals in the alloy have segregated. The Fe, Ni and Cr that were homogeneously distributed in the previous two samples have segregated into an area of more concentrated Cr and Ni, and an area of more concentrated Fe. N is also observed on the surface with a slightly higher concentration in the Fe region. This N most likely comes from the decomposed NH_3 and has formed a nitride with the segregated Fe. Secondly, Pt has leached from the catalysts tested and coated the inside surface of the reaction tube. The Pt can be seen strongly in the same regions as the Cr and Ni. It is believed that it is this leached Pt,

accumulated over a number of tests, which has led to the activity of the blank tube.
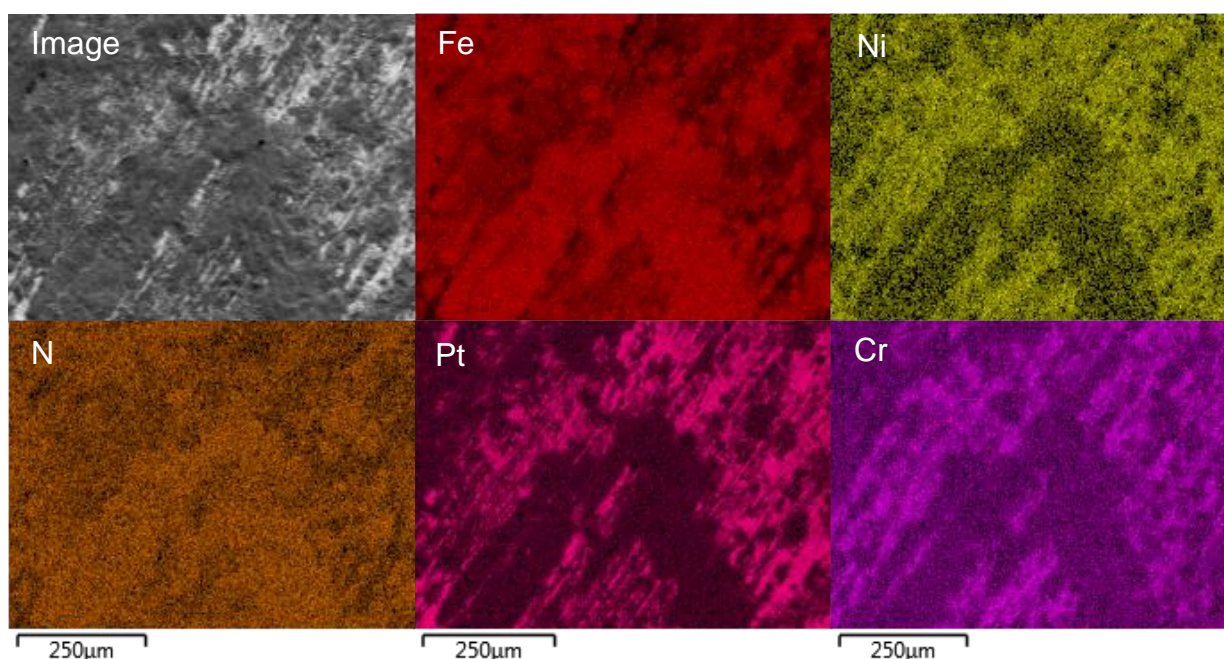

Figure 4: Elemental mapping of stainless steel components exhibiting segregation and evidence of Pt leaching

Finally, high-zoom images of a region of Pt contamination and its elemental mapping is shown in Figure 5. The Pt contaminant is evident in the BSD image as a bright region, however, there are also darker spots on the contamination suggesting elements of a far lower atomic mass. Elemental mapping confirms that the bright regions are Pt and shows that the dark regions evident in the BSD image contain Al and O. This suggests that it is not only the metal that has fused onto the reaction tube but also, to a lesser extent, some of the support material. Segregation of the steel components is not as evident in these images, with the exception of an area of lower intensity in the Fe mapping. However, this should not be misattributed to segregation as a much more likely explanation is the shielding effect of Pt on top of the Fe.

In conclusion, it has been demonstrated that repeated testing of Al_2O_3-supported Pt-containing catalysts leads to deposition of the metal onto the stainless steel tube which is then active for future reactions. It has also been shown that the Al_2O_3 support also fuses to a lower degree. Due to this investigation, all further tests were carried out using quartz reactor tubes (i.d.= 6 mm).
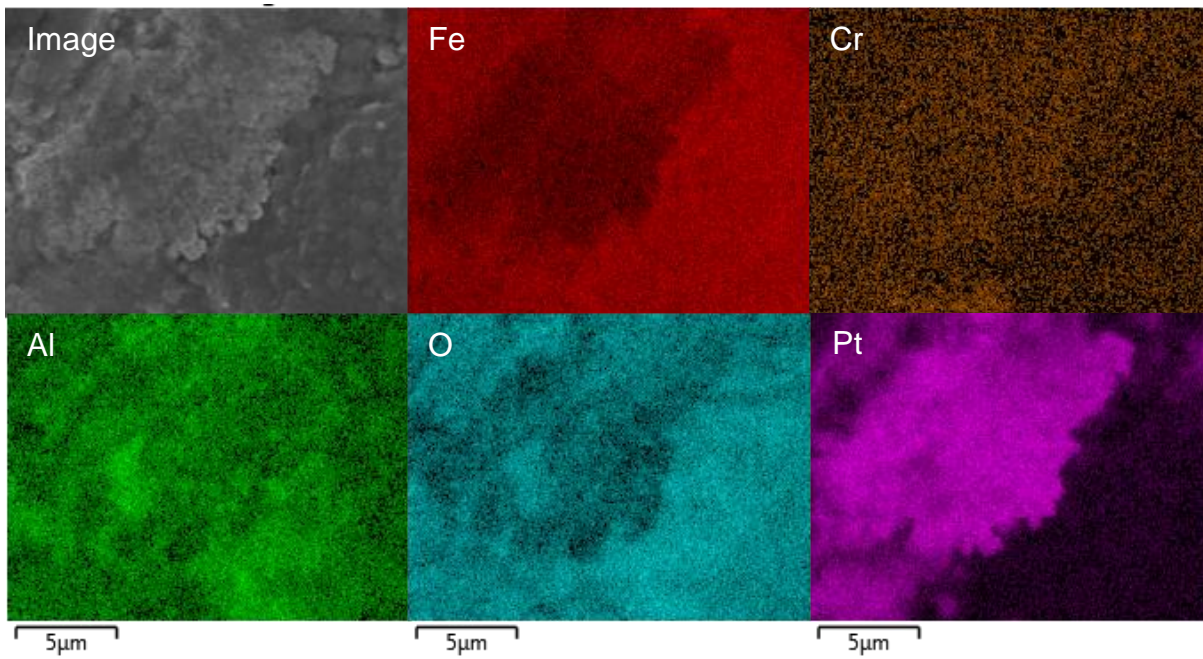
Figure 5: Elemental mapping of two stainless steel components and three contaminants from Al_2O_3 supported catalysts

4.3 Fe-Pt Alloy Catalysts

4.3.1 Preparation and testing of Fe-Pt bimetallic catalysts

Initially, a series of 5% Fe-Pt/Al_2O_3 catalysts were prepared by a sequential CVI technique whereby a Pt/Al_2O_3 catalyst was prepared with the desired weight loading of Pt using CVI, reduced at 550 °C and then a second CVI with Fe was performed before a further reduction at 550 °C. The aim of this preparation method was to form metallic Pt seeds onto which an Fe layer would be deposited to form the Fe-Pt-Pt surface that was predicted to be active by Hansgen *et al.*[2,5] The following catalyst compositions were prepared and tested and are shown in Figure 6: Fe_{100}, $Fe_{80}Pt_{20}$, $Fe_{60}Pt_{40}$, $Fe_{40}Pt_{60}$, $Fe_{20}Pt_{80}$ and Pt_{100}, where the subscript relates to the molar ratio of metals. There is a synergistic effect observed, with all Fe-Pt catalysts being more active than the parent metals. As the bimetallic catalysts become more Fe-rich the activity increases to a maximum of 71% for the $Fe_{80}Pt_{20}$ catalyst. This synergy could be due to alloying of the metals, an Fe monolayer being formed over the Pt nanoparticles (proposed by Hansgen et al.[10] to be a highly active structure) or promotion of one metal by the other.
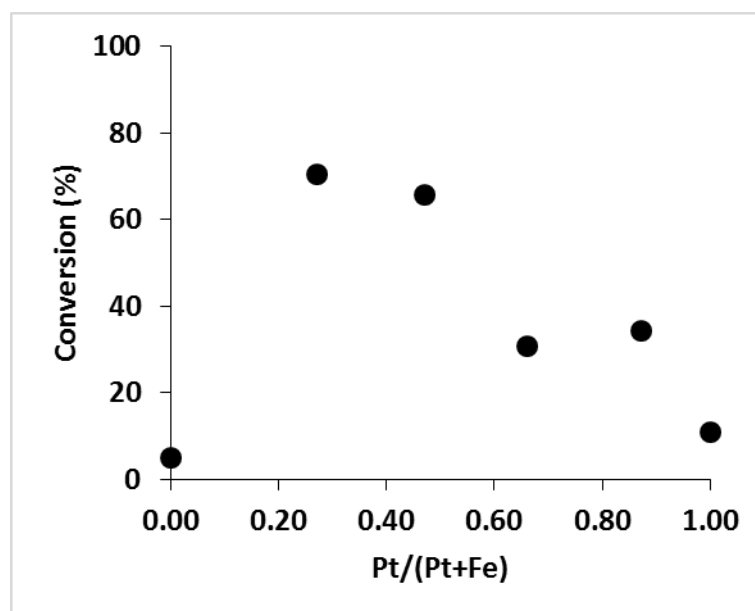

Figure 6: Conversion of ammonia by 5%Fe-Pt/Al_2O_3 prepared by seq-CVI

An analogous series of Fe-Pt/Al$_2$O$_3$ catalysts were prepared by co-CVI, with Fe and Pt being impregnated simultaneously followed by one reduction at 550 °C. This is a much more efficient preparation with half the number of CVI and reduction steps. Activity measurements for these catalysts are shown in Figure 7. These catalysts exhibit the same synergy as the series prepared by seq-CVI and follow the same trend; that an increase in Fe content leads to a higher conversion. However, catalysts prepared by co-CVI show a greater synergistic effect, with the most active catalyst, also Fe$_{80}$Pt$_{20}$, converting 80% ammonia at 500 °C. This could be due to a greater extent of alloying, presence/absence of an Fe monolayer or another factor and is investigated through the use of numerous characterisation techniques.
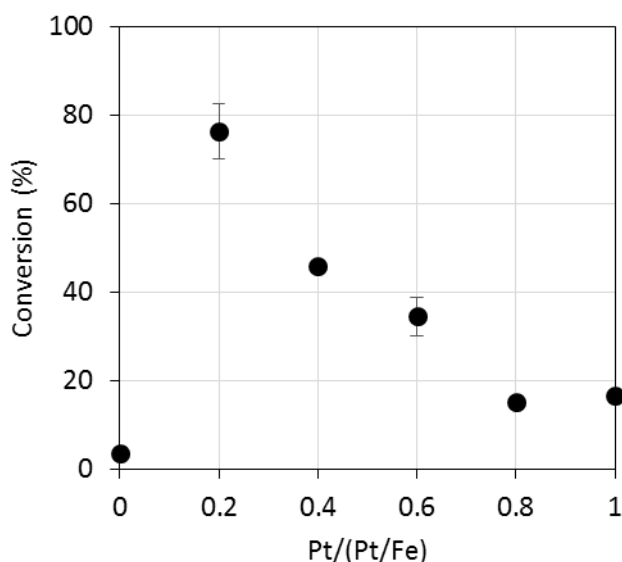

Figure 7: Conversion of ammonia by 5%Fe-Pt/Al$_2$O$_3$ prepared by co-CVI

Each test for the co-CVI catalysts was performed three times and error bars are presented showing the standard deviation. The errors are also presented in Table 2 as many of them are too small to be observed. These results show that this testing protocol is reproducible and that the results are reliable.

Catalyst	Conversion (%)	Standard Deviation
Fe_{100}	3.5	0.4
$Fe_{80}Pt_{20}$	76.2	6.3
$Fe_{60}Pt_{40}$	45.8	0.4
$Fe_{40}Pt_{60}$	34.4	4.3
$Fe_{20}Pt_{80}$	15.1	0.5
Pt_{100}	16.6	0.9

4.3.2 Characterisation of Fe-Pt bimetallic catalysts

4.3.2.1 XRD

Powder X-ray diffraction was performed on both series of catalysts and the Al₂O₃ support and are shown in Figure 8. The Al₂O₃ is largely amorphous, with three broad reflections of low intensity at 37, 47 and 68 ° (●). This is consistent with literature data.[11] The seq-CVI catalysts present sharp, crystalline peaks at 39 and 46 ° (▲) which correspond to metallic Pt (111) and (200) reflections respectively[12,13] and become more intense as the Pt content of the catalyst
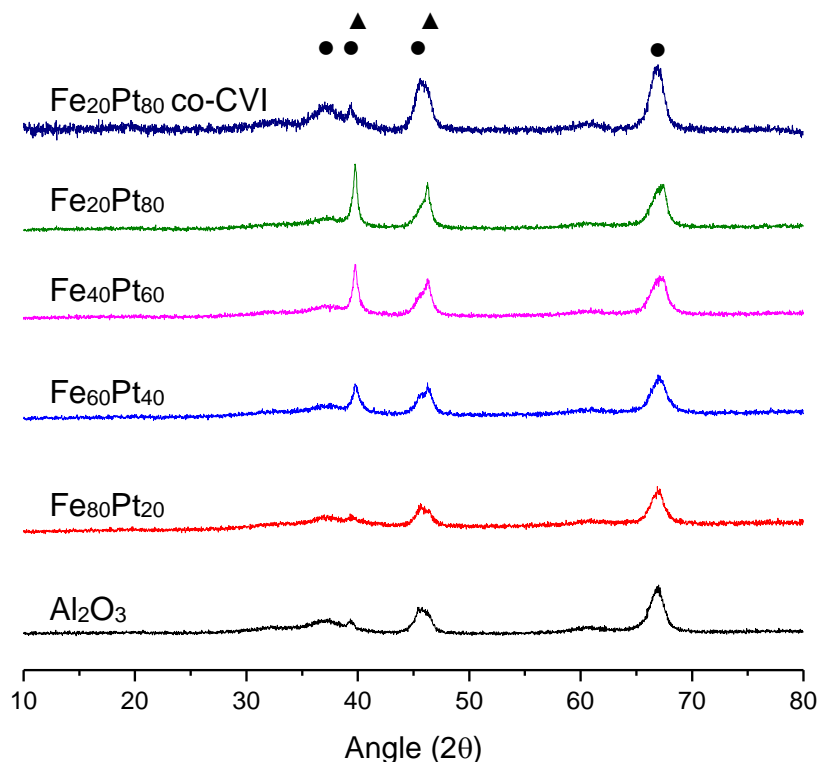

Figure 8: XRD patterns of Fe-Pt/Al₂O₃ catalyst prepared by seq-CVI and co-CVI

increases. Crystallite size calculations using the Scherrer equation were carried out and are shown in Table 3. This suggests that the activity trend shown in Figure 6 for Fe-Pt catalysts prepared by seq-CVI is due to a particle size effect, with the smaller Pt particle size catalysts giving a higher conversion.

Diffraction patterns for the catalysts prepared by co-CVI only show reflections due to the Al_2O_3 support and lack the reflections at 39 and 46 °, which suggests there are no large Pt particles. This may suggest that the activity trend for co-CVI is not due to particle size, unlike catalysts prepared by seq-CVI, however this would require further particle size analysis by electron microscopy. This demonstrates that by impregnating both metals simultaneously, particle growth is limited. This could be due to the presence of Fe preventing Pt agglomeration or due to fewer heat treatments.

Table 3: Pt crystallite size as calculated by the Scherrer equation

Catalyst	Pt Crystallite Size (nm)
$Fe_{80}Pt_{20}/Al_2O_3$	N/A
$Fe_{60}Pt_{40}/Al_2O_3$	9.0
$Fe_{40}Pt_{60}/Al_2O_3$	8.2
$Fe_{20}Pt_{80}/Al_2O_3$	11.0
Al_2O_3	N/A

4.3.2.2 Seq-CVI Catalysts: Effect of metal ratio on particle size

The TEM in this section was performed by Qian He in Cardiff (Seq-CVI samples) and Li Lu in Lehigh University (Co-CVI samples). TEM was used to confirm the particle size effects recognised through XRD and to investigate the form of Fe and Pt on the catalyst. Micrographs of $Fe_{80}Pt_{20}$ and $Fe_{20}Pt_{80}$ prepared by seq-CVI are shown in Figure 9$_{a+b}$. It is immediately evident from the images that the nanoparticles of the $Fe_{20}Pt_{80}$ catalyst are far larger than those of the $Fe_{80}Pt_{20}$ catalyst, confirming what was observed through XRD. It is also of note that many of the particles show no evidence of alloying such as

lattice planes of alternating intensity and this suggests that a lot of the Pt is present as metallic Pt nanoparticles in both $Fe_{80}Pt_{20}$ and $Fe_{20}Pt_{80}$.
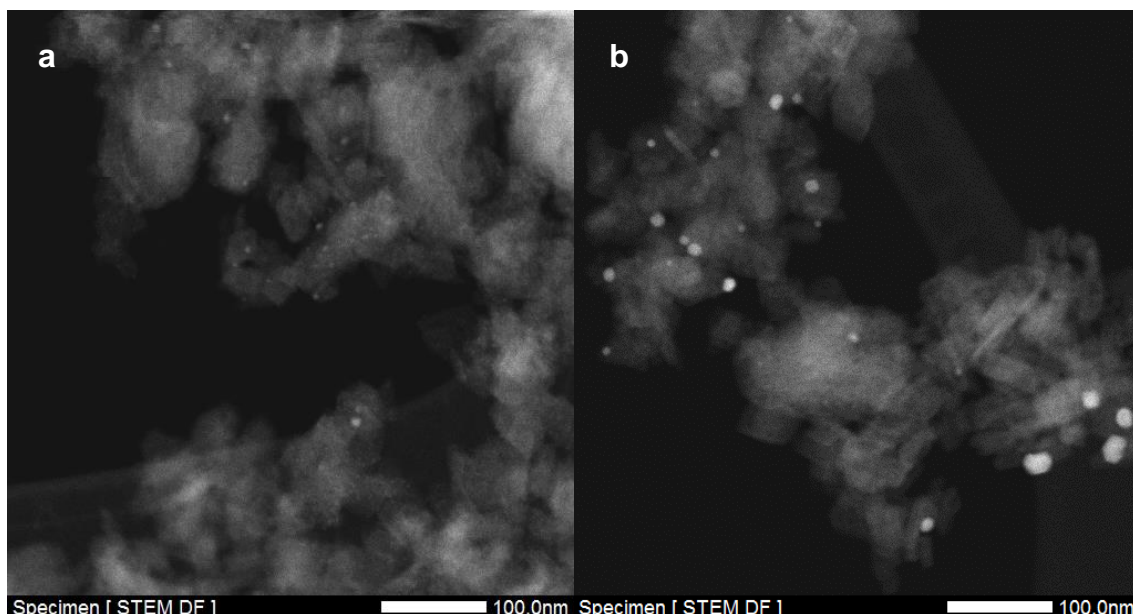
Figure 9: TEM micrographs of: (a) $Fe_{80}Pt_{20}$, (b) $Fe_{20}Pt_{80}$ catalysts prepared by seq-CVI

Particle size distributions and mean-particle size are shown in Figure 10. The mean particle size compares favourably to the values calculated by the Scherrer equation and support the suggestion that the activity trend of Fe-Pt catalysts prepared by seq-CVI is due to particle size, with the higher Fe content catalysts containing smaller, more active nanoparticles than those with a higher Pt content. It is shown that the particle size distribution is very broad, demonstrating that the seq-CVI method has limited particle size control.
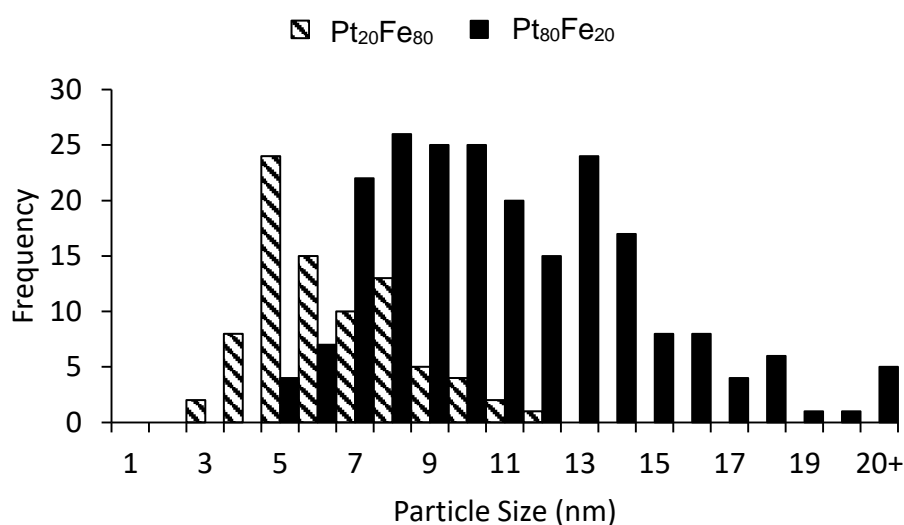
Figure 10: Particle size distributions of catalysts of different ratios prepared by seq-CVI

4.3.2.3   Investigating the Alloy Phase in co-CVI

In order to attribute the activity of these catalysts to periodic table interpolation, it is essential to demonstrate that the metals have formed alloys. To do this HR-STEM was performed on the most active Fe-Pt catalyst, $Fe_{80}Pt_{20}$, prepared by co-CVI before use and after 20 h testing. Figure 11a+b show the catalyst before use,, where it is evident that the prepared catalyst contains small, well-alloyed particles. Both images show the particles to contain tetragonal FePt alloy, with the particle in (a) exhibiting alternating intensity and fitting projections of the (001) plane and the particle in (b) fitting with the (111) projection, which does not show alternating intensity.
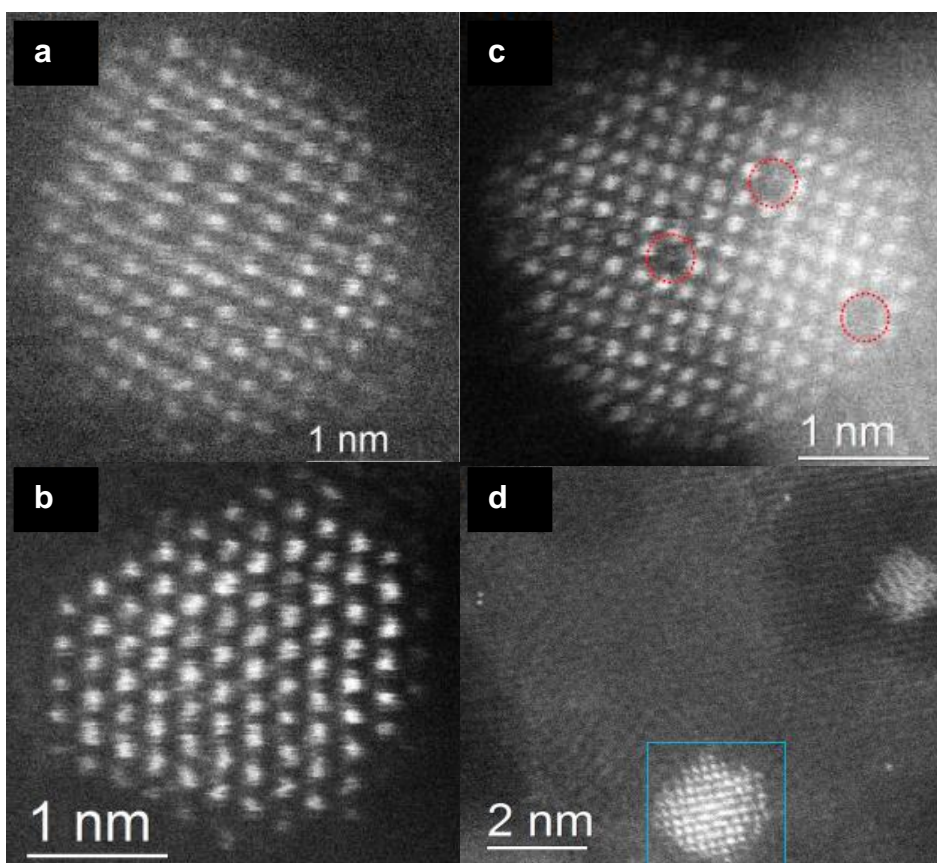
Figure 11: STEM images of $Fe_{80}Pt_{20}$ catalyst prepared by co-CVI: Fresh (a)+(b) and following 20 h reaction (c)+(d).

Metal concentrations calculated by EDS analysis are shown in Figure 12 and Table 4. It showed that a high concentration of Fe and a low concentration of Pt is highly dispersed across the support, including atomically dispersed

species. This high background signal for both elements means accurate metal composition of the nanoparticles is not possible. Due to these limitations, it is not possible to accurately model the Fe-Pt alloy particles or to correlate the activity to actual particle composition as would be required to conclusively investigate the practical application of the periodic table interpolation design method. One way of overcoming this would be the preparation of model surfaces and catalysts such as thin films or colloidal alloy nanoparticles in which the metal composition can be better controlled and characterised.

Table 4: Elemental composition of the regions shown in Figure 12 by EDS

Region	Fe Conc. (%)	Pt Conc. (%)
Particle	79.04	20.96
(Blue box)	±3.78	±2.03
Background	90.46	9.54
(Red box)	±5.04	±2.30
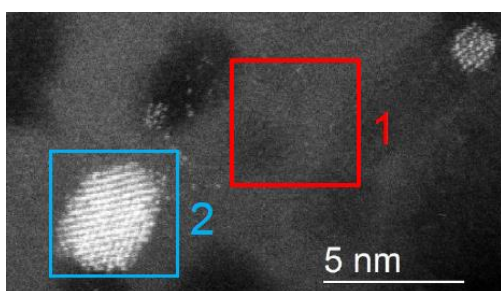
Figure 12: STEM image of a region of Fe$_{80}$Pt$_{20}$ prepared by co-CVI for EDS analysis

Figure 11c+d show particles after 20 h testing. The testing data is presented in Figure 13 and shows that the catalyst activity is very stable over this period. Under reaction conditions the particles maintain their alloying and small size, however, they lose their structure. In Fig. 11(c) Pt vacancies or Fe-rich columns are formed during testing and the alloy structure is lost, indicating that metal segregation occurs under reaction conditions. Although this particle fits
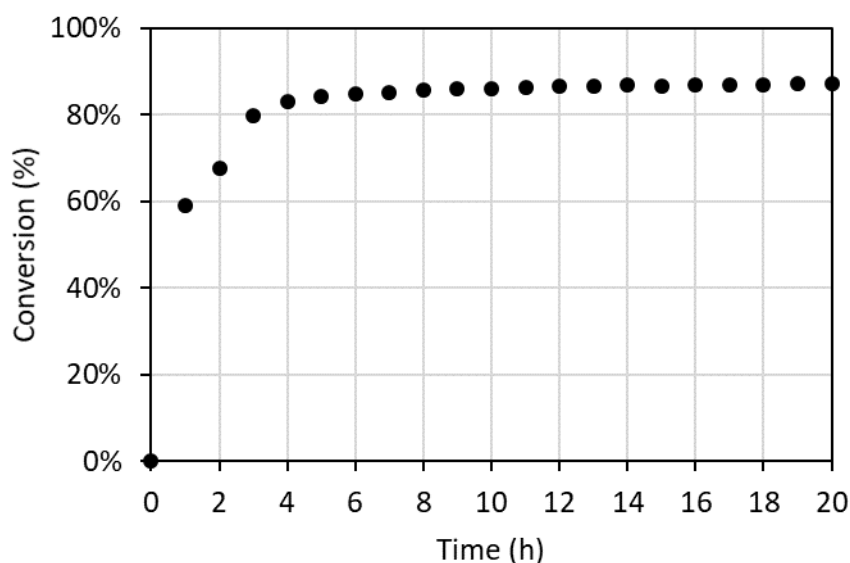
Figure 13: 20 h stability test of Fe$_{80}$Pt$_{20}$ prepared by co-CVI

with projections of the [001] plane of tetragonal FePt or the [001] plane of cubic $FePt_3$, both would exhibit alternating intensity, which this does not. This is also evident in particle (d), which fits with the same lattice projections, however does not exhibit alternating intensity.

EDS mapping of the post-reaction catalyst is shown in Figure 14 and confirms the presence of both metals in the nanoparticles and again indicates that both species are also highly dispersed over the support.
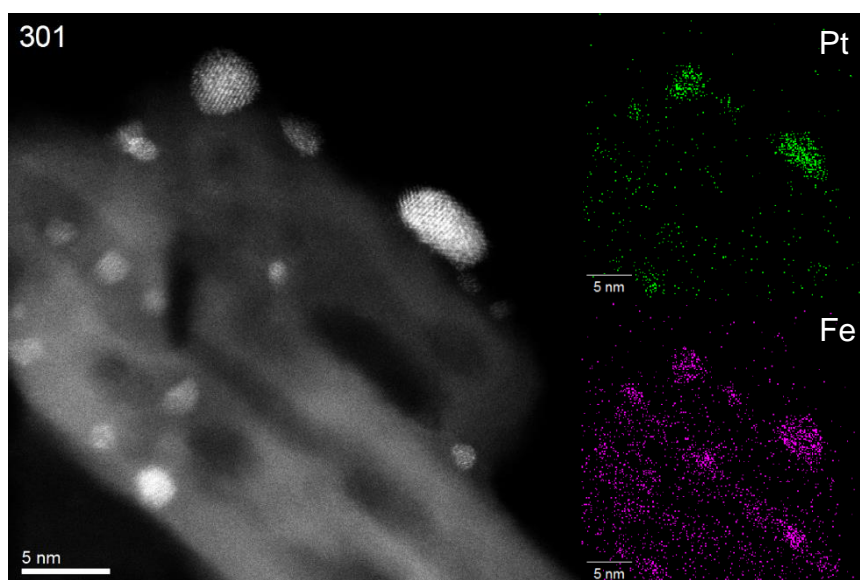
Figure 14: EDS maps of post-reaction 5% $Fe_{80}Pt_{20}/Al_2O_3$ prepared by co-CVI

Despite the re-structuring of the alloys after a prolonged testing period, the catalysts prepared by co-CVI show remarkable catalytic stability and the particle size does not increase, with the mean particle size of the fresh catalyst being 1.75 nm (n = 536) and the mean particle size of the used catalyst being 1.85 nm (n = 549). A small decrease in the number of 1.5-2 nm particles is observed along with a small increase in the number of 2.5-3 nm particles as shown in the particle size distributions in Figure 15. Microscopy shows that CVI can be used as a solvent-free method to produce small, well-dispersed and well-alloyed nanoparticles that are stable at temperatures up to 500 °C and for periods up to 20 h.
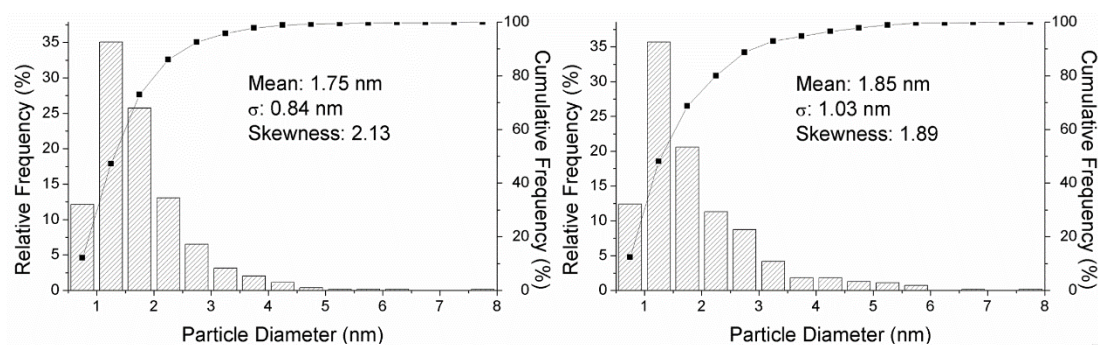
Figure 15: Particle size distributions for fresh (left) and tested (right) 5% $Fe_{80}Pt_{20}/Al_2O_3$ prepared by co-CVI

4.3.2.4   CO-DRIFTS of Fe-Pt/Al_2O_3 bimetallic catalysts

CO-DRIFTS is used to investigate the different Pt sites present in a catalyst as CO binds to different sites with characteristic modes such as linear or bridging. In this work, it is used to investigate the influence of alloying on the Pt structure. CO-DRIFTS experiments were carried out on Fe_{100}, $Fe_{80}Pt_{20}$ seq-CVI, $Fe_{80}Pt_{20}$ co-CVI and Pt_{100} catalysts and are shown in Figure 16. The supported Pt catalyst exhibited peaks at 2078 and 2056 cm^{-1}, which correspond to terrace and edge sites respectively.[14] Fe showed no interaction with CO, therefore no adsorption modes were observed. $Pt_{20}Fe_{80}$, as prepared by seq-CVI, shows a small peak between 2078 and 2056 cm^{-1}. This indicates that there is available Pt for the CO to bind to. However, when prepared by co-CVI the $Fe_{80}Pt_{20}$ catalyst demonstrated no adsorption of CO.
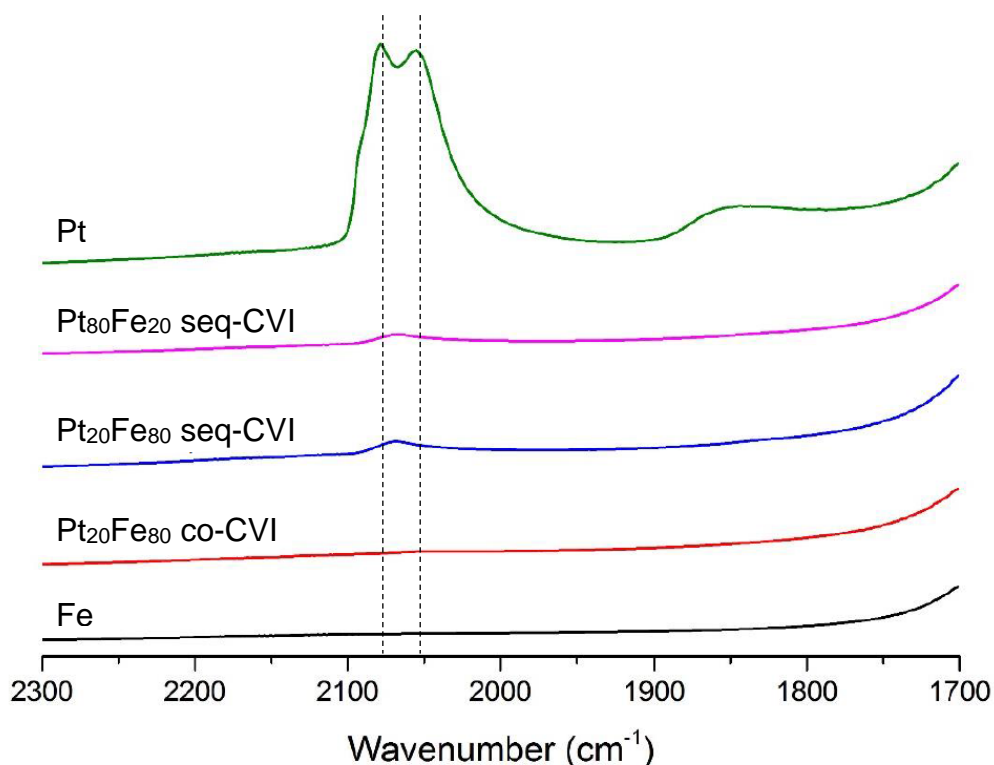
Figure 16: CO-DRIFTS of various Fe-Pt catalysts prepared by seq-CVI and co-CVI

The DRIFTS data suggests that when incorporated into an Fe-Pt alloy, the electronic structure of Pt is significantly changed so that it no longer interacts with the probe molecule. This electronic modification could be seen as evidence supporting the use of periodic table interpolation. The absence of CO-binding observed in the co-CVI catalyst confirms the observation by TEM that all Pt is present as a component of Fe-Pt alloy particles. It is important to note that this not due to Fe obscuring the Pt in a core-shell type structure as no particles of this type were observed using TEM. Also, if segregation was to occur, Pt would be the surface dominating species due to its lower surface energy. TEM images also showed that in the catalyst prepared by seq-CVI, although Fe-Pt nanoparticles are formed, a quantity of Pt is present as monometallic nanoparticles which exhibit CO-adsorption. The activity difference between the two preparation methods is therefore due to the extent of alloying, with co-CVI method leading to better alloying.

4.4 Fe-Pd Alloy Catalysts

To further investigate the robustness of interpolation as a catalyst design tool, Fe-Pd bimetallic catalysts were also investigated. Like Pt, Pd is relatively inactive for ammonia decomposition and is on the opposite side of the volcano plot to Fe asshown in figure 4 of the introduction. It is predicted that Fe-Pd catalysts will also show synergy and be active ammonia decomposition catalysts.

4.4.1 Testing of Fe-Pd/Al$_2$O$_3$ Catalysts

As co-CVI was shown to prepare catalysts that were better alloyed and with a narrower PSD than seq-CVI, this method was chosen to prepare four Fe-Pd/Al$_2$O$_3$ catalysts, analogous to the Fe-Pt series discussed previously. These four catalysts, along with the parent metals, were tested for ammonia decomposition and are shown in Figure 17.
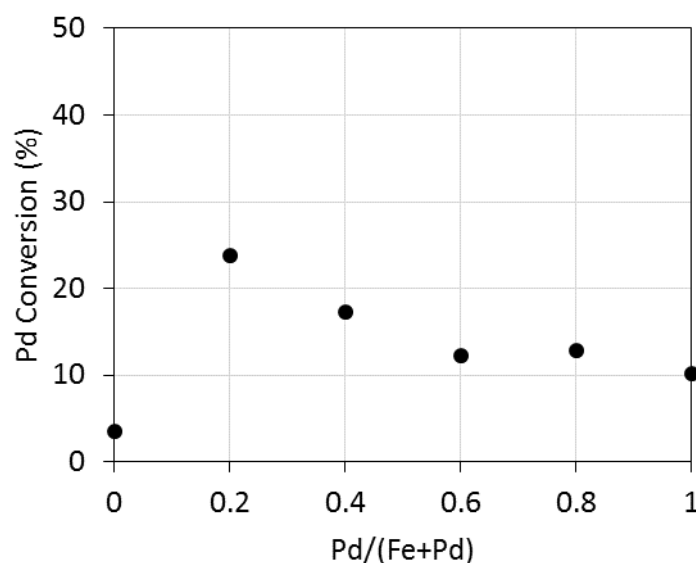
Figure 17: Conversion of ammonia by 5%Fe-Pd/Al$_2$O$_3$ catalysts

There are both similarities and differences when compared to the Fe-Pt catalysts. Like the Fe-Pt series, the Fe-Pd catalysts showed synergy, with all bimetallic catalysts being more active than the parent metals. The activity also increases as the Fe content of the catalysts increases, much like the Fe-Pt

catalysts ($Fe_{20}Pd_{80}$ is more active than $Fe_{40}Pd_{60}$; the cause of this is unknown and the difference is within experimental error). However, in comparison to the Fe-Pt catalysts, the Fe-Pd catalysts are relatively less active. Although there is synergy, the maximum conversion of an Fe-Pd catalyst is 23% in contrast to the 80% exhibited by the Fe-Pt catalysts. The causes of this were investigated through further characterisation.

4.4.2 Characterisation of Fe-Pd/Al_2O_3 Catalysts

4.4.2.1   XRD

Figure 18 shows the X-ray diffraction patterns of three of the Fe-Pd/Al_2O_3 catalysts and the monometallic Pd/Al_2O_3 ($Fe_{40}Pd_{60}$ was not used due to a lack of sample). The main feature of the patterns are the five peaks at 32, 37, 39, 47 and 68 ° labelled (●) which are characteristic of the support material.[11] However, there are two sharper peaks at 40 and 46 °, labelled (▲) that are due to Pd^0 (111) and (200) respectively.[15] These are most prominent in the Pd_{100} sample and get less intense as the Pd content of the catalysts decreases, with the peaks having disappeared in the $Fe_{80}Pd_{20}$ catalyst.
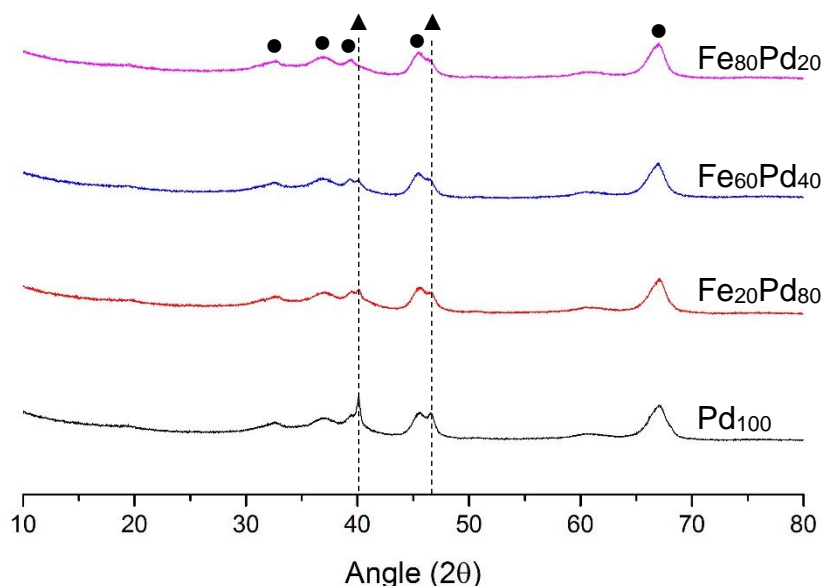
Figure 18: Diffraction patterns of Fe-Pd/Al_2O_3 catalysts

This is similar to the trend observed for the Fe-Pt catalysts prepared by seq-CVI whereby the precious metal was not fully incorporated into alloy nanoparticles. This suggests that although co-CVI was an optimal method for preparing alloyed Fe-Pt nanoparticles, it is not as suitable for Fe-Pd catalysts. This is unexpected as CVI has been shown to produce Zn-Pd alloys under similar conditions but may be due to small differences in sublimation temperature between $Pt(acac)_2$ and $Pd(acac)_2$. As with the seq-CVI prepared Fe-Pt catalysts, this characterisation suggests that the activity trend observed for ammonia decomposition testing might not be due to a synergistic effect of Fe-Pd alloying, but could rather be caused by smaller and more dispersed unalloyed Pd particles whose formation is facilitated either by the presence of Fe or the lower weight loading of Pd.

4.4.2.2   CO-DRIFTS

Figure 19 shows the CO-DRIFTS spectra from the carbonyl-binding region of the four Fe-Pd alloy catalysts and the Pd_{100} catalyst. The Pd_{100} spectra shows two distinct binding modes; one at 1979 cm^{-1} and one at 1940 cm^{-1}. Typically, the Pd CO-DRIFTS spectrum is split into a high frequency (2200-2000 cm^{-1}) region due to linear coordinated CO, and a lower frequency (2000-1800 cm^{-1}) region due to non-linear coordinated CO (bridged and hollow sites), as shown in the inset of figure 19.[16,17] The two peaks observed in this study have been assigned to bridge and hollow sites. The absence of a linear region is unexpected and the cause of it is unknown.
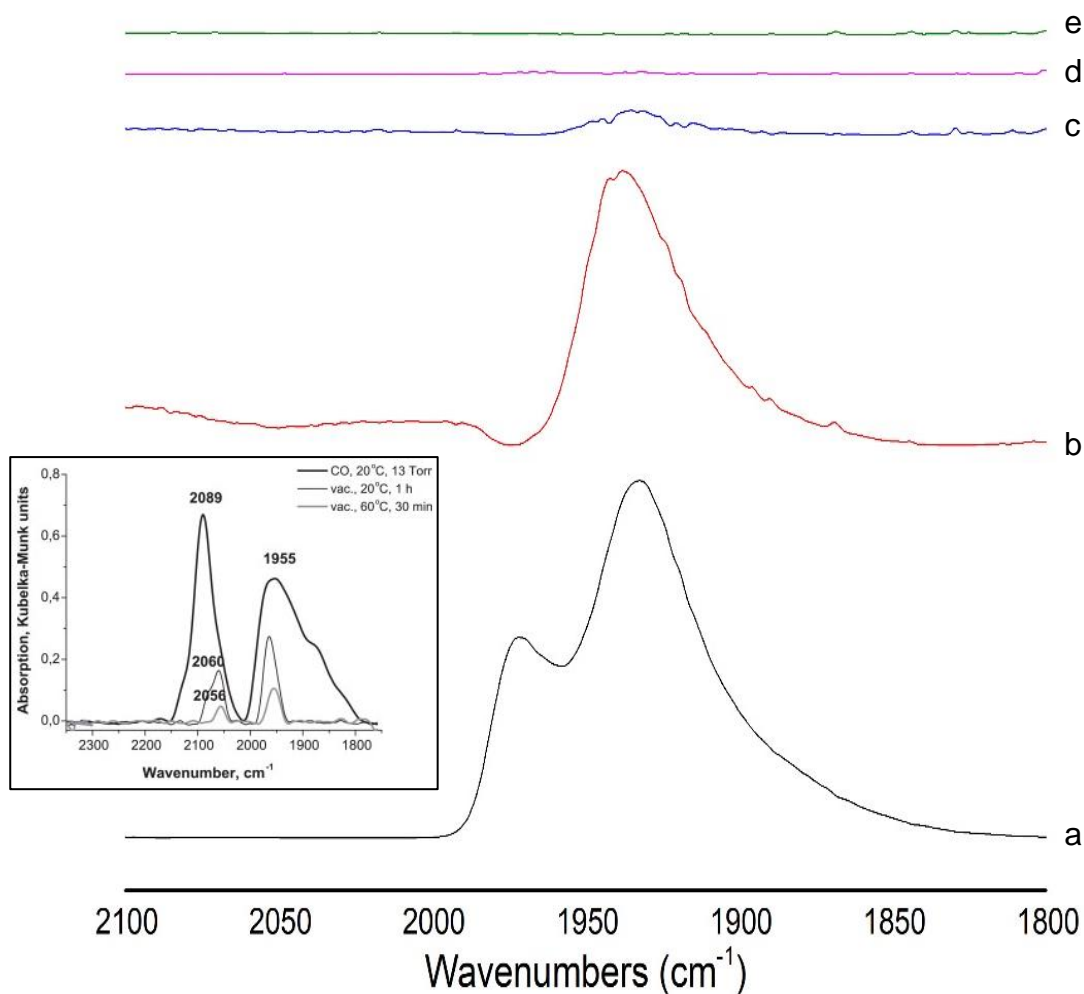
Figure 19: CO-DRIFTS spectra of: a) Pd_{100}, b) $Fe_{20}Pd_{80}$, c) $Fe_{40}Pd_{60}$, d) $Fe_{60}Fe_{40}$ and e) $Fe_{80}Pd_{20}$. Insert: Expected Pd CO-DRIFTS spectrum showing linear and non-linear regions reproduced from ref X.

The most Pd-rich alloy, $Fe_{20}Pd_{80}$ exhibits a binding mode at 1945 cm^{-1} corresponding to bridged carbonyl but no linear region is present. As linear carbonyl modes usually correspond to edge sites,[17] this would suggest that these Pd edge sites are lost due to the introduction of Fe. However, as Pd^0 reflections are still present in the XRD diffraction patterns, these edge sites cannot be lost through alloying. As the Pd content of the alloys decreases, the binding modes decrease in intensity and are not present in the two most Fe-rich catalysts. The absence of binding modes in the Fe-rich catalysts suggests that the interactions between Fe and Pd due to alloying cause a difference in the electronic structure and because of this Pd no longer interacts with the probe molecule. It could also be that there is no exposed Pd because of Fe covering the Pd nanoparticles, however, such a structure was not observed in the TEM of the Fe-Pt catalysts. The relative surface energies of Fe and Pd also indicate that if segregation was to occur, Pd would dominate the surface due to its lower surface energy. This is consistent with the results seen for the Fe-Pt catalysts previously. The trend in decreasing intensity through the series could suggest either that the degree of electronic modification is proportional to the Fe content or that the Pd exhibiting the carbonyl binding is un-alloyed and as the Fe content increases the extent of alloying increases. The latter is a more reasonable explanation as it is consistent with the results of both the Fe-Pt catalysts and the XRD characterisation of these catalysts which show Pd^0 reflections; if all Pd was alloyed as is the implication of the former explanation then the Pd^0 XRD reflections would not be present.

4.5　Fe-Ni Alloy Catalysts

Fe-Ni was chosen as a third bimetallic catalyst to investigate for a number of reasons:

i) Like Pd and Pt, Ni is on the opposite side of the volcano plot to Fe (figures 4 and 8 of the introduction), however, it is much closer to the optimum binding energy than the other two. This means that instead of alloying Fe with another inactive metal and preparing an active catalyst, Fe will be alloyed with an already active metal.

ii) Ni is the other metal in group 10 (disregarding Ds for its unsuitableness for catalysis). Group 10 metals get less active for ammonia decomposition the further down the group, however, it was observed that the synergy when alloyed with Fe is greater down the group (although this is based only on two datapoints). This synergy could be dependent on another physical property, such as atomic radii, which increases down the group. As these metals are similar in atomic radii they will form substitutional alloys and the different atomic radii will cause the lattice to expand more or less. Furthermore, Ni is the only group 10 element with an atomic radius smaller than Fe and this may cause it to exhibit different trends to the other group 10 alloys.

4.5.1 Testing of Fe-Ni/Al$_2$O$_3$ Catalysts

As Ni is itself an active metal for ammonia decomposition, testing of catalysts and comparison of results had to be changed to investigate Fe-Ni/Al$_2$O$_3$ catalysts. Firstly, as Ni achieves close to equilibrium conversion at 500 °C, the reactions were compared at 450 °C so that the reaction is not mass transfer limited. Secondly, with Ni being many orders of magnitude more active than Fe, simply seeing if the alloys are more active than both parent metals may not suffice to confirm a synergistic effect. For this reason, an analogous catalyst series was produced of monometallic Ni catalysts. These catalysts contain the same weight loadings of Ni as is present in each alloy catalyst but without the Fe. For example, the 2% Ni/Al$_2$O$_3$ catalyst contains the same mass of Ni as the Fe$_{60}$Ni$_{40}$ catalyst but without any Fe. In this way, the effect of Fe addition to a Ni catalyst can be investigated.
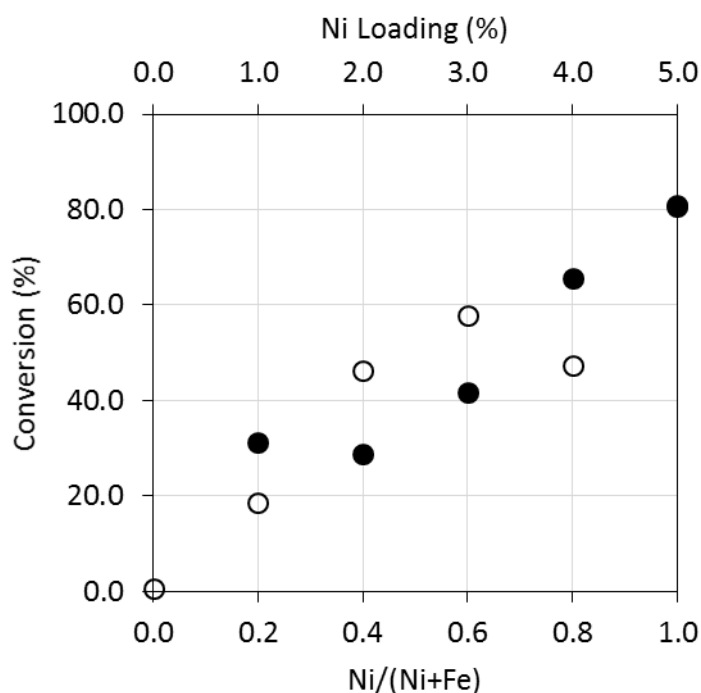
Figure 20: Conversion of ammonia by 5%Fe-Ni/Al$_2$O$_3$ catalysts (○)
when compared to monometallic Ni analogues (●)

The results of these tests are shown in Figure 20. At 450 °C, the Fe catalyst is inactive meaning that any increase in activity of the alloy catalysts over the Ni catalysts is not due to the presence of more metal but most likely the effect of alloying. Ni was shown to be an active catalyst, exhibiting 81% conversion, and this is consistent with previous investigations that attribute the activity to

a binding energy near to the optimum.[18] The activity of Ni-only catalysts decreases uniformly as the weight loading is decreased from 5 to 2%, however, the activity of the 1% Ni/Al_2O_3 is more active than that of the 2% catalyst. This may be due to particle size effects and a greater dispersion of metal and is investigated later in the chapter.

The alloy catalysts show the opposite trend to that of the Fe-Pt and Fe-Pd catalysts in that the activity increases as the Fe-content decreases. The least active alloy, $Fe_{80}Ni_{20}$, is less active than the Ni-only analogue, although as previously discussed, this catalyst shows an enhanced activity and it is possible that if this is due to higher dispersion the addition of Fe is inhibiting it. From the point of view of periodic table interpolation, this lack of synergy could be due to the high Fe-content altering the binding energy too far from the optimum. As Ni content increases, the alloy catalysts become more active than the Ni-only analogues. $Fe_{40}Ni_{60}$ and $Fe_{60}Ni_{40}$ both show enhancements in conversion of ~20% due to the addition of Fe. As the Fe is inactive at this temperature this suggests there may be an interaction between the metals, such as alloying or promotion, which is enhancing the activity of these catalysts.

4.5.2 Characterisation of Fe-Ni/Al_2O_3 Catalysts

4.5.2.1   XRD

Again, XRD was used as a means to investigate the presence of large nanoparticles and to confirm that the co-CVI method had facilitated the formation of small, well-dispersed nanoparticles as characterised in-depth in

4.3.2. Once more, only peaks due to γ-Al_2O_3 are observed, indicating that no large metal nanoparticles are present.
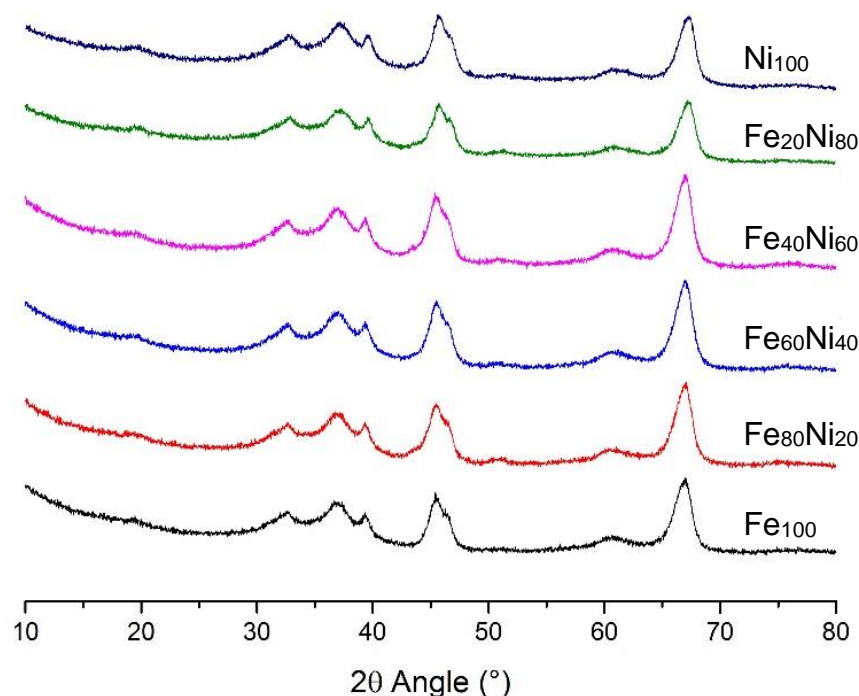
Figure 21: Diffraction patterns of Fe-Ni/Al_2O_3 catalysts

4.5.2.2 Ni Particle Size and Surface Area

The trend in activity of Ni catalysts with different weight loadings may be due to particle size effects. In order to investigate this, N_2O titration was used as it has been shown by Tada *et al.* to give accurate average particle size information when compared with microscopy.[19] Particle size is shown in Table 5, along with metal surface area and normalised activity.

Contrary to convention, as the weight loading of Ni decreases the particle size increases. The 5 wt.% Ni/Al_2O_3 exhibits the smallest nanoparticles of 1.8 nm, consistent with our previous work which shows that CVI prepares catalysts with particles ~2 nm. However, as the weight loading decreases, particle size increases to a maximum of 5.5 nm for the 1 wt.%Ni/Al_2O_3 catalyst. This could be due to the fewer Ni atoms deposited being more mobile and agglomerating easier. As a result of the lower loading and larger particle size, metal surface

area decreases through the series from 6 m^2/g to 0.4 m^2/g. These changes in particle size and metal surface area are shown to be linear in Figure 22.

Table 5: Particle size, metal surface area and normalised activity of Ni/Al2O3 catalysts of different weight loadings

Ni wt. Loading (%)	Ni Crystallite Size (nm)	Metal Surface Area (m^2/g)	Surface Normalised TOF (mol_{NH3}/m^2/h)
5	1.8	6.1	0.23
4	2.3	3.9	0.30
3	2.6	2.6	0.28
2	4.9	0.9	0.55
1	5.5	0.4	1.34

A surface normalised turnover frequency (TOF) was calculated and is shown in Table 5. It is evident from this that the particle size has a large effect on activity, with the 1% Ni/Al$_2$O$_3$ being the most active (1.34 mol_{NH3} m^{-2} h^{-1}) and the 5% Ni/Al$_2$O$_3$ catalyst being the least active (0.23 mol_{NH3} m^{-2} h^{-1}). The 5%, 4% and 3%Ni catalyst have particle sizes between 1.8-2.6 nm and exhibit a similar activity, however, when the particle size doubles to 4.9 nm in the 2%Ni catalyst that the activity also doubles and carries on increasing as the particle size reaches a maximum of 5.5 nm. As discussed in more depth in the
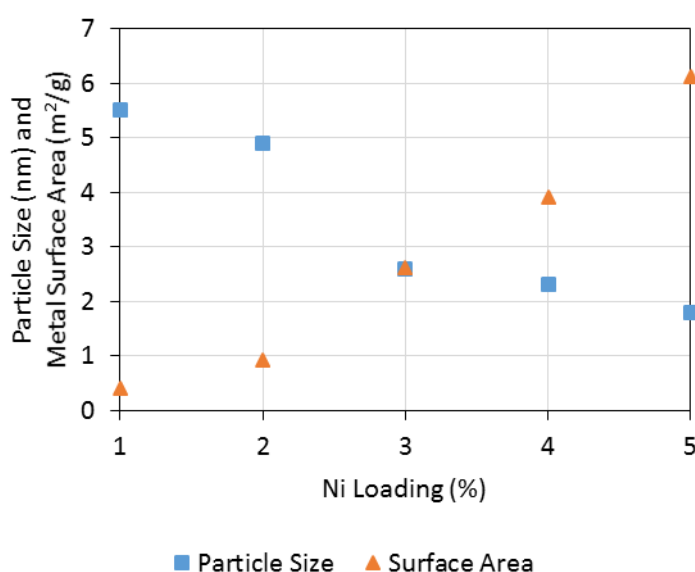
Figure 22: Ni particle size and surface area changes as a function of weight loading

introduction, it has been shown that for both Ru and Ni the active site is a B_5 site where the Ru or Ni has 5 nearest neighbours.[20–22] Because of this, very small nanoparticles (<2 nm) are often less active as they have a lower number of these active sites. They also have a different electronic structure due to the lower number of atoms. Therefore, the larger particles observed in the 1% Ni and 2% Ni samples could be more active due to a higher number of B_5 active sites.

4.5.2.3 EELS Mapping

In order to confirm whether Fe and Ni form an alloy when prepared by co-CVI, EELS elemental mapping was carried out on the most Ni-rich catalyst, $Fe_{20}Ni_{80}$ and is shown in Figure 23. Unlike the STEM images of Fe-Pt catalysts, Fe and Ni are of comparable atomic mass and thus do not contrast. However, by use of EELS elemental mapping it is evident that Fe and Ni are both present in the same regions (nanoparticles) and are assumed to be present as an alloy due to their readiness to alloy.[23] Again, Fe appears to be highly dispersed over the support surface, consistent with the EDS of the Fe-Pt catalysts.

As these maps suggest that the Fe and Ni are forming alloy particles and yet the activity of this catalyst is less active than its monometallic analogue, this suggests that the use of periodic table interpolation as a design method is limited. The activity of the monometallic analogue was shown to be due to its large particle size, which leads to a higher number of the highly-active B_5 sites, it is therefore likely that by alloying with Fe these B_5 sites are lost and the activity of the catalyst decreases.
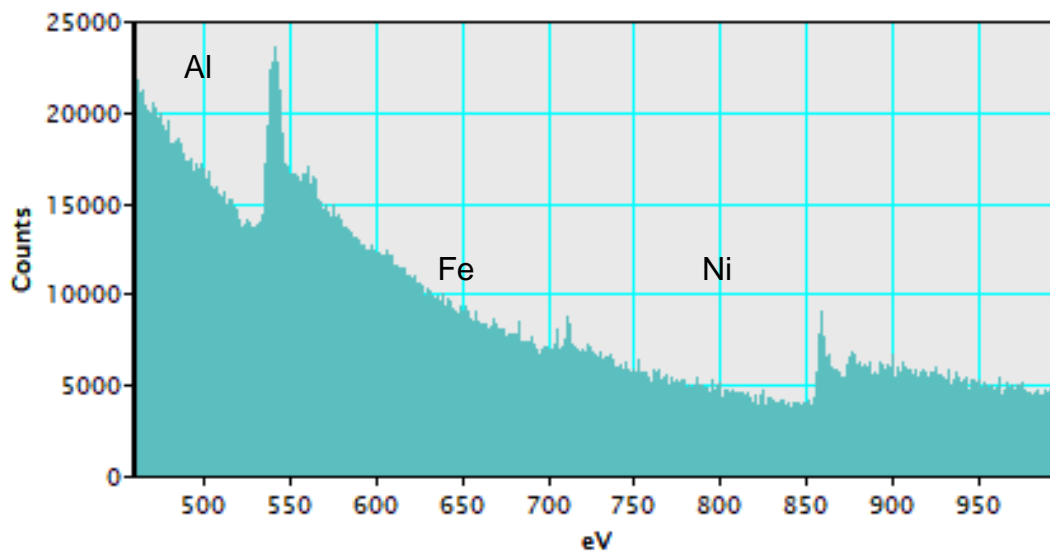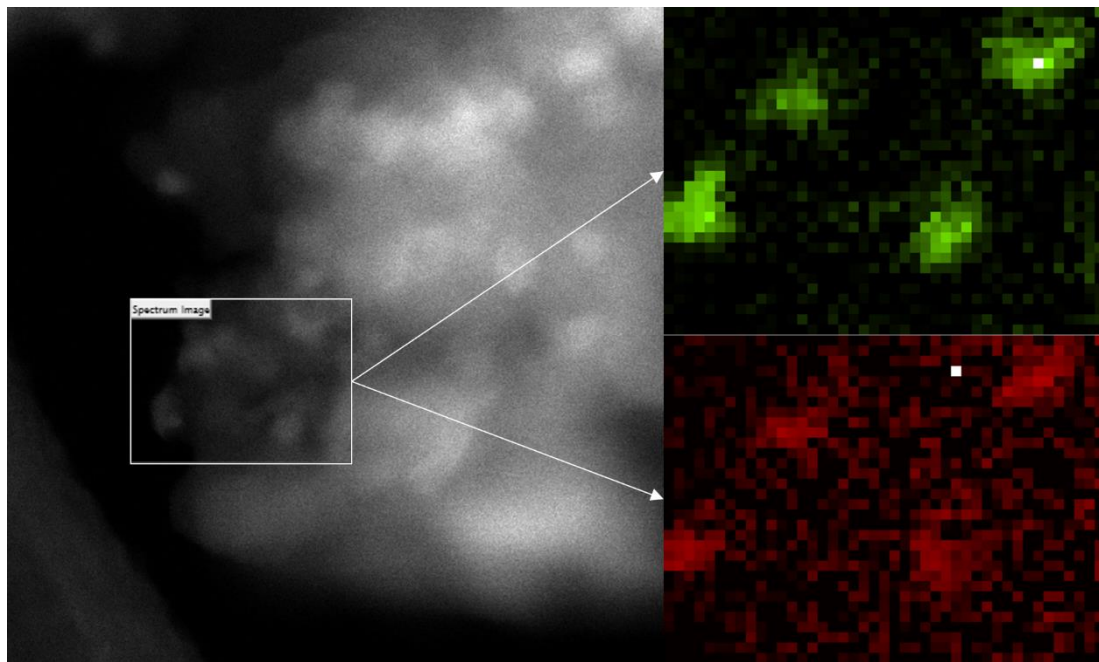
Figure 23: Top - EELS image of an area of 5% $Ni_{80}Fe_{20}/Al_2O_3$ showing Fe (red) and Ni (green). The white spots are due to missing pixels
*Bottom – EELS spectrum of the bottom left particle showing peaks due to Fe (711 eV) and Ni (859 eV)*

4.6 Conclusions

Various ratios of Fe-Pt, Fe-Pd and Fe-Ni catalysts were prepared, tested and thoroughly characterised. These catalysts had been predicted to be active through their optimised N-binding energy via either periodic table interpolation or layered bimetallic surfaces. All three of these alloy catalysts showed some degree of synergy indicating that N-binding energy can be used to assist in predicting novel active alloy catalysts. Fe-Pt showed the greatest enhancement in activity, whereas Ni catalysts showed the highest overall activity. The enhancement observed for Fe-Pd was modest, however, it did follow the same trend as Fe-Pt.

Fe-Pt catalysts showed an increase in activity as the Fe-content increased. Characterisation by TEM and CO-DRIFTS showed that these catalysts contained Fe-Pt alloy nanoparticles and the extent of alloying was seen to increase as the Fe content increased. This suggested that the active species was alloyed Fe-Pt nanoparticles. CO-DRIFTS showed that the electronic structure of the alloyed Fe-Pt nanoparticles had been modified as the Pt contained therein no longer facilitated CO adsorption. Therefore, a potential cause of the activity enhancement of these alloyed catalysts could be due to a shift in their N_2-binding energy and thus sit closer to Ru on the volcano plot. This would support the hypothesis of periodic table interpolation. However, STEM and EDS of the fresh catalyst has shown that there is heterogeneity in nanoparticles throughout the sample and post-reaction samples show a high-degree of restructuring, possibly due to segregation. Because of this the active site cannot be accurately identified or modelled and without an accurate description of the active site, conclusive evidence of periodic table interpolation cannot be provided.

Fe-Pd catalysts showed similar effects to the Fe-Pt catalysts when examined by CO-DRIFTS in that the extent of alloying increased with Fe-content and the most active catalysts had been electronically modified and no longer facilitated CO binding. However, XRD analysis indicates there are non-alloyed Pd nanoparticles that get smaller as the Fe content increases. Again, this heterogeneity in the catalyst sample makes identifying the active site difficult

and suggests that the data supporting periodic table interpolation is inconclusive. Although Fe-Pd is shown to be electronically different to Pd, and if this is the active site then this would support the design hypothesis; the modest enhancement in activity could also be due to the particle size of Pd that decreases in correlation with activity.

The Fe-Ni catalysts are the only series in which the activity of alloys is not more active than that of the parent metals. The alloys were compared with monometallic Ni catalysts of equivalent weight loading and only two alloys showed enhanced activity over these monometallic analogues. When these monometallic Ni catalysts were characterised it was shown that as the weight loading decreased, large particles that were more active were formed. It is unlikely that the binding energy changes as a function of particle size (at least when particles >1-2 nm and act as a continuous surface) and it is believed that these large particles were more active due to the increased number of B_5 sites, which are known to be the active site for the reaction on Ni. Alloying Ni with Fe may result in a lowering of the number of B_5 sites and this is why the Fe-Ni catalysts are less active.

In conclusion, this work shows that although N-binding energy is a good descriptor for the reaction and can be used to aid in the prediction of active novel alloys. However, this proposition has limitations in that it fails to address the complexities of supported metal catalysts that aren't present in model surfaces such as particle size and likely the effect of support (though this is beyond the scope of this work). The preparation of small, well-ordered Fe-Pt nanoparticles with a greatly enhanced activity are novel and can be used as evidence supporting the design of metals and an adaptation from a model system although care must be taken as these materials were demonstrated to restructure under reaction conditions. The significant particle size effects exhibited by the monometallic Ni catalysts and the lack of synergy shown between Fe-Ni demonstrate that the design hypothesis does not hold for every case.

4.7 Future Work

This work has yielded some interesting and unexpected results. Although the design philosophy on which these catalysts were based was not proven, a number of active catalysts were developed and these should be researched further. The synergy exhibited by Fe-Pt catalysts shows great potential for further examination. Colloidal preparation methods that offer more compositional control of the particles should be investigated as these will be able to better elucidate the active site. As it is the electronic modification of the alloy that gives rise to the synergy, the effect of the support should not be neglected. Lewis basic and Lewis acidic supports may further modify the electronic structure of the alloy particles offering scope for further enhancement in activity.

It has been demonstrated the alkali metals are effective promoters for some metals such as Ru and it would be of interest to the research community to investigate whether alloy catalysts can be promoted in the same way that monometallic catalysts can be.

4.8 References

1. Singh, A. K. & Xu, Q. Highly-dispersed surfactant-free bimetallic Ni-Pt nanoparticles as high-performance catalyst for hydrogen generation from hydrous hydrazine. *Int. J. Hydrogen Energy* **39**, (2014).

2. Hansgen, D. A., Thomanek, L. M., Chen, J. G. & Vlachos, D. G. Experimental and theoretical studies of ammonia decomposition activity on Fe-Pt, Co-Pt, and Cu-Pt bimetallic surfaces. *J. Chem. Phys.* **134**, (2011).

3. Simonsen, S. B., Chakraborty, D., Chorkendorff, I. & Dahl, S. Alloyed Ni-Fe nanoparticles as catalysts for NH3 decomposition. *Appl. Catal. A Gen.* **447**–**448**, 22–31 (2012).

4. Chellappa, A. ., Fischer, C. . & Thomson, W. . Ammonia decomposition kinetics over Ni-Pt/Al2O3 for PEM fuel cell applications. *Appl. Catal. A Gen.* **227**, 231–240 (2002).

5. Hansgen, D. A., Vlachos, D. G. & Chen, J. G. Using first principles to predict bimetallic catalysts for the ammonia decomposition reaction. *Nat. Chem.* **2**, 484–489 (2010).

6. Raróg-Pilecka, W., Szmigiel, D., Komornicki, A., Zieliński, J. & Kowalczyk, Z. Catalytic properties of small ruthenium particles deposited on carbon: Ammonia decomposition studies [4]. *Carbon N. Y.* **41**, 589–591 (2003).

7. Jacobsen, C. J. H. *et al.* Catalyst design by interpolation in the periodic table: Bimetallic ammonia synthesis catalysts [2]. *J. Am. Chem. Soc.* **123**, 8404–8405 (2001).

8. Duan, X., Qian, G., Zhou, X., Chen, D. & Yuan, W. MCM-41 supported CoMo bimetallic catalysts for enhanced hydrogen production by ammonia decomposition. *Chem. Eng. J.* **207**–**208**, 103–108 (2012).

9. 316 Stainless Steel Composition. Available at: https://www.upmet.com/products/stainless-steel/316316l%0A. (Accessed: 27th November 2018)

10. Hansgen, D. a, Vlachos, D. G. & Chen, J. G. Using first principles to predict bimetallic catalysts for the ammonia decomposition reaction. *Nature chemistry* **2**, 484–489 (2010).

11. Rozita, Y., Brydson, R. & Scott, A. J. An investigation of commercial gamma-Al $_2$ O $_3$ nanoparticles. *J. Phys. Conf. Ser.* **241**, 012096 (2010).

12. Son, I. H., Shamsuzzoha, M. & Lane, A. M. Promotion of Pt/γ-Al $_2$ O $_3$ by New Pretreatment for Low-Temperature Preferential Oxidation of CO in H $_2$ for PEM Fuel Cells. *J. Catal.* **210**, 460–465 (2002).

13. Antolini, E. & Cardellini, F. Formation of carbon supported PtRu alloys: an XRD analysis. *J. Alloys Compd.* **315**, 118–122 (2001).

14. Kaftan, A., Kusche, M., Laurin, M., Wasserscheid, P. & Libuda, J. KOH-promoted Pt/Al2O3catalysts for water gas shift and methanol steam reforming: An operando DRIFTS-MS study. *Appl. Catal. B Environ.* **201**, 169–181 (2017).

15. Mishra, K., Basavegowda, N. & Lee, Y. R. Biosynthesis of Fe, Pd, and Fe–Pd bimetallic nanoparticles and their application as recyclable catalysts for [3 + 2] cycloaddition reaction: a comparative approach. *Catal. Sci. Technol.* **5**, 2612–2621 (2015).

16. Pawelec, B. *et al.* AuPd alloy formation in Au-Pd/Al2O3catalysts and its role on aromatics hydrogenation. *Appl. Surf. Sci.* **242**, 380–391 (2005).

17. Carter, J. H. *et al.* Synergy and Anti-Synergy between Palladium and Gold in Nanoparticles Dispersed on a Reducible Support. *ACS Catal.* **6**, 6623–6633 (2016).

18. Ganley, J. C., Thomas, F. S., Seebauer, E. G. & Masel, R. I. A priori catalytic activity correlations: The difficult case of hydrogen production from ammonia. *Catal. Letters* **96**, 117–122 (2004).

19. Tada, S., Yokoyama, M., Kikuchi, R., Haneda, T. & Kameyama, H. N2O pulse titration of Ni/α-Al2O3 catalysts: A new technique applicable to nickel surface-area determination of nickel-based catalysts. *J. Phys. Chem. C* **117**, 14652–14658 (2013).

20. Jacobsen, C. J. H. *et al.* Structure sensitivity of supported ruthenium catalysts for ammonia synthesis. *J. Mol. Catal. A Chem.* **163**, 19–26 (2000).

21. Zhang, J., Xu, H. & Li, W. Kinetic study of NH3 decomposition over Ni nanoparticles: The role of la promoter, structure sensitivity and compensation effect. *Appl. Catal. A Gen.* **296**, 257–267 (2005).

22. Zheng, W., Zhang, J., Xu, H. & Li, W. NH3decomposition kinetics on supported Ru clusters: Morphology and particle size effect. *Catal. Letters* **119**, 311–318 (2007).

23. Yang, C. & Williams, D. B. A Revision of the Fe-Ni Phase Diagram at Low Temperatures (<400 oC). *J. Phase Equilibria* **17**, 522–523 (1996).

5 Effect of Promoters on Active Metal Species

5.1 Introduction and Aims of the Chapter

5.1.1 Literature Survey of Promoters for Ammonia Decomposition Catalysts

Alkali and alkaline earth metal promoters have been known and used for the ammonia synthesis reaction for decades.[1–7] They have also been studied in great depth for the ammonia decomposition reaction over the last 20 years.[8–11] As Ru is the most active metal for the reaction, most of the work has focussed on the promotion of Ru. All the alkali metals promote the activity of Ru such that promotion increases down the group with Cs being the most active.[12,13] Alkali and alkaline earth metals promote numerous reactions and their promoting properties have been shown to be due to structure stabilisation and/or electrostatics, depending on the reaction.[14,15]

Detailed studies by Hill *et al.* of the nature of the promoter and mechanism of promotion have been carried out.[16,17] In these studies, it was shown that more electrically conductive supports facilitate promotion through the enhancement of electron donation with multi-walled carbon nanotubes (MWCNTs) being the optimal support of those investigated.[17] Through TEM it was also shown that the promotion could be induced from remote Cs sites i.e. Cs did not have to be in contact with Ru nanoparticles. The electron donation was observed using TPR, with reduction temperatures of the two metals simultaneously affected. It was also concluded that the optimal Cs:Ru ratio was 3:1, with excess Cs causing the active site to be inaccessible to NH_3.[16]

This demonstrates the importance of electronic structure in the activity of ammonia decomposition catalysts. As discussed previously, N-binding energy is a good descriptor for the reaction and shows a volcano-style relationship dependent on rate determining step (RDS). The RDS for Ru is nitrogen

recombinative desorption and this is promoted by electron donation from Cs. Conversely, Torrente-Murciano *et al.* show that Co, with a low binding-energy and N-H bond scission RDS, is not promoted by Cs.[18] From this knowledge of the electronic behaviour of the reaction it may be possible to predict which metals will be promoted by Cs. If Co is not promoted by electron-donation, it is reasonable to predict that electron withdrawing promoters may facilitate the reaction by increasing the interaction between NH_3 and the metal and facilitating N-H bond scission. Fe is a cheap alternative to Ru and although inactive under typical ammonia decomposition reaction conditions it is known to be active for ammonia synthesis. Alkali promotion of Fe is also well-established in ammonia synthesis, therefore, in this chapter the promotion of Fe by Cs is investigated.

5.1.2 Aims

In this chapter, we set out to explore whether the use of N-binding energy can assist in the design of promoted transition metal catalysts. The hypothesis is that alkali metal promoters, which promote through electron donation, will only promote catalysts in which the rate of N_2 re-combinative desorption is the RDS. This includes Ru and all metals with an N-binding energy that are higher than the optimum (see figure 9 in chapter 1). Conversely, alkali metals are not expected to promote catalysts in which N-H bond scission is rate determining, such as Co.

To investigate this, a series of Cs-promoted Fe catalysts were prepared, tested and characterised. By this hypothesis, these catalysts should exhibit an enhanced activity due to the presence of a promoter. Characterisation of this catalyst through TPR should demonstrate the electron donating relationship of the promoter with the active site as shown in the Cs-Ru work of Hill *et al.*[17] The optimal loading of Cs was also identified and the cause of this optimum was investigated.

5.2 Effect of Cs as a Promoter for Fe

Five 5 wt.% Fe/Al_2O_3 catalysts promoted with differing molar equivalents of Cs were prepared by co-impregnation and tested for ammonia decomposition. CVI was not used in this work due to the lack of suitable Cs precursor. These catalysts will be referred to as Fe/Al_2O_3-XCs, where X is the mol. eq. Cs. Results for these 24 h tests are shown in Figure 1. It was observed that in all catalysts Cs promotes the activity of Fe/Al_2O_3 and all promoted catalysts exhibit an induction period of >12 hours, whereas the unpromoted-Fe catalyst shows no induction period. It is believed that this period is due to rearrangement of the Cs species on the surface as these become mobile at reaction temperature, however, further characterization is needed to investigate this. Because of the long induction period these catalysts were tested for 24 hours so that steady-state conversion was achieved.
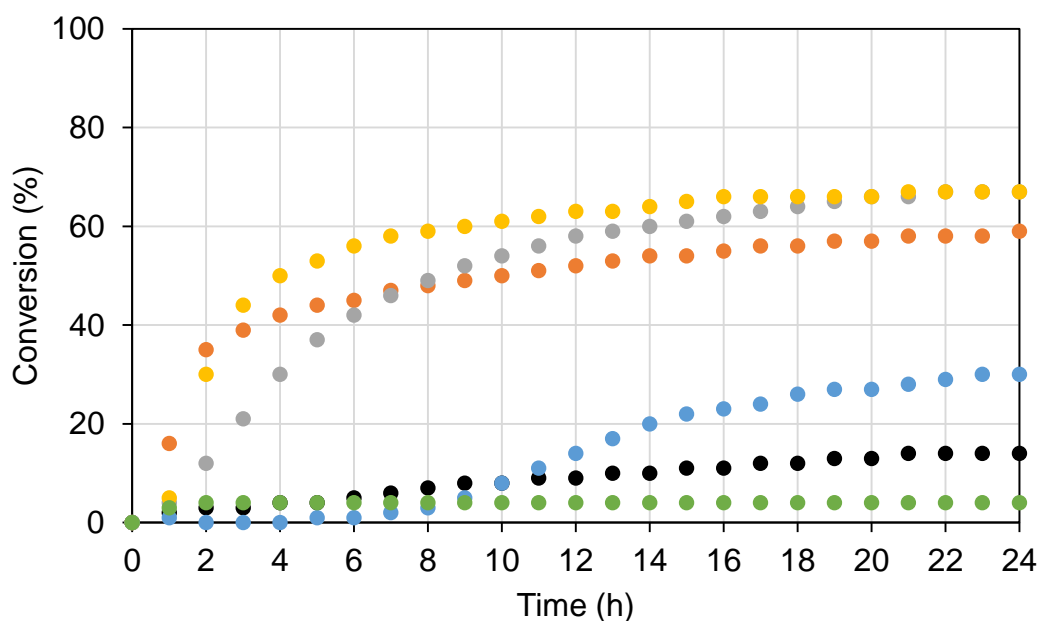

Figure 1: 24 hour testing results for 5%Fe-Cs/Al₂O₃ catalysts.
Conditions: 100 ml/min 0.5% NH₃/Ar, 100 mg catalyst pellets (300-425 µm), 500 °C
Legend: 0Cs (●), 0.1Cs (●), 0.25Cs (●), 0.5Cs (●), 1Cs (●), 2Cs (●)

The initial activity of the catalysts varies greatly and does not correlate with the final steady-state conversion of the catalysts, i.e. after two hours the 0.25Cs

catalyst appears to be the most active, however, after steady-state is achieved both 0.5Cs and 1Cs are more active. This could be attributed to the rate of formation of the active phase occurring during the induction period. With the exception of the 0.1Cs catalyst, the initial activity of the catalysts is higher with a lower loading of Cs. This suggests that the Cs loading could have an effect on the rate of active phase formation.

Figure 2 shows the conversion after 24 h as a function of Cs loading. Initially, the addition of Cs greatly enhances the activity of the Fe with activity increasing from 3% to 17% with 0.1 mol eq. Cs up to a maximum of 65% with 0.5 mol eq. Cs present. The conversion of ammonia stays the same for the catalyst with 1 mol eq. Cs and then decreases with a further increase in Cs content. This shows that there is an optimum Cs loading between 0.5 and 1 mol eq. The equal activity of the 0.5 and 1 mol eq. Cs catalysts could be explained by the enhancing effect of more Cs being balanced by the detrimental effect of excess Cs. It should be noted that this optimum Cs is far lower than the 3:1 ratio observed by Torrente *et al.* for Ru, however, their studies were conducted on CNT supports with a much higher surface area. This may increase the amount of Cs that can be impregnated before active sites are blocked. The cause of the activity drop after this optimum value, reaching a low of 30% for the catalyst promoted by 2 mol. eq. Cs, could be due to a surface saturation of Cs blocking active sites. In order to demonstrate
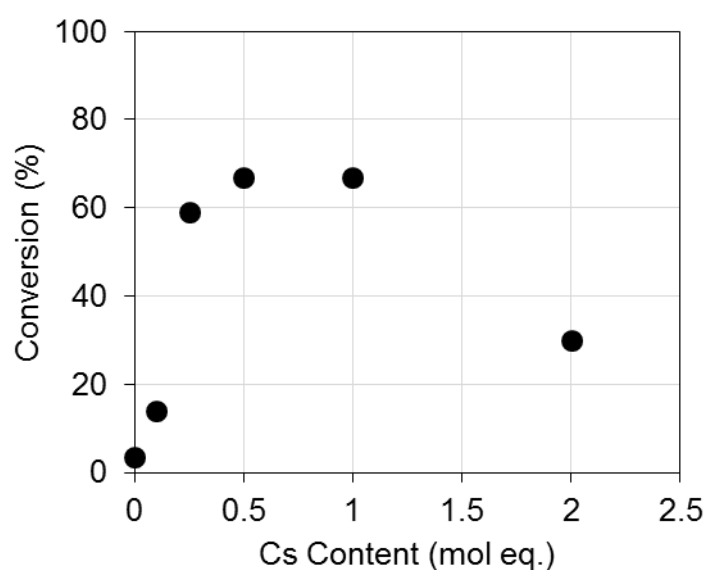
Figure 2: Relationship between Cs loading and catalytic activity

that Cs acts only as a promoter and not as an active site an 11 wt.% Cs/Al_2O_3 (1 mol eq.) catalyst was prepared in the same way and tested. This catalyst showed no activity.

This induction period indicates that the catalysts undergo a change under reaction conditions that is essential to their activity. It was also observed that catalysts left in an air environment would change colour from grey to orange, due to re-oxidation of Fe. Therefore, after the reaction the catalyst bed was purged with Ar and sealed. The catalyst was then removed and crushed into a fine powder in an MBraun Labstar glovebox under N_2 atmosphere with <5 ppm O_2 and stored under N_2 so that subsequent post-reaction characterisation could be performed on the active form of the catalyst.

5.3 Characterization of Fe-Cs Catalysts

5.3.1 H_2-TPR

H_2-TPR has been used in previous studies to observe the electron donating effect of Cs to Ru and is used here to investigate the same effect between Cs and Fe. Figure 3 shows the reduction pattern for unpromoted Fe/Al_2O_3, three of the Cs-promoted catalysts and Cs/Al_2O_3 with no Fe present.
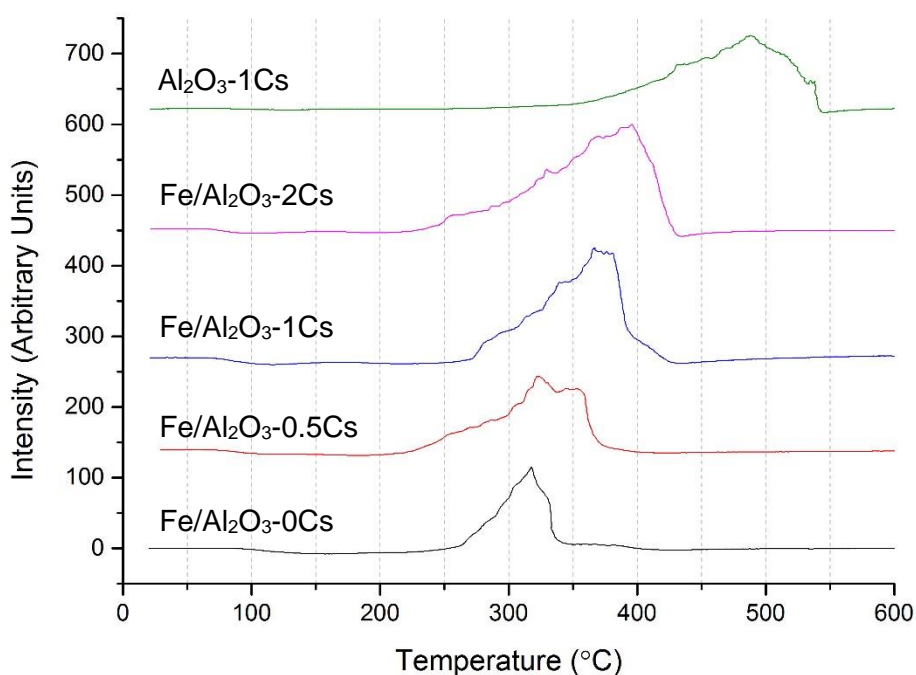
Figure 3: H_2-TPR of Fe/Al_2O_3 catalysts with varying Cs promoter loadings

Fe and Cs exhibit a broad reduction peak each at 315 and 490 °C, respectively. However, when both metals are present such as in the promoted catalysts only one reduction peak is observed. This can be attributed to the simultaneous reduction of Fe and Cs and is consistent with the findings of Hill *et al.* with their Cs-promoted Ru catalysts. Cs is reduced at considerably lower temperatures when in contact with Fe due to the dissociation of H_2 on the Fe[19] and subsequent spillover to nearby Cs. As the Cs content increases, the temperature of the simultaneous reduction peak increases and the integrated area of the reduction peak also increase (Table 1) as both metals are simultaneously reduced.

Table 1: Reduction temperature and peak area of $Fe-Cs/Al_2O_3$ catalysts

Catalyst	Reduction Temp. (°C)	Integrated Peak Area

Fe/Al₂O₃	315	6070
Fe-Cs/Al₂O₃ 0.5 mol eq.	340	9102
Fe-Cs/Al₂O₃ 1 mol eq.	360	12956
Fe-Cs/Al₂O₃ 2 mol eq.	395	15619
Cs/Al₂O₃	490	13298

5.3.2 XRD

X-ray diffraction patterns were recorded under a flow of N_2 in an *in-situ* cell to ensure the catalyst remained in their post-reaction form and are shown in Figure 4. All samples exhibit a low intensity, sharp peak at 29.5 °, which is a reflection due to the sample cell in the instrument. The catalysts with low concentrations of promoter (0.1-0.5 mol eq. Cs) show five well defined peaks at 32, 37, 39, 47, 62 and 68 ° corresponding to γ-Al_2O_3.[20] These reflections are due to the (220), (311), (222), (400), (333) and (440) planes respectively[21] and are in agreement with the database standard (JCPDS ref. no. 00-010-0425). No reflections due to Fe species are observed, suggesting that all Fe is present as either small nanoparticles or in an amorphous form. The expected Cs species, such as CsOH reported by Hill *et al.* in their study, are amorphous and could explain the absence of Cs in the diffraction patterns.
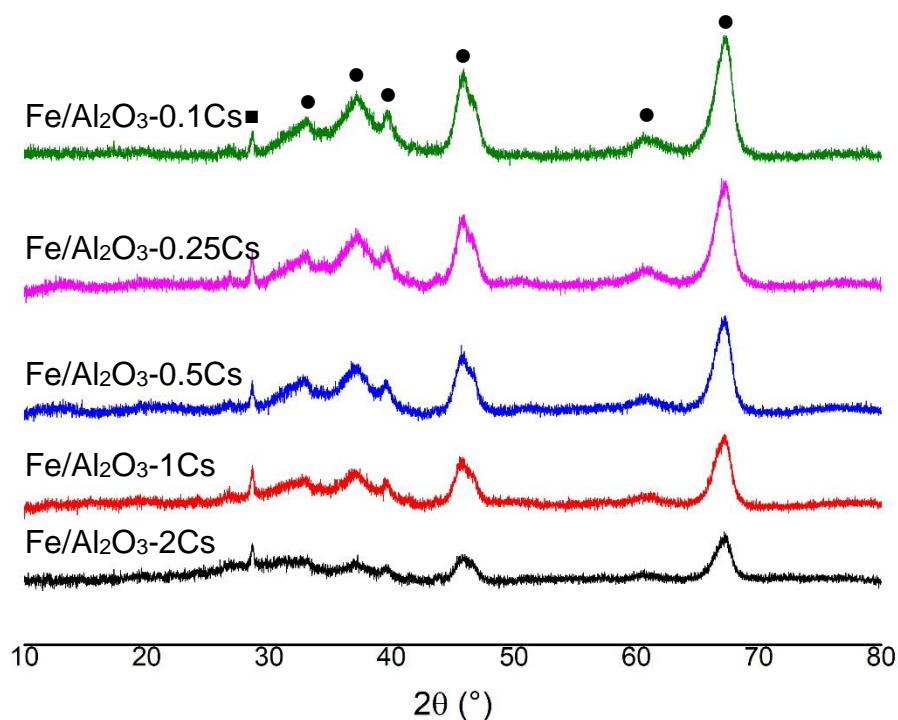
Figure 4: XRD diffraction patterns of 5%Fe/Al$_2$O$_3$-XCs catalysts showing reflections due to γ-Al$_2$O$_3$ (●) and the sample holder (■)

The diffraction patterns of catalysts with higher concentrations of Cs (1 and 2 mol eq. Cs) show the same peaks, however, they are broader and less intense and in the case of the 2 mol eq. Cs catalyst, the peaks at 32 and 37 ° are not clear. The reflection at 62 ° is also not present in the 1Cs and 2Cs samples. It is important to note that the intensity of the peak at 29.5 ° (which is due to the sample holder and not the sample) does not significantly decrease or broaden, indicating that this effect is a change in the catalyst and not due to sample measurement. This suggests that an amorphous layer is forming and obscuring the crystallinity of the catalyst below. This layer could be formed of an amorphous Cs species, such as CsOH forming. Cs has a high mass attenuation coefficient which means it absorbs X-ray radiation easily. If a layer of this was to form on top of the surface investigated, X-rays would be absorbed and the signal reaching the detector would get weaker. As this layer grows in thickness the signal gets progressively weaker, as is seen in Figure 5 and as the layer formed is amorphous no new reflections due to it are observed.

5.3.3 BET Surface Area

The saturation of the surface due to excess loading of Cs was also investigated by BET surface area as determined by N_2 physisorption (Table 2). It is seen that the Al_2O_3 support before impregnation is 124 m^2/g and that impregnation at low promoter concentrations (0.1 and 0.25 mol eq. Cs) does not significantly affect catalyst surface area. The surface area then appears to increase as the promoter loading is increased with the 0.5 mol eq. Cs catalyst exhibiting a surface area of 144 m^2/g and this could be due to the CsOH adding surface roughness and its own porous structure. It is then observed that a further increase in Cs loading has a detrimental effect on surface area. The catalyst with the highest Cs loading, 2 mol eq., has a surface area of only 70 m^2/g, almost half that of the 0.1Cs catalyst.

Table 2: BET surface area of Cs-promoted Fe/Al_2O_3 catalysts calculated using N_2-physisorption

Catalyst	Surface Area (m^2/g)	TOF (mol_{NH3}/m^2/h)
Al_2O_3	124	n/a
Fe/Al_2O_3-0.1Cs	122	0.0202
Fe/Al_2O_3-0.25Cs	129	0.0806
Fe/Al_2O_3-0.5Cs	144	0.0820
Fe/Al_2O_3-1Cs	112	0.1054
Fe/Al_2O_3-2Cs	70	0.0755

When activity (calculated at steady-state after 24 h) is normalised as a function of surface area the same trend is observed in that activity increases with Cs until 1Cs and then decreases after an excess of Cs is added. The difference in activity between 0.5Cs and 1Cs is made greater due to the difference in the surface area of the two catalysts, however, as this variation is due to experimental error this result may not be reliable. It is also seen that even when normalised for the lower surface area the 2Cs catalyst is still one of the least active catalysts.

This large decrease in surface area correlates with both the large loss in activity and the amorphous Cs layer forming over the catalyst. Surface area is well known to have an effect on catalyst activity for many reactions, including

ammonia decomposition. A common reason for the loss of surface area is the blocking of pores, which is likely to be a factor in the case of these catalysts. With such a high loading of Cs (~25 wt%) present, it is possible that a layer of CsOH is being formed over the support.

5.3.4 XPS

XPS was used to investigate the oxidation state of Fe and further investigate the cause of inactivity at higher concentrations of Cs. Figure 5 shows the region containing both Cs 3d and Fe 2p/3 transitions. The peak at 724.0 eV is attributed to CsOH and grows in intensity as the loading of Cs is increased, as is to be expected. This supports the conclusions drawn from the XRD and BET results that an amorphous layer of CsOH is formed at higher Cs loadings, blocking access to active sites. The broad peak around 710 eV is due to Fe and decreases in intensity as the concentration of Cs increases. This is further evidence that at higher concentrations of Cs a surface layer is formed, blocking active sites and reducing activity. This is further evidenced in Table 3, which quantifies the molar ratio of Cs:Fe and Cs:Al.
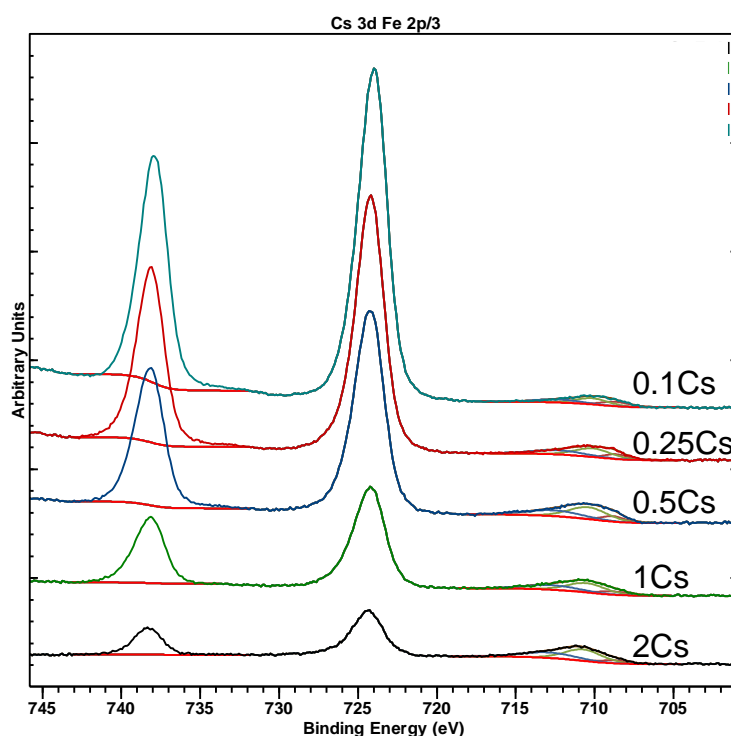

Figure 5: XPS spectrum of the region containing Cs 3d and Fe 2p/3 transition

In all these catalysts the Cs:Fe ratio is higher than expected and this is likely a combination of Cs being better dispersed than Fe and also forming a layer on top of the Fe nanoparticles. This suggests a layer of amorphous CsOH forming across the surface, which would lead to lower surface area as evidenced by N_2-physisorption measurements and lower crystallinity due to a lowering of crystallinity as observed in the XRD measurements.

Table 3: Cs:Fe and Cs:Al molar ratios as calculated from XPS

Cs Loading	Expected Cs:Fe	Observed Cs:Fe	Cs:Al
0.1 mol eq.	0.1	0.4	0.02
0.25 mol eq.	0.25	1.2	0.05
0.5 mol eq.	0.5	1.9	0.10
1 mol eq.	1	3.4	0.12
2 mol eq.	2	6.2	0.27

Figure 6 is an enlarged image of the Fe 2p/3 region of the spectrum in Figure 5. Fitting of this broad peak shows that Fe is present as two oxides; FeO as evidenced by the peak at 708.7 eV and Fe_2O_3 by the peak at 710.7 eV. It Is possible that the induction period observed in Figure 1 is due to the reduction of Fe_2O_3 to FeO with FeO being the active species, however, this would require further investigation. A ratio of these Fe species for each catalyst is shown in Table 4 and it is observed that as the Cs loading is increased, the ratio of $FeO:Fe_2O_3$ increases from 0.12 to 0.36. This is consistent with the increase in reduction temperature observed by TPR and further demonstrates how electronic modification by the Cs affects the Fe species.
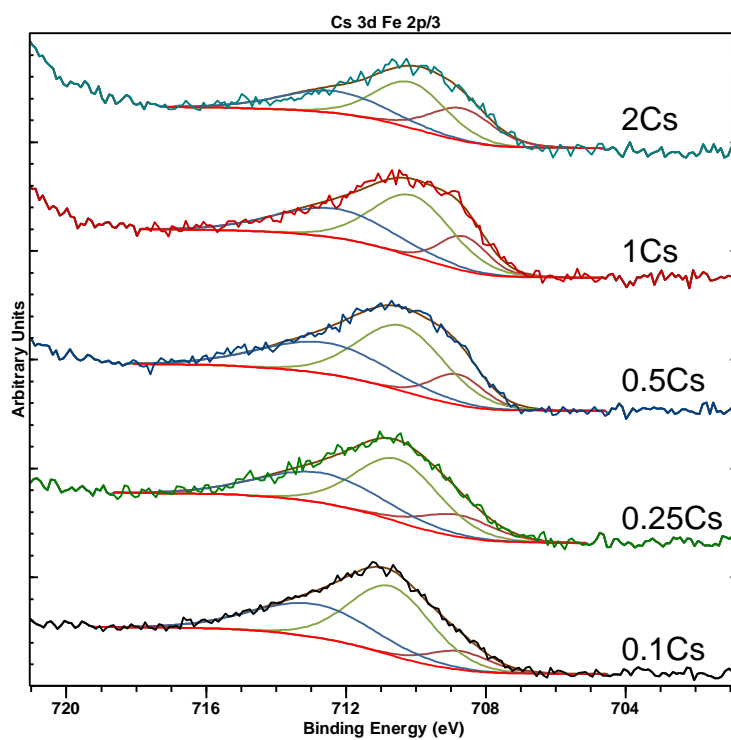
Figure 6: XPS spectrum of the Fe 2p/3 region including fittings

Table 4: Ratio of Fe species as determined by fitting of the Fe 2p/3 region

Catalyst	FeO:Fe$_2$O$_3$
Fe/Al$_2$O$_3$-0.1Cs	0.12
Fe/Al$_2$O$_3$-0.25Cs	0.18
Fe/Al$_2$O$_3$-0.5Cs	0.18
Fe/Al$_2$O$_3$-1Cs	0.20
Fe/Al$_2$O$_3$-2Cs	0.36

5.4 Conclusions

A series of promoted Fe/Al_2O_3 catalysts were prepared and tested to investigate the promoting ability of Cs and the effect of promoter concentration on activity. Cs was expected to promote Fe as it has been demonstrated as a promoter for Ru catalysts and, like Fe, Ru has a N-binding energy higher than the optimum. These catalysts were prepared by a co-impregnation method and confirmed that Cs is a suitable promoter for Fe catalysts.

All Cs-containing catalysts exhibited higher conversion than the Fe/Al_2O_3 catalyst with no Cs. A Cs/Al_2O_3 catalyst was also inactive, indicating that the enhancement in activity is due to the promotional effect of the Cs and not merely the addition of metal active sites. Catalyst evaluation indicated that as the concentration of Cs is increased, activity also increases up to a maximum of 73% conversion when 0.5 mol eq. Cs are present. Further increases of Cs at first does not increase activity (73% conversion at 1 mol eq. Cs) and then inhibits activity with activity decreasing to 30% with 2 mol eq. Cs present.

Characterisation using XRD and N_2-physisorption has shown that this decrease in activity coincides with a loss of catalyst crystallinity and surface area. It is proposed that at high concentrations of promoter (>1 mol eq. Cs) an amorphous layer of CsOH is formed on the majority of the support surface, blocking pores and restricting access to metal active sites. This is consistent with the results presented by Hill *et al*. in 2014.[16]

Alkali metal promotion is well reported for other reactions and Cs-promoted Fe has been used for many years as an ammonia synthesis catalyst, however, this is the first time such an investigation has shown its activity for the ammonia decomposition reaction. Many studies, including a related study into Cs-promoted ammonia decomposition, have described the mechanism of promotion by electron donation from the alkali metal to the active site.

5.5 Future Work

This proof of concept study has shown that Fe-based catalysts can be successfully promoted using Cs, however, further investigation into the diminishing promotion at high Cs concentrations is required, with analysis using techniques such as SEM to image amorphous CsOH species on the surface being desirable. Investigation into the effect of the support is also important, with carbon nanotubes being the most pressing due to their demonstration as being highly active support materials for Ru catalysts and their use in the study by Torrente *et al.*[17]

This work was motivated by the hypothesis that the N-binding energy can be used to predict not just novel alloy preparations, as investigated in Chapter 4 and by other groups, but can also be used to predict active promoters for this reaction. Whilst this work has successfully demonstrated the prediction of Fe being promoted by Cs, this is far from enough evidence to validate using the N-binding energy to choose promoters. Further work would focus on inactive metals with a lower than optimum binding energy, such as Pt and Pd. Pt and Pd catalysts should not be promoted by Cs or other alkali metals and demonstration of this will help in the proving of this. However, the discovery of a promoter for these metals would further ensure that this design method is validated.

5.6 References

1. Ertl, G., Lee, S. B. & Weiss, M. Adsorption of nitrogen on potassium promoted Fe(111) and (100) surfaces. *Surf. Sci.* **114**, 527–545 (1982).

2. Hagen, S. *et al.* Ammonia synthesis with barium-promoted iron-cobalt alloys supported on carbon. *J. Catal.* **214**, 327–335 (2003).

3. Rossetti, I., Pernicone, N. & Forni, L. Promoters effect in Ru/C ammonia synthesis catalyst. *Appl. Catal. A Gen.* **208**, 271–278 (2001).

4. Aika, K. *et al.* Support and promoter effect of ruthenium catalyst. I. Characterization of alkali-promoted ruthenium/alumina catalysts for ammonia synthesis. *J. Catal.* **92**, 296–304 (1985).

5. Liang, C., Wei, Z., Xin, Q. & Li, C. Ammonia synthesis over Ru/C catalysts with different carbon supports promoted by barium and potassium compounds. *Appl. Catal. A Gen.* **208**, 193–201 (2001).

6. Forni, L., Molinari, D., Rossetti, I. & Pernicone, N. Carbon-supported promoted Ru catalyst for ammonia synthesis. *Appl. Catal. A Gen.* **185**, 269–275 (1999).

7. Dahl, S., Logadottir, A., Jacobsen, C. J. H. & Nørskov, J. K. Electronic factors in catalysis: the volcano curve and the effect of promotion in catalytic ammonia synthesis. *Appl. Catal. A Gen.* **222**, 19–29 (2001).

8. Yin, S. F., Xu, B. Q., Zhou, X. P. & Au, C. T. A mini-review on ammonia decomposition catalysts for on-site generation of hydrogen for fuel cell applications. *Appl. Catal. A Gen.* **277**, 1–9 (2004).

9. Raróg-Pilecka, W. Ammonia decomposition over the carbon-based ruthenium catalyst promoted with barium or cesium. *J. Catal.* **218**, 465–469 (2003).

10. Liu, H., Wang, H., Shen, J., Sun, Y. & Liu, Z. Promotion effect of cerium and lanthanum oxides on Ni/SBA-15 catalyst for ammonia decomposition. *Catal. Today* **131**, 444–449 (2008).

11. Jedynak, A., Kowalczyk, Z., Szmigiel, D., Raróg, W. & Zieliński, J.

Ammonia decomposition over the carbon-based iron catalyst promoted with potassium. *Appl. Catal. A Gen.* **237**, 223–226 (2002).

12. Mukherjee, S., Devaguptapu, S. V., Sviripa, A., Lund, C. R. F. & Wu, G. Low-temperature ammonia decomposition catalysts for hydrogen generation. *Appl. Catal. B Environ.* **226**, 162–181 (2018).

13. Wang, S. J. *et al.* Investigation on modification of Ru/CNTs catalyst for the generation of COx-free hydrogen from ammonia. *Appl. Catal. B Environ.* **52**, 287–299 (2004).

14. Zhang, C. *et al.* Alkali-metal-promoted Pt/TiO2opens a more efficient pathway to formaldehyde oxidation at ambient temperatures. *Angew. Chemie - Int. Ed.* **51**, 9628–9632 (2012).

15. Xiong, H., Motchelaho, M. A., Moyo, M., Jewell, L. L. & Coville, N. J. Effect of Group i alkali metal promoters on Fe/CNT catalysts in Fischer-Tropsch synthesis. *Fuel* **150**, 687–696 (2015).

16. Hill, A. K. & Torrente-Murciano, L. In-situ H2 production via low temperature decomposition of ammonia: Insights into the role of cesium as a promoter. *Int. J. Hydrogen Energy* **39**, 7646–7654 (2014).

17. Hill, A. K. & Torrente-Murciano, L. Low temperature H2 production from ammonia using ruthenium-based catalysts: Synergetic effect of promoter and support. *Appl. Catal. B Environ.* **172**–**173**, 129–135 (2015).

18. Torrente-Murciano, L., Hill, A. K. & Bell, T. E. Ammonia decomposition over cobalt/carbon catalysts—Effect of carbon support and electron donating promoter on activity. *Catal. Today* **286**, 131–140 (2017).

19. O'Byrne, J. P. *et al.* High CO2 and CO conversion to hydrocarbons using bridged Fe nanoparticles on carbon nanotubes. *Catal. Sci. Technol.* **3**, 1202 (2013).

20. Rozita, Y., Brydson, R. & Scott, A. J. An investigation of commercial gamma-Al 2 O 3 nanoparticles. *J. Phys. Conf. Ser.* **241**, 012096 (2010).

21. Lippens, B. C. & de Boer, J. H. Study of Phase Transformations During

Calcination of Aluminum Hydroxides by Selected Area Electron Diffraction. *Acta Cryst* **17**, 1312–1321 (1964).

6 Conclusions and Future Work

With climate change heading towards an irreversible global temperature rise due in part to the rising levels of atmospheric CO_2, carbon-free alternatives to fossil fuels are being sought. Hydrogen presents a clean and renewable energy source with the only product of both its combustion and its use in fuel cell being water. However, hydrogen presents challenges in both its storage and transport and because of this, attention has turned to ammonia as a potential hydrogen storage material.

In this work, the effect of heat-treatment, support and preparation on the activity of Ru catalysts was investigated. Reduction of a commercial 5%Ru/C catalyst was shown to lower the activation energy by 17 kJ mol^{-1} when compared to a calcination heat-treatment. TPR and XPS indicated that more metallic Ru was present in the reduced catalyst suggesting that this is the most active Ru species. When prepared by impregnation, the activity of Ru on the four cheap and industrially scalable supports tested was as follows: Al_2O_3 > SiO_2 ~ C > TiO_2.

Following these initial results, chemical vapour impregnation (CVI) was investigated as a novel method for the preparation of Ru/Al_2O_3. The CVI catalyst exhibit a T_{50} of c. 30 °C lower than the impregnation prepared catalyst. BET surface area of both catalysts was the same. TEM imaging showed that whilst the mean particle size of the two catalysts was comparable, the particle size distribution showed more Ru particles within the optimum size range, 3-5 nm, than the impregnation prepared catalyst which exhibit more particles below 3 nm. This suggests that the CVI catalyst is more active due to a higher number of the active B_5 sites which are most abundant in particles between 3-5 nm. XPS characterization showed that contrary to previous reports, high temperature reduction does not completely remove residual Cl$^-$ from the RuCl$_3$ precursor, leading to a higher surface concentration of Cl$^-$ in the impregnation

prepared catalyst. These are known to be inhibitors and suggest that the increase in activity for catalysts prepared by CVI is two-fold, with the lack of inhibitors and more optimal particle size both contributing.

The effect of pH on the preparation of $CoMoO_4$ was investigated due to their use as precursors to the highly active Co_3Mo_3N catalyst. $CoMoO_4$ was prepared by co-precipitation with the pH left uncontrolled or controlled at 5.5 and 8. The pH of the uncontrolled co-precipitation was 5.5. Characterization by XRD and SEM showed that the pH of precipitation played a significant role in $CoMoO_4$ structure and morphology. XRD showed that the samples with controlled pH formed crystalline phases identified as $CoMoO_4$, however they were not pure. This is in contrast to the catalyst precipitated without pH control which was amorphous. SEM images showed that in all three cases different morphologies were formed.

Catalyst testing did not show the synergistic effect previously reported, however, it did show that pH of the co-precipitation had an effect on catalyst activity. The catalysts prepared with no pH control and at pH 8 exhibited comparable activities whereas the catalyst prepared at pH 5.5 was less active. XRD characterization of the post-reaction sample showed that the catalysts were less active than previously reported as they had not formed a nitride, instead forming a partially reduced oxide, $Co_2Mo_2O_8$. Further work should focus on the nitridation step of these catalysts as it was suggested in this study that ammonia concentration influences the phase formed.

Periodic table interpolation was previously used as a design method to predict the Co_3MoN catalyst as being more active than Ru. This is due to the alloy having a more optimal N-binding energy, a key descriptor for the reaction. In this work, three Al_2O_3-supported alloy nanoparticle catalysts predicted to exhibit synergy were prepared by CVI to examine the robustness of this design method. These alloys were Fe-Pt, Fe-Pd and Fe-Ni.

The Fe-Pt catalysts showed remarkable synergy with a trend of activity increasing with Fe content. TEM and XRD analysis showed that co-CVI was a more optimal preparation method than seq-CVI as when the metals were added sequentially large, unalloyed Pt particles were present, whereas when

they were added simultaneously the particles were smaller and alloyed throughout the sample. These catalysts were shown to be stable under reaction conditions for up to 20 h, however, post-reaction STEM showed that under reaction conditions the particles rearrange and become a random alloy. Examination by CO-DRIFTS showed that the most active catalyst demonstrated no CO-binding which suggests that the alloy formed is electronically different to the parent metals

The Fe-Pd catalysts showed the same synergistic trend of activity increasing with Fe loading, however the overall activity was approximately half that of the Fe-Pt catalysts. At high Pd contents, large metallic Pd particles were observed by XRD and these decreased as the Fe-content increased. CO-DRIFTS showed CO-Pd binding modes at the high Pd contents which also decreased as Fe-content increased. The most active catalyst ($Fe_{80}Pd_{20}$) showed no CO-binding peaks, suggesting that the alloyed catalyst is electronically modified in such a way that CO-binding is not facilitated. Both the XRD and CO-DRIFTS data suggest that the synergistic effect observed may not be due to a tuning of the N-binding energy but merely due to smaller Pd particles being more active, however, the extent of alloying also increases with activity suggesting that the alloy particles are a more active species than the parent metals.

The Fe-Ni catalysts showed no conclusive evidence of a synergistic effect. Examination of the most Ni-rich alloy suggested that the particles formed were alloyed. For each alloy ratio a monometallic Ni analogue, with the same Ni content as the alloy, was prepared. Analysis of these monometallic Ni particles using N_2O titration showed that as the weight loading decreased, larger more active particles were formed. The activity of these particles was attributed to a higher concentration of B_5-sites, the same active sites as present in the Ru catalysts.

The investigation into alloying failed to conclusively support the use of periodic table interpolation as a design method, however, active alloy catalysts Fe-Pt and, to a lesser extent Fe-Pd, were prepared that were predicted to be active. The heterogeneous nature of supported nanoparticle catalysts is not taken into account and factors such as particle size were shown to have a large effect on

catalyst activity. For future work to investigate this further, model particles and surfaces would have to be studied.

Finally the promotion of Fe, an inactive metal, with Cs was investigated. A series of catalysts with various molar equivalents of Cs (0.1-2 mol eq.) were prepared by co-impregnation. It was shown that the presence of Cs enhanced the activity of the Fe catalysts in all cases, with an optimum Cs loading being between 0.5-1 mol eq. Further addition of Cs was shown to decrease activity. XRD, XPS and BET surface area analysis suggest that this is due to an amorphous layer of CsOH forming over the catalyst surface, both decreasing catalyst surface area and blocking active sites. TPR and XPS studies suggest that the promotion is due to an electronic modification.

Further work on this topic should focus on the use of the N-binding energy descriptor as a means to predict suitable promotors. It has been shown that electron donating promotors such as Cs promote both Fe and Ru which both have an above optimal binding energy. Therefore, the investigation of electron-withdrawing groups as promotors for metals with a lower than optimal binding energy may yield important results.